N73-31209

NASA CR-120963

Final Report

DESIGN AND DEVELOPMENT LIQUID HYDROGEN MIXER UNIT

By

Robert W. Morgan
Kenneth Wuertz
Robert R. Rudich

CASE FILE COPY

Distribution of this report is provided in the interest of information exchange. Responsibility for the contents resides in the author or organization that prepared it.

Prepared under Contract No. NAS 3-11208

by

AiResearch Manufacturing Company
Torrance, California

for

NATIONAL AERONAUTICS AND SPACE ADMINISTRATION

National Aeronautics and Space Administration

NASA CR-120963

Final Report

DESIGN AND DEVELOPMENT LIQUID HYDROGEN MIXER UNIT

By

Robert W. Morgan
Kenneth Wuertz
Robert R. Rudich

Distribution of this report is provided in the interest of information exchange. Responsibility for the contents resides in the author or organization that prepared it.

Prepared under Contract No. NAS 3-11208

by

AiResearch Manufacturing Company
Torrance, California

for

NATIONAL AERONAUTICS AND SPACE ADMINISTRATION

National Aeronautics and Space Administration

CONTENTS

Section		Page
1	Summary	1-1
2	Introduction	2-1
3	Symbols	3-1
4	Design and development of liquid hydrogen mixer unit	4-1
	General	4-1
	Design analyses	4-1
	Philosophy	4-1
	Mechanical design	4-2
	Electrical motor	4-13
	Electronic motor control module principles of operation	4-18
	Position sensor development	4-25
	Circuit diagram	4-44
	Development testing	4-44
	Fabrication	4-50
	Evaluation	4-54
5	Conclusions	5-1
6	Recommendations	6-1
Appendix A	Evaluation testing	A-1
Appendix B	Evaluation test procedure	B-1
Appendix C	Failure analysis	C-1
Appendix D	Bearing report	D-1

FINAL REPORT ON DESIGN AND DEVELOPMENT OF A LIQUID HYDROGEN MIXER UNIT

By R. W. Morgan, K. Wuertz, and R. R. Rudich

SECTION 1
SUMMARY

A dc brushless motor driven "mixer unit" (a vaneaxial fan) was designed and evaluated for use in cryogenic fluids (liquids and gases). It was found to operate well in all fluids in which it was tested. The test fluids were liquid and gaseous helium, hydrogen in the liquid phase gas phase and mixtures of the two phases, and liquid nitrogen. It operated for over 100 hr at cryogenic temperatures without damage to the bearings and at the conclusion of testing the condition of the bearings was such that an operational life of 5000 hr appeared possible.

The unit demonstrated that (with the brushless dc motor principle) useful pumping of cryogenic fluids could be accomplished with very small power inputs to the mixer motor. During test, the motor input power varied from approximately 0.5 W to 2.5 W, depending on fluid density. The high power input produced a mixer efficiency of over 49 percent. In an earlier program (see NASA Report CR-72365), a mixer using an ac induction motor demonstrated an efficiency of 17.7 percent under the same conditions, illustrating the advantage of the dc brushless motor driven unit.

The mixer also demonstrated its ability to automatically vary speed as a function of the density of the fluid being pumped. This causes the unit to deliver higher volumetric flow rates as fluid density decreases.

SECTION 2
INTRODUCTION

Contract No. NAS 3-11208 was awarded by the NASA Lewis Research Center to develop a prototype dc brushless motor driven cryogenic mixer unit for installation in liquid hydrogen (LH_2) tanks of long duration space vehicles. The contract specified a unit to operate from 28 $\pm$2 Vdc power with a shaft power not to exceed 3 W in liquid hydrogen and with a maximum starting time of 500 msec in LH_2. It was also specified that the unit was to have 5000 hours of operation as a design goal and was to operate in LH_2, gaseous helium (GHe), and gaseous hydrogen (GH_2) or mixtures of these fluids.

The fluid pumping characteristics specified were:

Liquid hydrogen

Flow rate: 1320 lb (600 kg) per hr at a pressure rise of 2 in. H_2O (498 N/m^2)

Gaseous helium: 57.4 lb (26.1 kg) per hr at a pressure rise of 0.2 in. H_2O (49.8 N/m^2)

The program to accomplish these objectives was divided into the following tasks:

Design and development

Fabrication

Testing

Data evaluation

Three engineering disciplines also made major contributions to identifiable portions of the unit:

Mechanical--The basic fan, including fluid dynamics

Electrical--The motor

Electronics--The motor control module

This report attempts to separate these tasks, disciplines, and major components to the extent possible to achieve order. Figure 2-1 is a photograph of the mixer unit produced.

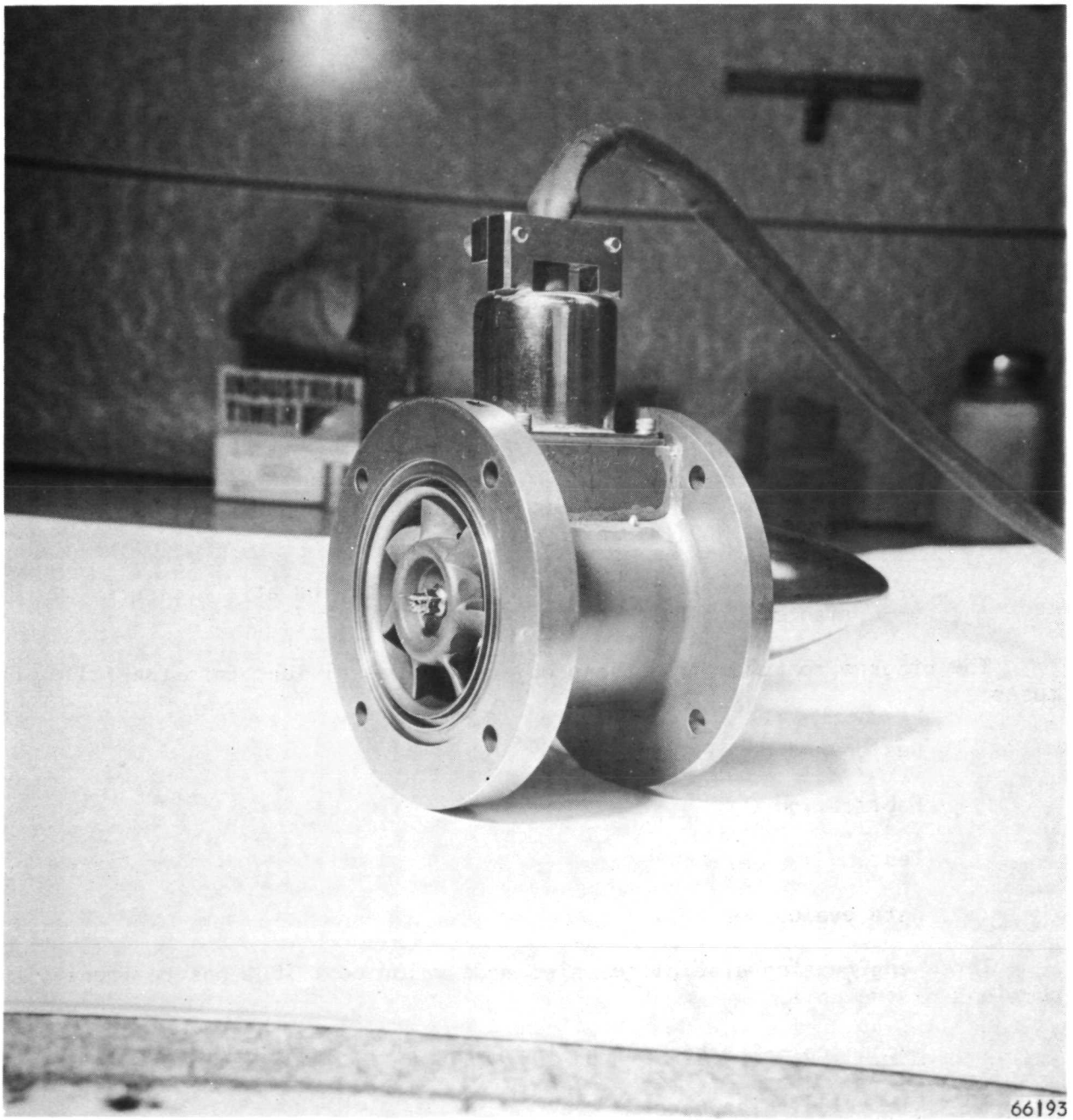


Figure 2-1. Liquid Hydrogen Mixer Unit, AiResearch PN 605632-1-1 (Electronics Not Shown)

SECTION 3
SYMBOLS

A	Area ~ square feet
A	Designates First Phase Motor Winding
A	Ampere
A^o	Angstrom Unit
A.W.G.	American Wire Gage
B	Designates Second Motor Phase Winding
BDCM	Brushless Direct Current Motor
C	Designates Third Phase Motor Winding
C	Impeller Tip Chord Length ~ feet
C	Capacitance ~ farads
C	Temperature ~ centigrade degrees
CFM	Cubic Feet per Minute
C_m	Axial Velocity ~ Feet per Second
CR	Designates Diode
C_S	Switching Capacitance in Farads
D	Designates Fourth Phase Motor Winding
D	Diameter ~ inches
DC	Direct Current
D_h	Impeller Hub Diameter ~ inches
D_t	Impeller Tip Diameter ~ inches
D_t'	Impeller Tip Diameter Before Correction ~ inches
E	Applied EMF ~ volts
E	RMS EMF ~ volts
E	Electrical Energy ~ joules

Egm	Maximum Generated Motor EMF ~ volts
E_{in}	Input EMF ~ volts
E_m	Motor EMF input ~ volts
E_x	Excitation EMF ~ volts
e	Instantaneous EMF ~ volts
e_g	Instantaneous EMF generated by Motor ~ volts
e_{sa}	Instantaneous Motor Switching EMF ~ volts
ft	Feet
F	Temperature in Degrees Fahrenheit
Fc	Commutating Frequency ~ Hz
G He	Gaseous Helium
Hc	Coercive Force
Hz	Frequency ~ cycles per second
I	Electric Current ~ amperes
I_s	Motor Stall Current ~ amperes
I_m	Instantaneous Motor Currency ~ amperes
K	Absolute Temperature, Degrees Kelvin
kg	Kilograms
KHz	One Thousand Hertz
KΩ	One Thousand Ohms
lb	Pound
L	Inductance ~ henrys
L_W	Winding Inductance ~ henrys
LH_2	Liquid Hydrogen
LHe	Liquid Helium

LN_2	Liquid Nitrogen
M	Motor Winding Coupling Constant ~ dimensionless
min	Minute
m	Meter
mh	Capacitance ~ millihenry
N	Newton
N	Rotational Speed ~ RPM
N_{corr}	Corrected Rotational Speed ~ RPM
N_R	Reynolds Number ~ Dimensionless
P	Pressure ~ Pounds per Square Inch
P	Number of Poles of Motor
pf	Capacitance ~ Farads X 10^{-12}
PSIA	Pounds Per Square Inch Absolute
PU	Designates Per Unit Quantity - Dimensionless
P_v	Velocity Pressure ~ Inches of Water
PWR	Power ~ Watts
PWR_E	Power Into Electronics ~ Watts
PWR_L	Power Lost Due to Winding Inductance in Watts
PWR_M	Motor Power Input ~ Watts
PWR_{shaft}	Motor Shaft Power ~ Watts
PWR_R	Power Consumed in Resistance ~ Watts
Q	Volumetric Flow Rate ~ CFM
Q	Heat Flow ~ BTU/Hr
Q'	Calculated Flow Rate Before Impeller Area Corrected ~ CFM

Q_{GHe}	Volumetric Gaseous Helium Flow Rate ~ CFM
Q_{LH_2}	Volumetric Liquid Hydrogen Flow Rate ~ CFM
R	Electrical Resistance ~ Ohms
R_M	Electrical Resistance of Motor Winding ~ Ohms
R_S	Electrical Resistance of External Shaping Resistor ~ Ohms
R_T	Total Resistance ~ Ohms
RPM	Rotational Speed ~ Revolutions per Minute
sec	Second
T	Torque ~ Inch ~ Ounces
t	Time ~ Seconds
t	Temperature ~ Degrees Fahrenheit
u	Tangential Velocity ~ Feet per Second
v	EMF ~ Volts
V	Velocity ~ Feet per Second
V_{CALC}	Calculated Velocity ~ Feet Per Second
V_M	Motor Voltage Applied, including Shaping Resistor ~ Volts
W	Number of Windings
W	Power ~ Watts
$\bar{W}$	Gravitemetric Flow Rate ~ Pounds per Hour
z	Number of Electrical Conductors in Series
ΔD_t	Change in Impeller Tip Diameter ~ Inches

ΔP	Change in Total Pressure ~ Inches of Water
ΔP_V	Change in Velocity Pressure ~ Inches of Water
ΔT	Temperature Difference ~ ^0F
θ	Phase Angle ~ Degrees
θc	Commutator Phase Angle ~ Degrees
η_a	Aerodynamic Efficiency at Low N_R relative to Nr $\geq 3X10^5$, Percent
η_{el}	Electronics Efficiency ~ Percent
η_f	Fan Efficiency ~ Percent
η_{IT}	Power Input Into Motor X 100 ~ Percent Fluid Dynamic Power of Motor
η_{MTR}	Motor Efficiency ~ Percent
η_{OA}	Overall Efficiency ~ Percent
μ	Viscosity ~ Pound Per Second Foot
ρ	Weight Density ~ Pounds per Cubic Foot
ρ_{CAL}	Weight Density of Calibrating Fluid ~ Pounds per Cubic Foot
ρ_{GHe}	Weight Density of Gaseous Helium ~ Pounds per Cubic Foot
ρ_{LH_2}	Weight Density of Liquid Hydrogen ~ Pounds per Cubic Foot
σ	Ratio of Density of a Fluid to Air at Standard Conditions of .0765 Pounds per Cubic Foot ~ Dimensionless
σ_{GHe}	Ratio of Density of Gaseous Helium to .0765 ~ Dimensionless
σ_{LH_2}	Ratio of Density of Liquid Hydrogen to .0765 ~ Dimensionless

ϕ	Magnetic Flux ~ Lines
ϕ_P	Magnetic Flux per Pole ~ Lines
Ω	Electrical Resistance ~ Ohms
ω	Rotational Speed ~ Radians per Second

SECTION 4
DESIGN AND DEVELOPMENT OF LIQUID HYDROGEN MIXER UNIT

General

This program was undertaken by the NASA Lewis Research Center because cryogens offer high-vehicle performance capability when used as propellants for long-duration space missions. In utilizing cryogens, a problem requiring solution involves the efficient control of tank pressure during zero or low-gravity coast periods. Heat leak into the propellant tanks results in increased internal pressure, the pressure can be efficiently controlled if only vapor, (i.e., no liquid) is vented to space. In a zero or low gravity environment, however, the location of the liquid and vapor phases is uncertain. An approach to tank pressure control, which does not require active or passive fluid phase control, and allows only vapor to be vented to space, has been defined in NASA Report No. CR-72365. This concept, a liquid propellant thermal conditioning system, maintains tank pressure control by extracting fluid from the tank, expanding the fluid and then passing the expanded refrigerated fluid through a heat exchanger to chill the ullage gas. This causes a reduction in tank pressure; the expanded fluid in passing through the heat exchanger, is completely vaporized, may be slightly superheated and is vented overboard. Fluids on the ullage side of the heat exchanger must be pumped through the heat exchanger using a mixer unit. The mixer unit is completely contained within the propellant tank, so that all power consumed by the mixer appears in the propellant tank as heat. Consequently, it is important that the power input to the mixer unit be as low as practical to minimize the boil-off, and waste by overboard venting of the propellants

Earlier work on the Apollo program had shown that small power sizes of brushless dc motors could be made more efficient than ac induction motors. Thus, the dc brushless-type motor was selected to power the mixer. In the dc brushless motor, an electronic control module is necessary to commutate the motor. This module was located outside the tank to remove the heat generated by the inefficiencies of the control module from the propellant tank. This also greatly simplified circuit component selection and circuit board design and fabrication.

Design Analyses

Philosophy.--There were essentially two (2) design points for the mixer whose required pressure rises were not related by the first power of fluid density. This dictated the use of a motor having a speed curve inversely proportional to torque, so that the motor would run slowly in liquid hydrogen and much faster in gaseous helium. Conventional ac induction motors tend to be constant speed machines and even "high slip" motors could not be expected to meet the required speed/torque relationship with the desired accuracy without the incorporation of relatively complex control circuitry.

In a dc motor the establishment of a straight line torque-speed characteristic, defined by the two required operating points, is a simple matter. However, the conventional brush-type motor is not suitable for operation in a cryogen due to brush wear and brush mechanical problems. Moreover, brush sparking is obviously incompatible with an explosive atmosphere. Accordingly, a permanent magnet rotor, brushless dc motor was selected for this application.

The dc brushless motor is similar to a dc brush-type motor except that the rotor is a permanent magnet field and the stator is commutated. The commutation is accomplished by sensing the position of the rotating field poles and electronically switching the stator windings accordingly. The switching is accomplished by power transistors which are turned on by the rotor position sensors. Since the position sensors are subjected to the same cryogenic temperatures as the motor, considerable attention was given to their design.

The initial design technique was to determine the mechanical powers and rotational speeds required by the fluid dynamic component at each design condition. The motor was then sized for these conditions with its input power, winding resistance, inductance, number of poles, number of phases, and waveform type selected. The value of a "shaping resistor" to regulate the speed of the motor as a function of load at the two design points was also considered. The electronic motor control module was then designed to match the required motor characteristics.

Mechanical design.--The first step in designing the mixer was to find the shaft power requirements and speed ratio so that the motor could be sized. To do this, the volumetric flow at each design condition had to be known. The unit must operate through the range of pressures from 17 psia (1.17×10^5 N/m^2) to 28 psia (1.93×10^5 N/m^2). For saturated liquid, the density change for LH_2 is only 3.7 percent in this pressure range, so for convenience the LH_2 density at 17 psia (1.17×10^5 N/m^2) was selected. In addition, the mixer would produce the lowest head rise at 17 psia (1.17×10^5 N/m^2) in helium. Thus densities for both media at 17 psia (1.17×10^5 N/m^2) and saturated LH_2 temperature were used, producing the following values:

$$\rho_{LH_2} = 4.38 \text{ lb/ft}^3 \ (70.1 \text{ kg/m}^3)$$

$$\rho_{GHe} = 0.179 \text{ lb/ft}^3 \ (2.86 \text{ kg/m}^3)$$

The LH_2 volumetric flow rate is then:

$$\frac{\overline{W}}{60\ \rho_{LH_2}} = Q$$

$$Q_{LH_2} = \frac{1320}{60(4.38)} = 5.02 \text{ cfm } (2.37 \times 10^{-3} M^3/\text{sec})$$

$$Q_{GH_e} = \frac{57.4}{60(0.179)} = 5.34 \text{ cfm } (2.51 \times 10^{-3} M^3/\text{sec})$$

Overall fluid efficiency is made up of estimates of the efficiencies of the blading, deswirl section, and diffuser section. Estimated efficiency for the blading: 80 percent. Estimated efficiency for the deswirl and diffuser: 75 percent then,

$$\eta_{OA} = 0.8 \ (0.75) = 0.6$$

$$PWR_{Shaft} = \frac{11.7 \times 10^{-2} \ (cfm) \ \Delta P}{\eta_{OA}} + \text{Bearing Loss} + \text{Windage}$$

Windage losses were ignored since the speed was expected to be relatively low and it was expected that within a short period of operation any liquid inside the rotor cavity would be converted to gas. Bearing friction was estimated as 9×10^{-3} oz-in. (6.4×10^{-6} N-m) or 0.02 W at 2700 rpm, so for the LH_2 design condition:

$$PWR_{Shaft} = \frac{11.7 \times 10^{-2} \ (5.02) \ (2)}{0.6} + 0.02 = 1.98 \text{ W}$$

And if efficiencies remain the same, for the GHe design condition the shaft power requirement would be 0.21 W.

Reynolds number is fundamental to the establishment of dynamic similarity. It establishes the relationship between the viscous and inertial forces and insures that dimensionless coefficients are comparable when a machine is operated in two different fluids. By inspection of the formula for Reynolds number, it may seem that all the terms which effect incompressible flow between two geometrically similar devices are included.

$$N_R = \frac{VC\rho}{\mu} \text{ (dimensionless)}$$

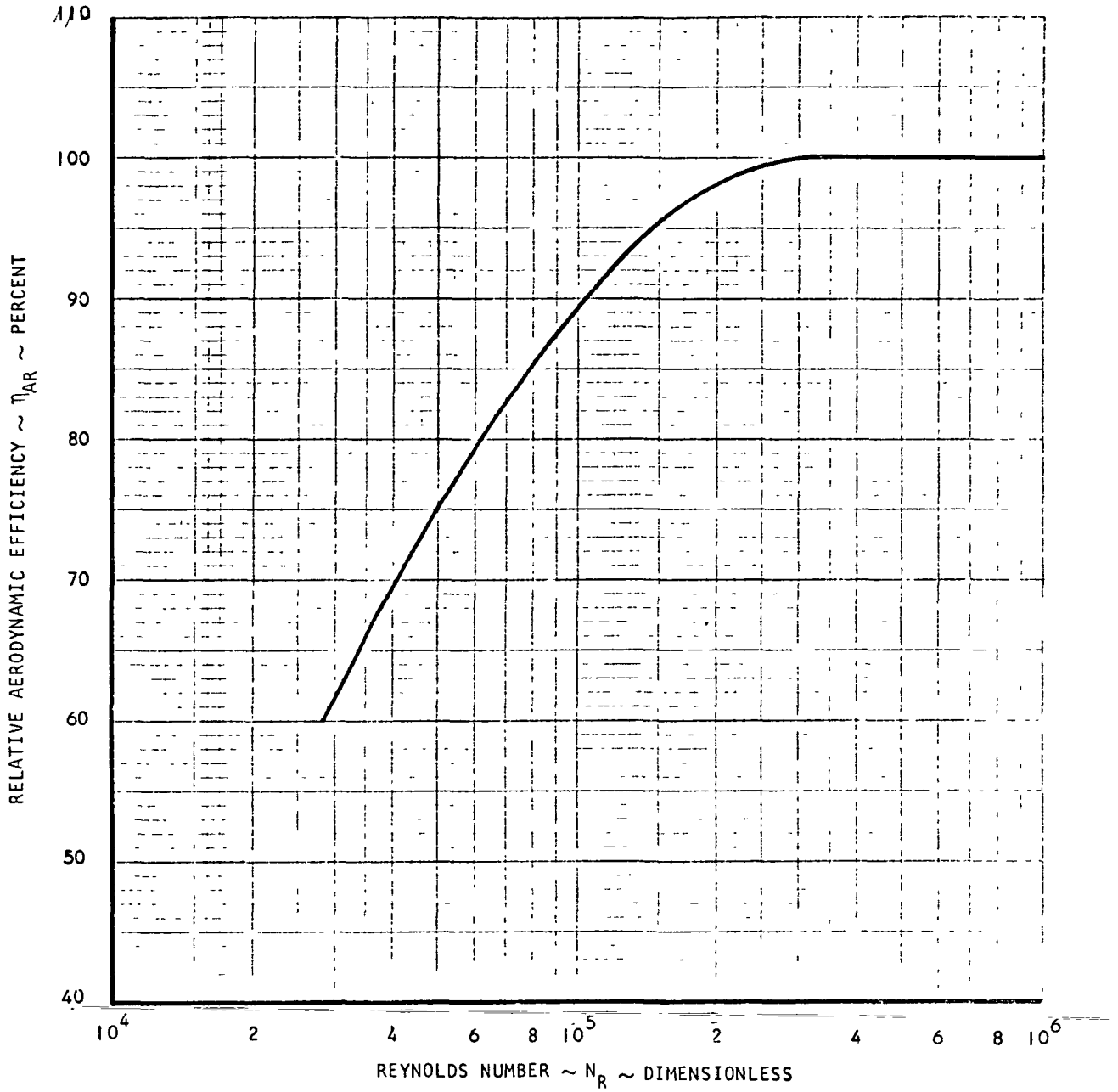
where: V = fluid velocity

C = characteristic dimension (blade chord length)

ρ = fluid density

μ = viscosity

It has been found that for the lower values of N_R, the fluid dynamic efficiency varies as some function of N_R. At higher values on N_R ($N_R \leq 3 \times 10^5$) the efficiency is a constant value (fig. 4-1).



S-73475

Figure 4-1. Fan Relative Efficiency as a Function of Blade Tip Reynolds Number

A preliminary analysis indicated that the required motor diameter was 1.125 in. (2.86×10^{-2}m). An existing fan impeller was available having a 1.125 in. (2.86×10^{-2}m) hub and a 1.95-in. (4.96×10^{-2}m) tip. This impeller was known to have an aerodynamic (fluid dynamic) efficiency of more than 80 percent. The impeller was designed for high head delivery as shown in fig. 4-2. Preliminary calculations showed an acceptable hub-to-tip ratio could be maintained by trimming the impeller tip diameter to deliver the required liquid hydrogen pumping performance. For this condition, the point of maximum aerodynamic efficiency on the fan performance curve, was selected. The flow rates at the liquid hydrogen and gaseous helium design points, 5.02 cfm (2.37×10^{-3} m^3/sec) and 5.34 cfm (2.51×10^{-3} m^3/sec) are nearly the same, but the ratios of pressure rise to fluid density are much different. This indicated that both a speed change and a shift in the operating point along the pressure rise curve would be required. It was initially assumed that N_R was sufficiently great that efficiencies would be the same in all the fluids under consideration (Air, LH_2 and GHe). The impeller diameters were selected on that basis. Later analysis showed this assumption to be approximately correct; the final analysis was conducted in which the effects of the Reynolds number on efficiency were considered.

The original fan calibration (fig. 4-2) was performed in air having a density of 0.0765 lb/ft^3 (1.22 kg/m^3). In order to be consistent, the pressure rises (ΔP's), of the mixer design fluids were corrected to the 0.0765 lb/ft^3 (1.22 Kg/m^3) density. To give the following $\Delta P/\sigma$ values where:

$$\sigma = \frac{\rho \text{ of fluid}}{\rho \text{ of calibration fluid}}$$

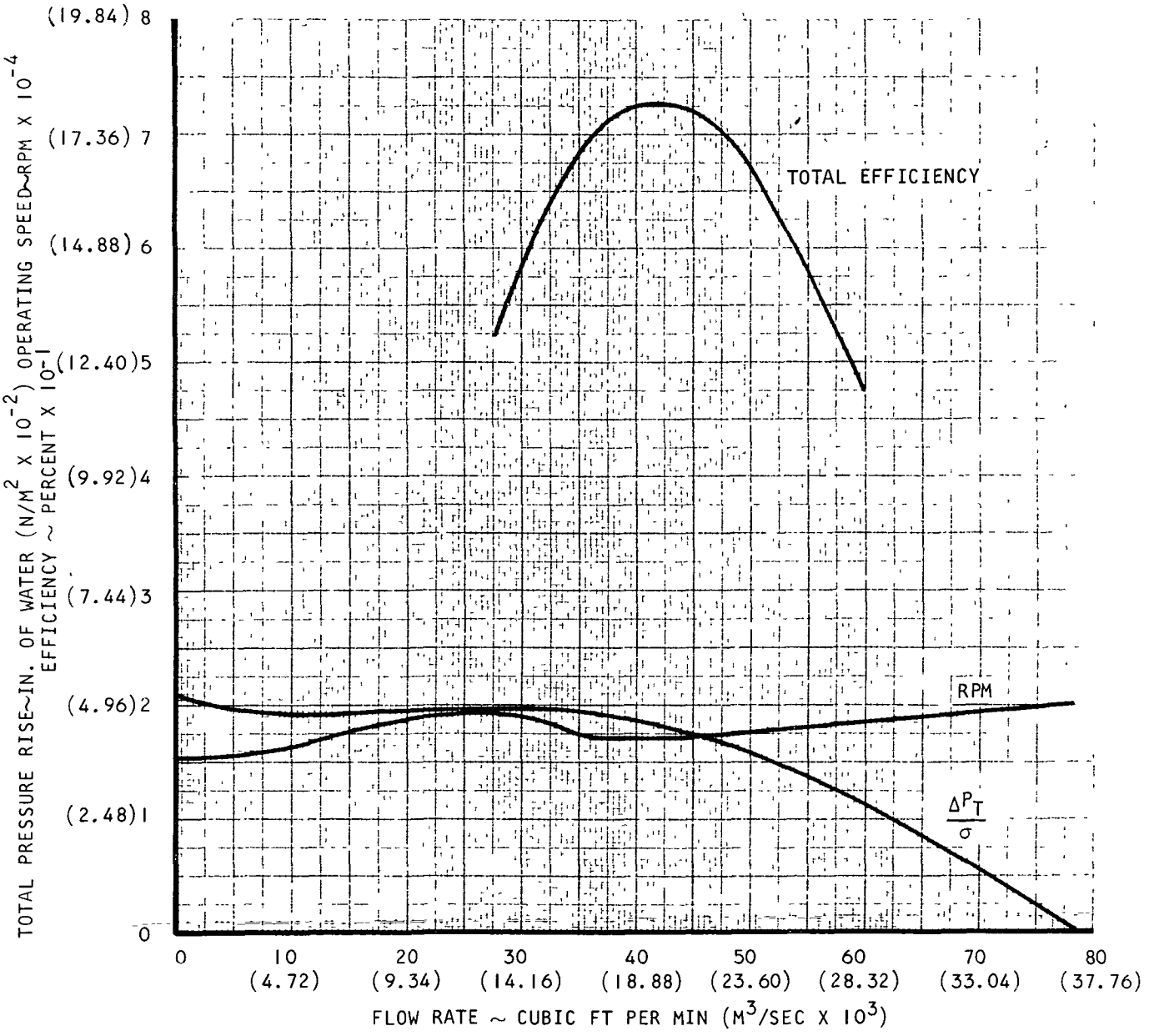
$$\sigma_{LH_2} = \frac{4.38}{0.0765} = 57.3$$

$$\sigma_{GH_e} = \frac{.179}{0.0765} = 2.34$$

$$\frac{\Delta P}{\sigma_{LH_e}} = \frac{2.0}{57.3} = 0.035 \text{ in. } H_2O \ (8.72 N/m^2)$$

$$\frac{\Delta P}{\sigma_{GH_e}} = \frac{0.2}{2.34} = 0.0855 \text{ in. } H_2O \ (21.3 N/m^2)$$

For mechanical reasons, it was found necessary to increase the impeller hub diameter to 1.235 in. (3.14×10^{-2}m) nominal.



S-73470

Figure 4-2. Performance of a Motor Driven Fan, PN 207640-9

The original flow area (annulus) of the impeller where $A = \pi/4\ (D_t^2 - D_h^2)$ was:

$$A = \pi/4\ (1.95^{-2} - 1.125^2) = 2.535(\pi/4)\ in^2\ (1.63 \times 10^{-3}(\pi/4)\ m^2)$$

The corrected area is:

$$A = \pi/4\ (1.95^2 - 1.235^2) = 2.275(\pi/4)\ in^2\ (1.467 \times 10^{-3}(\pi/4)\ m^2)$$

So the flow rates in fig. 4-2 must be reduced to $\left(\frac{2.275}{2.535}\right) = 0.898$ of those shown.

In selecting the stall point for operation in GHe the dump loss for the original fan was found for 35 cfm (1.65×10^{-2} m^3/sec) where:

$$V = \frac{Q}{A(60)}$$

For the annulus:

$$V = \frac{35\ (144)}{60\ (2.535)\pi/4} = 42.2\ \text{ft/sec}\ (12.86\ \text{m/sec})$$

$$P_v = 0.0962\ \rho V^2 = 0.0962\ (.0765)\ 42.2^2$$

$$= 0.4\ \text{in. } H_2O\ (99.5\ N/m^2)$$

In the duct:

$$Pv = 0.18\ \text{in. } H_2O\ (44.9\ N/m^2)$$

$$\Delta P_v = 0.4 - 0.18 = 0.22\ \text{in. } H_2O\ (54.7\ N/m^2)$$

Therefore, the stall point may be considered as 35 (0.898)= 31.4 cfm at a stage

$\frac{\Delta P}{\sigma} = 1.95 + 0.22 = 2.17\ \text{in. } H_2O\ (54.1\ N/m^2)$

Assuming an impeller tip diameter of 1.8 in. (4.57×10^{-2} m) for the mixer unit with the mixer discharging to a 1.9 in. (4.83×10^{-2}m) i.d. duct, the following values were found for the configuration of the mixer shown in fig. 4-3.

Motor Annulus Area = 0.01005 ft^2 (9.34×10^{-4} m^2)

Minimum Annulus Area = 0.0059 ft^2 (5.49×10^{-4} m^2)

Duct Cross Sections Area = 0.0197 ft^2 (1.83×10^{-3} m^2)

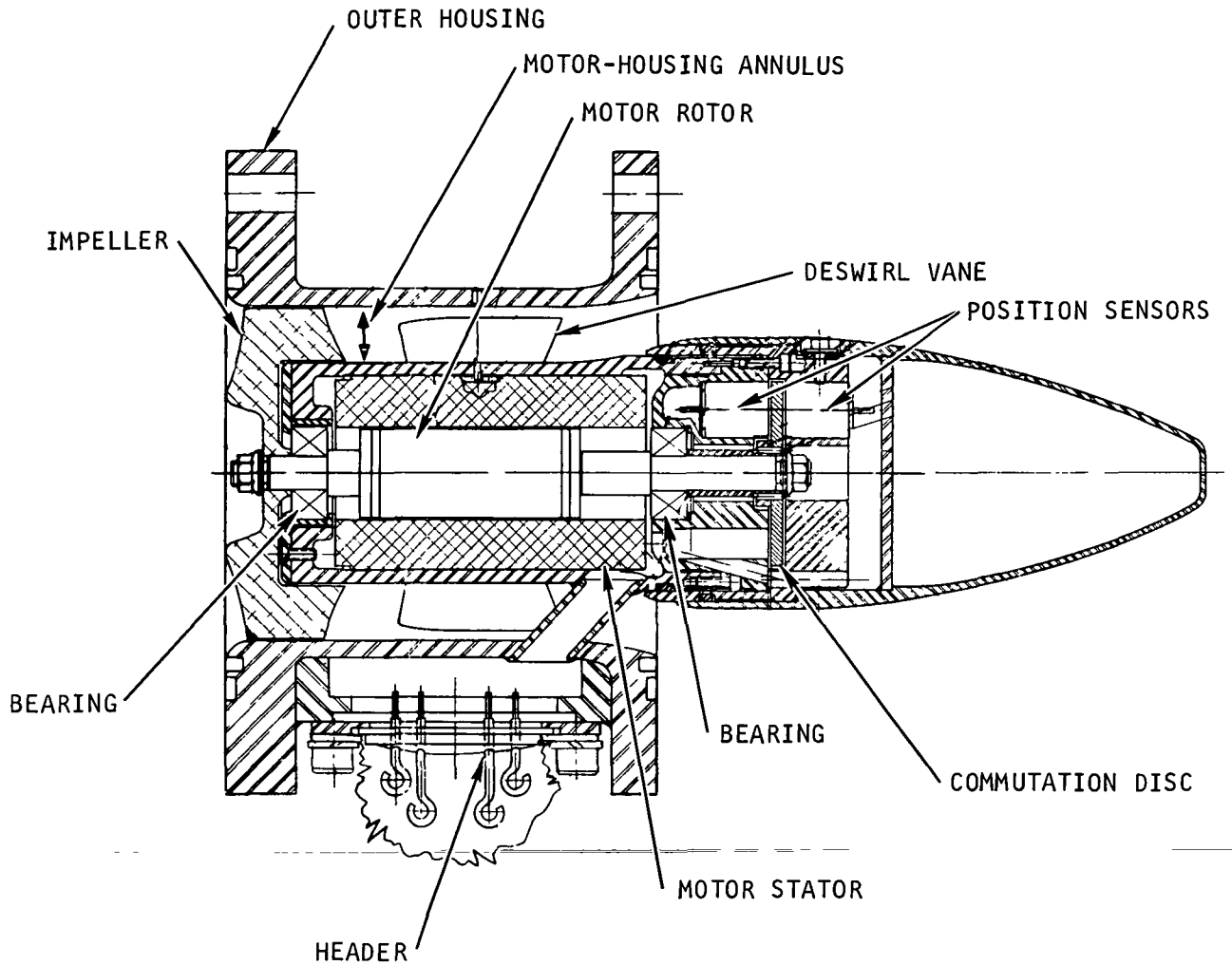


Figure 4-3. Cut Away View of Liquid Hydrogen Mixer Unit (Motor Control Electronics Not Shown)

when Flowing 5.3 cfm ($2.49 \times 10^{-3} m^3/sec$)

$\frac{Pv}{\sigma}$ (motor annulus) = 0.016 in. H_2O ($3.98\ N/m^2$)

$\frac{Pv}{\sigma}$ (min. Annulus) = 0.0465 in. H_2O ($11.57\ N/m^2$)

$\frac{Pv}{\sigma}$ (duct) = 0.0042 in. H_2O ($1.1\ N/m^2$)

For a 50 percent efficiency acceleration and deceleration of the fluid the losses are:

$$\frac{\Delta P}{\sigma} = [0.0465 - 0.016 + 0.0465 - 0.0042]0.5 = 0.035 \text{ in. } H_2O \ (8.71\ N/m^2)$$

So the stage $\frac{\Delta P}{\sigma} = 0.2 + 0.035 = 0.235$ in water ($58.6\ N/m^2$)

$$N = N_{cal} \left(\frac{\Delta P}{\sigma} / (\Delta \rho / \sigma)_{cal} \right)^{1/2}$$

$$N = 17{,}500 \left(\frac{0.235\ (1)}{2.17\ (2.34)} \right)^{1/2} = 3770 \text{ rpm}$$

$$Q' = \frac{N}{N_{cal}} Q_{cal \text{ corrected}}$$

$$Q' = \frac{3770}{17{,}500} \ (31.4) = 6.77 \text{ cfm } (3.2 \times 10^{-3} m^3/sec)$$

$$A_{annulus} = \frac{Q}{Q'} A_{impeller \text{ corrected}}$$

$$A_{annulus} = \frac{5.32}{6.78} \ (0.0124) = 0.00972 \text{ Ft}^2 \ (6.26 \times 10^{-4} m^2)$$

$$D_t' = 1.78 \text{ in. } (4.53 \times 10^{-2} m)$$

Considering thermal contraction:

$$\Delta D_t = \sigma_{AL} D_t' \ (T_{rm} - T_{LH2})$$

$$= 12 \times 10^{-6} \ (1.71) \ (530-37)$$

$$\Delta D_t = 0.010 \text{ in. } (2.54 \times 10^{-4} \text{m})$$

$$D_t = 1.79 \text{ in. } (4.55 \times 10^{-2} \text{m})$$

So the assumed 1.8 in. (4.57×10^{-2}m) tip diameter is considered sufficiently accurate.

The above calculations assume the fan efficiency flowing GHe is identical with that flowing air. Fan efficiency is dependent on Reynolds number. Fig. 4-1 is a plot of AiResearch experience using axial flow fans to determine the effects of N_R on relative efficiency. It may be noted that for values above $N_R = 3 \times 10^5$, no further increase in efficiency is achieved; the relative efficiency is 1.00.

The N_R of the original impeller in air and of the trimmed impeller operating in LH_2 and GHe at 37°R (20.5 K) were calculated. For these calculations, the velocity was taken as $\sqrt{U^2 + C_m^2}$.

For GHe with

$$U = \frac{\pi D_t (N)}{720} \text{ or } U = \frac{\pi (1.79)\ 3770}{720}$$

$$= 29.5 \text{ ft/sec } (8.99 \text{ m/sec})$$

and $$Cm = \frac{Q}{A \text{ impeller}} = \frac{5.321\ (144)\ 4}{60\ (2.275)\pi} = 7.15 \text{ ft/sec } (2.05 \text{ m/sec})$$

then $$V = \sqrt{29.5^2 + 7.15^2} = 30.3 \text{ ft/sec } (9.11 \text{ m/sec})$$

and $$N_R = \frac{CV\rho}{\mu}$$

$$= \frac{0.85\ (30.3)\ 0.179}{12\ (2.86)\ 10^{-6}}$$

$$= 1.35 \times 10^5$$

If we assume that for LH_2, N = 2700 rpm, then $N_R = 7.2 \times 10^5$

For the original fan in Air, operating at 18,000 rpm $N_R = 7.2 \times 10^4$

The corresponding relative efficiencies from fig. 4-1 are:

Air	~	83 percent
GHe	~	93 percent
LH_2	~	100 percent

Due to uncertainties of the properties present in actual operation and the large effects of relatively small variations in viscosity, it was decided to ignore the efficiency increase in GHe and to take only half the theoretical value for calculating the operating speed in LH_2.

In a manner similar to that used to obtain the GH_e operating speed, the LH_2 operating speed was found to be 2680 rpm, with the operating point corresponding to the 52 cfm (2.45×10^2 M^3/sec) point of fig. 4-2. The shaft torque required to drive the impeller for GHe is

$$T = \frac{1.59\ (cfm)\ \Delta P\ (10)^2}{\eta_f\ N}$$

$$= \frac{1.59\ (5.02)\ (0.235)\ 10^2}{0.685\ (3770)} = 0.073 \text{ oz-in. } (5.15 \times 10^{-5} \text{N-m})$$

Bearing torque per Barden Catalog M6 using R-3 bearings, 0.0004 in (1.016×10^{-6}m) radial clearance and 3 lb thrust load is 0.021 oz-in. (1.49×10^{-5}N-m). The motor torque for operation in GHe is $0.073 + 0.021 \approx 0.1$ oz-in. (7×10^{-5}N-m). Similarly the torque for operation in GH_2 was found to be 1.1 oz-in. (7.8×10^{-4} N-m) considering the effects of dump losses.

In preparing a motor problem statement, it was felt that there was considerable confidence in the calculated values for the (LH_2) operating point, but less confidence was felt in the GHe operating point near stall. Thus, a 1.1 multiplier was used to establish the GHe motor speed and torque design points, making the motor speed and torque design points as tabulated below:

Fluid	Rotational Speed rpm	Torque oz-in. (N-m)
GHe	4150	0.11 (7.8×10^{-5})
LH_2	2680	1.1 (7.8×10^{-4})

The mechanical design of the mixer was a straight/forward vane axial flow fan except for the following:

(a) Differential coefficients of thermal expansion in the materials selected had to be avoided or an allowance made for them.

(b) The physical size was such that very small hardware had to be used, particularly around the position sensors.

(c) The bearings were shielded to minimize the entry of contaminants and restrict the entry of liquid into the motor rotor chamber.

(d) Normal types of turbomachinery bearing lubrication such as oil and grease could not be used.

By using stainless steel for the rotor shaft, basic housing, endbells, and bearings, then, as the machine cooled to cryogenic temperatures, all parts tended to cool together. A spring was installed to provide a three-pound nominal preload to the bearings. The spring was sized to allow a 400°F (222°C) ΔT between the shaft and motor housing before the preload spring went solid. This prevented brinnelling of the bearing races by axial loading as the machine was cooled down. The bearings were fitted to the shaft with a zero-to-0.0004 in. (1.015×10^{-6}m) loose fit. The rear bearing was slip fitted to the endbell with a 0.0008-0.0014 in. ($2.03 - 3.55 \times 10^{-6}$m) clearance. This coupled with a radial play of 0.0008 to-0.0011 in (2.03 to 2.79×10^{-6}m) permitted a temperature increase across the bearing of more than 400°F (222°C). The front bearing was fitted with a resilient mount to permit some uneven shrinkage of the housing without putting brinelling loads on the bearings. The commutator disc on the shaft also had sufficient axial clearance to not contact the stationary sensors with a 400°F (222°C) ΔT, shaft to housing

The motor stator was wound with copper wire and used no iron for poles. A laminated iron flux shield was used at the o.d. of the stator in the area of the rotor magnet. The stator windings has an open weave glass cloth insulation on the i.d. and o.d. The o.d. insulation protected the motor windings from damage as the flux shield expanded and contracted at a different rate from the windings. The i.d. insulation served to keep the windings in place and insure that all windings were held in place by the encapsulant. The motor stator was encapsulated with Stycast 2850 ft compound having essentially the same coefficient of thermal expansion as the winding magnetic wire. Thus, appreciable tensile loading of the very fine No. 39 wire was avoided. The same encapsulant was also used in the position sensor coils to prevent winding failure.

The impeller was of die cast aluminum insuring ample clearance between the impeller tip and the housing i.d. The clearance per side between impeller and housing increased approximately 0.003 in. (7.6×10^{-6}m) at liquid hydrogen temperatures. The impeller is connected to the shaft by compression between the shaft nut and bearing inner race at room temperature. With the impeller rotor and bearings at liquid hydrogen temperature, the rotor shaft has a higher coefficient of thermal expansion that the bearings and shrinks more than the bearing. This insures that at low temperatures the shaft will slide in the bearings, minimizing problems of uneven thermal expansion. This means that the nut holding the impeller to the shaft moves toward the bearing approximately 0.00103 in. (2.62×10^{-6}m) while the impeller hub length shrinks approximately 0.0009 in. (2.29×10^{-6}m), increasing the force locking the impeller to the shaft. When being slugged with liquid hydrogen, it is possible for the impeller to cool much more rapidly than the shaft. If no other provision were made to lock the impeller to the shaft, it could become loose. The impeller bore and shaft tolerances have been selected such that the impeller bore shrinks to the shaft, insuring that it stays in place during cool down. The commutator disc is held in place in the same manner as the impeller, except it will not be colder that the shaft, so a transient condition

did not have to be considered. Due to the absence of a hub, the radial clamping force on it in liquid helium is somewhat greater than for the impeller.

The motor rotor is constructed of platinum-cobalt magnetic material, aluminum balance washers, and steel magnetic end shields. The shaft includes axially raised material from indentation which holds the rotor components to the shaft. This system allows some axial movement of the shaft during cooldown

O-Rings are used as static seals to restrict the entry of liquid hydrogen into the areas of the unit containing rotating components. Liquid in those areas would produce drag forces which would reduce the motor efficiency.

During assembly of the motor, it is necessary to adjust the position of the commutating disc relative to the magnetic poles. This is accomplished by achieving a proper wave shape on an oscilloscope while operating. Adjustment is accomplished by stopping the machine, loosening the commutation disc nut and rotating the disc. It is a trial and error procedure. A lack of space prevented a more convenient method of setting the commutation.

Electrical motor (brushless dc motor type).--The design of a brushless dc motor (BDCM) requires primarily the establishment of the magnetic flux which can be obtained. The motor capacity and the torque per ampere are related directly to the flux. The limit points of the speed torque curve can be predicted through the use of the following expressions.

$$\text{Speed, } N = \frac{(E-IR)\ (60 \times 10^{8})}{(\phi_p)\ (P)\ (\bar{z})} \tag{4-1}$$

$$\text{Torque, } T = 22.4\ (P)(\bar{z})(I)(\phi_p)(10^{-8}) \tag{4-2}$$

where

N = speed (rpm)

E = applied dc voltage at motor terminals

I = dc current amperes

ϕ_p = flux per pole (lines)

P = number of poles

$\bar{z}$ = conductors in series circuit

R - resistance of motor circuit

T = electromagnetic torque (in-oz)

Fundamentally, at no load, the current is negligible so the speed is established as that point where the back emf equals the applied voltage.

At stall conditions, there is no back emf so the applied voltage is equal to the IR drop across the motor winding. This current, at stall is limited only by the winding resistance.

$$I_s = \frac{E}{R_M}$$

where I_s = stall current (ampere)

R_M = motor winding resistance (ohms)

Under cryogenic operating temperatures the resistance of the stator winding becomes so small that too much current is drawn, the torque is too high and the proper speed-torque slope is not obtainable. It is necessary to include a line resistor to bring the total resistance seen by the applied voltage to the proper value. Thus, for low temperature operation:

$$R_T = R_M + R_S \text{ and } I_s = \frac{E}{R_T}$$

where R_S = shaping resistance (ohms)

R_T = total resistance (ohms)

The desired speed-torque curve is defined in the problem statement by the requirement for two precise design points. The speed-torque characteristic for this type of permanent magnet (PM) motor is a straight line, thus the required performance line can be seen on fig. 4-4.

Magnetic flux and the number of poles are the result of design decisions made to optimize in tank efficiency of the motor. The selection of PM excitation eliminates any field losses and increases overall reliability. The selection of Platinum-Cobalt for the permanent magnet material with its high magnetic coercive (mmf) capability permits the use of an "ironless" stator which eliminates stator tooth losses and allows maximum stator copper cross section which reduces the I^2R losses to a minimum. This type of construction greatly reduces motor reactance and consequently reduces the stored energy in the windings at the time of switching; this produces large reductions in switching transients. The use of six pole magnetization keeps the stator winding end turn length down, which is also a considerable advantage in limiting the winding resistance. The use of a brushless machine is, of course, mandatory because of the environment. The BDCM configuration selected yields the best possible efficiency for the application, commensurate with reliability and cost.

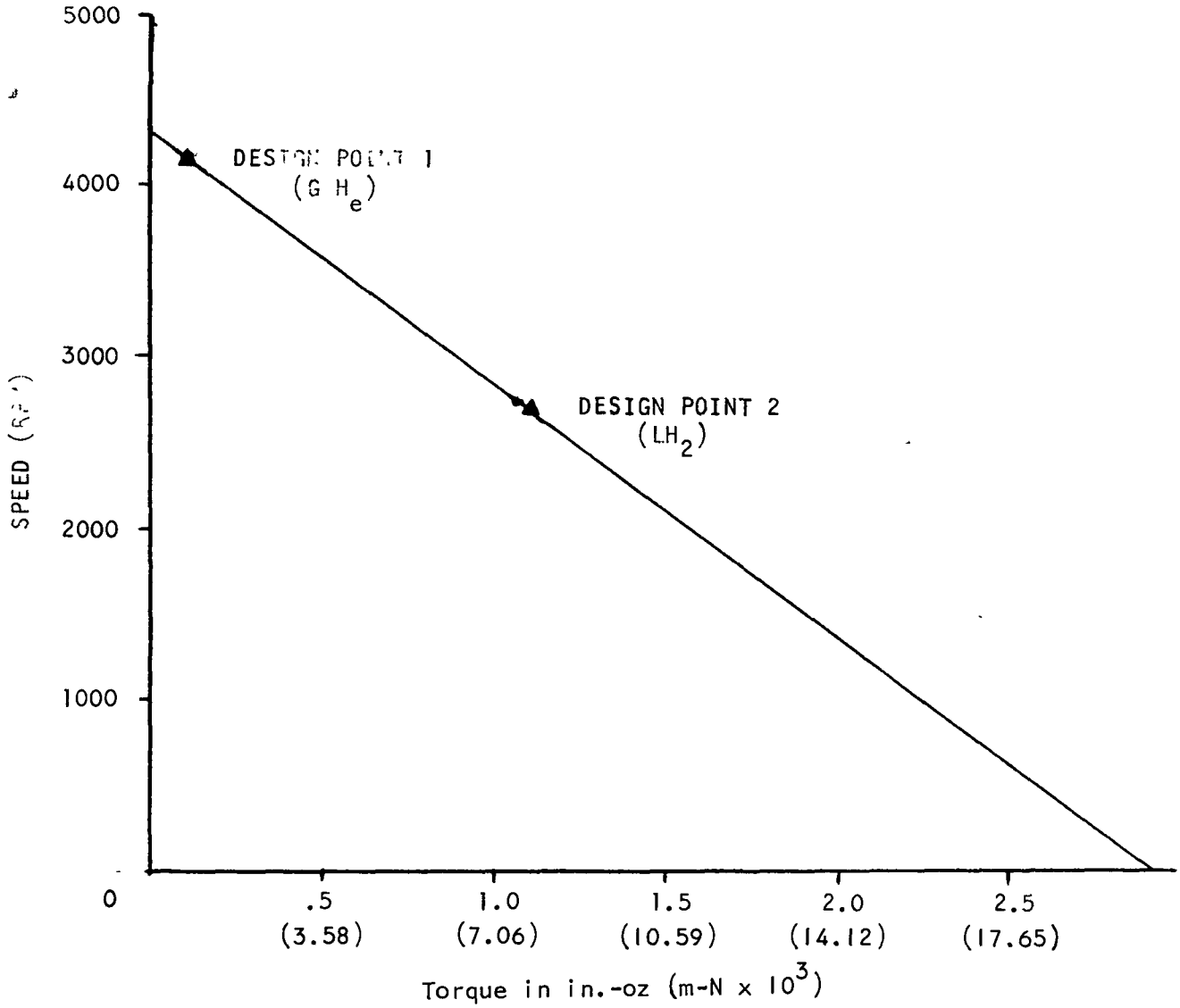


Figure 4-4. Speed-Torque Characteristic for BDCM Unit

The magnetic flux available is established from the magnet pole area which can be achieved and the flux density obtainable from the Pt-Co magnet material working into the permeance of the "ironless" stator. The effective flux per pole is 1935 lines. Using eq. 4-1, and an applied voltage, effective at the motor, of 25.5 V, the required conductors Z can be calculated for the no load speed of 4300 rpm (fig. 4-4). The slope of the speed-torque curve is dependent strictly on effective winding resistance. The effect of voltage variations is to move the entire curve higher or lower, but maintain the same slope. Because of the need for an external resistor at the cryogenic temperatures, it can be seen that a trimming of the motor speed-torque line is possible with slight adjustments to the input voltage and external resistor. This permits an exact match with the fan characteristic. Fig. 4-5 graphically shows the effects of voltage and resitance variations.

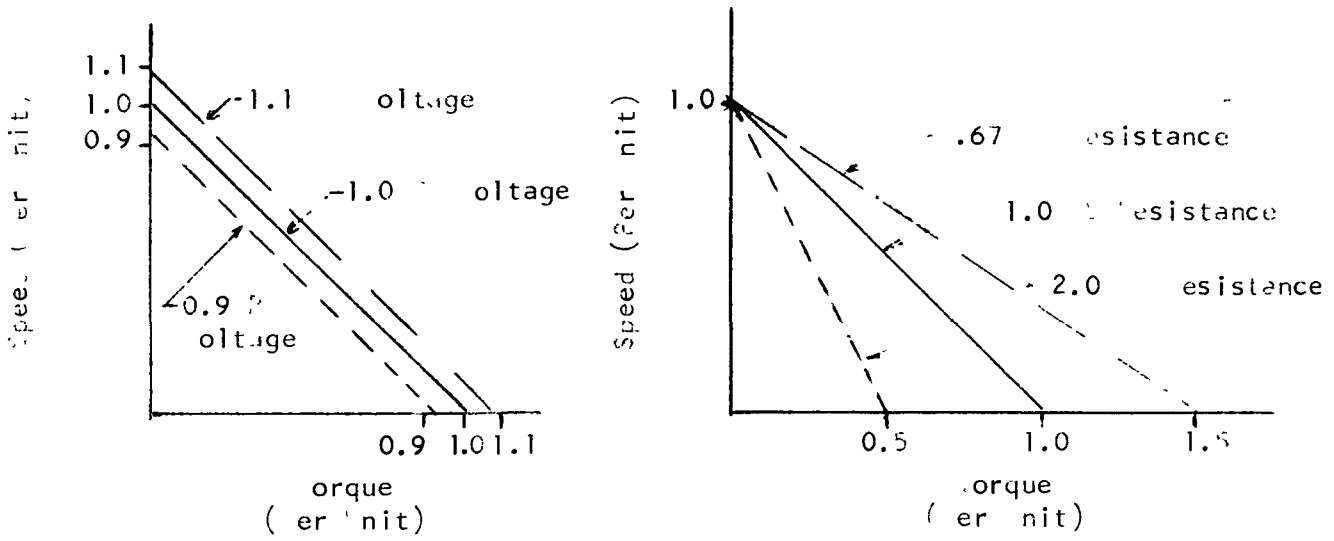


Figure 4-5. Effect of Voltage and Resistance Variations

With the number of conductors established and the cross sectional area available for the conductors determined from the geometry of the system, the wire size and winding resistance are determined. These parameters calculate as:

Z = 3000 conductors per phase

wire size = No. 39 A.W.G.

R/phase = 366 Ω @ 68°F

Referring back to fig. 4-4 again, the desired stall torque of 2.9 in.-oz is established. The current necessary to develop that torque can be calculated from eq. 4-2

$$I_s = \frac{2.9 \times 10^8}{(22.4)(6)(3000)(1935)} = 0.372 \text{ A}$$

The total resistance necessary to obtain this current at stall, using E - IR = 0 is then.

$$R = \frac{E}{I} = \frac{25.5}{.372} = 68.5\ \Omega$$

The total resistance, with the stator windings at 37°R, must be made up to this 68.5 Ω level. The motor winding resistance at this temperature is less than 5 percent of the total required resistance. It is recognized that the

higher motor currents will result in heating of the stator which will increase stator resistance. However, this is considered a second-order effect and is probably not detectable within the limits of instrument accuracy.

The electromagnetic losses were then predicted. Because of the low absolute magnitude of the losses, good accuracy in the calculations was difficult to obtain. The motor electromagnetic losses consist of copper loss I^2R, eddy current loss in the conductors, iron loss in the flux containment sleeve, and stray load losses. The motor electromagnetic torque is also decreased by the windage and friction loss before the resultant output shaft torque is achieved. An inductive loss relating to the motor winding inductance and the current at the time of switching (LI^2) does not occur in the motor but is attributable to motor characteristics.

The motor consists of two basic parts, a stator assembly and a rotor assembly. The stator assembly utilizes a two phase bifilar winding which is connected into a four phase configuration, see fig. 4-6. Only one phase is energized at a time with the exception of a slight overlap at the switching point. This means of excitation is referred to as half wave. The advantages for this type of system lie primarily in simplification of the electronic switching circuitry. There is need for only a single series switching device per phase. Other systems, where full wave or reversal currents are employed, need four switches per phase thus even if a three phase winding were used 12 switches with their associated circuitry would be needed. This decreases the efficiency and reliability of the electronic controls. Thus, the half wave motor effects an increase in overall reliability at a very small cost in motor efficiency.

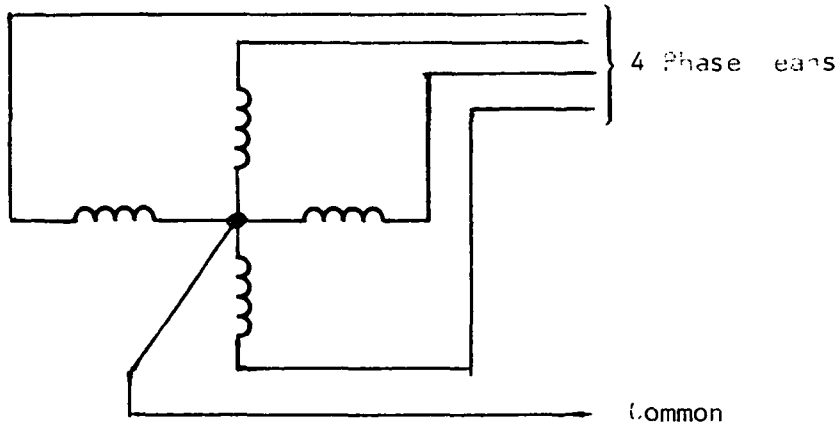


Figure 4-6. Stator Winding

The use of four phases provides a smoother torque pattern as a function of rotor position than three phase and it is wound as a conventional two phase unit with stranded conductors. These strands are subsequently separated and reverse connected to give the four phase configuration.

Only those conductors which are in proper relationship to react with maximum effect with the magnetic field are energized. The current flowing through those conductors located in the magnetic field results in an electromagnetic torque on the rotor. This torque causes the rotor to rotate with respect to the stator. To maintain motor torque with the new rotor position, the next group of conductors in the direction of rotation is energized and the others turned off. This process continues throughout the full rotation of the rotor.

The second basic electromagnetic part is the rotor. It consists of a cylinder of platinum-cobalt permanent magnet material mounted on a shaft. The fundamental reason for the use of permanent magnet excitation was discussed earlier. The specific use of platinum-cobalt deserves some further explanation. At the time of the development of this motor (1968), platinum-cobalt was one of two magnet materials exhibiting an energy product as high as 10.0 million gauss-oersteds, the other material being Alnico 9. The significance of the high-energy product is that the work obtainable from a particular volume of material is maximum. Of these two magnet materials, platinum-cobalt is the only one capable of working into large effective air gaps because of its resistance to demagnetization (high H_c). Within the last two years new permanent magnet materials have been developed. These are the rare earth-cobolt alloys. The higher magnetic quality versions are samarium-cobalt and are capable of achieving energy products in the 15 to 20 million gauss-orsted region. These new alloys are magnetically superior to the platinum-cobalt material in all aspects: energy product, coercive force, and residual induction. Thus some consideration could now be given to its use in future versions of this motor. The mechanical properties of platinum-cobalt are easily the best of any respectable permanent magnet alloy. The rare earth-cobalt alloys exhibit physical properties similar to Alnico 9; they are brittle, tend to crack or chip and have no appreciable tensile strength. Platinum--cobalt is still the only good magnet material with isotropic characteristics. That is to say, its good magnetic properties are not restricted to a particular axis. To date, the rare earth-cobalt alloys as well as Alnico 9 are anisotropic. This combination of magnetic and mechanical properties probably still makes platinum-cobalt the best magnet material for this application. The magnet cylinder is all that is required, whereas the rare earth-cobalt approach would need magnet segments and a nonmagnetic support ring and end plates. The necessity of providing support for a rare earth-cobalt magnet assembly has a detrimental magnetic effect in that it would increase the effective air gap and thus negate some of the benefits of better magnet properties. A composite rotor would cause considerable problems in maintaining part fits over wide temperature ranges encountered in assembly and use.

Electronic motor control module principles of operation.--The block diagram of a four-phase half-wave brushless dc motor and of its associated electronics is shown in fig. 4-7. Each motor winding is represented by its generated voltage (counter-emf) e_g, its winding resistance R_M, and its winding inductance L.

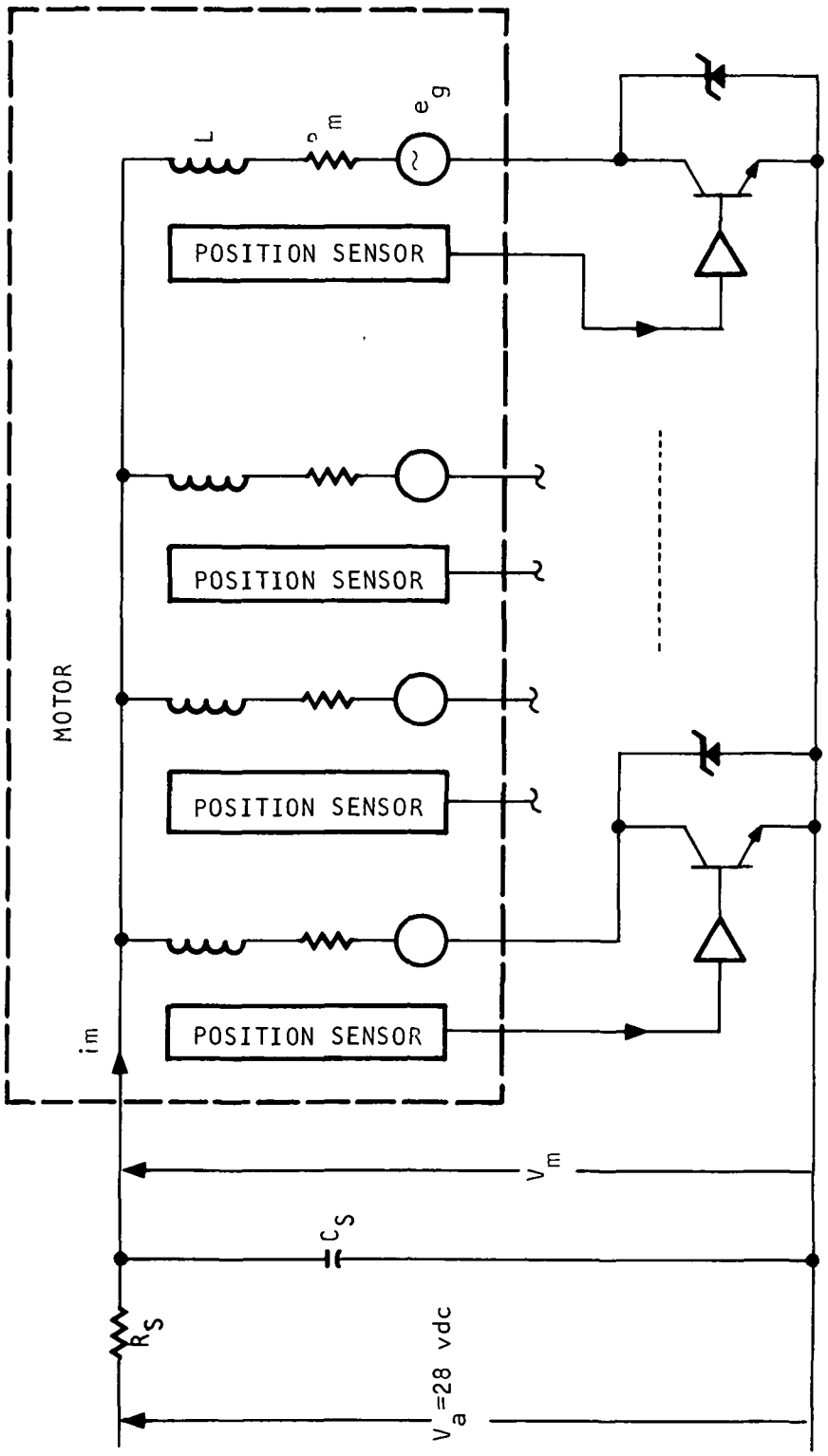


Figure 4-7. Block Diagram, Motor and Electronics

In addition, each winding is coupled to each other winding, thereby introducing an additional voltage $e = M \frac{di}{dt}$ which is significant to the understanding of the observed voltage waveforms, but which otherwise has no effect on the operation because only one winding conducts at a time. For simplicity only two of the four amplifier (switching) stages are shown. The resistor R_S is used in this particular application only in order to shape the torque-speed characteristic, as previously discussed. The capacitor C_s is used to assure a dc voltage at V_M in the presence of a pulsating motor current i_m. The capacitor is not needed for the operation of the machine; however, it greatly simplifies the instrumentation needed for the separation of losses required in order to determine the in-tank efficiency of the motor. Operating the machine with and without the capacitor revealed no measurable difference in speed or current under load; it was therefore concluded that the capacitor did not materially change performance. The entire subject of instrumentation is detailed in Appendix B of this report.

Fig. 4-8 depicts the waveforms that would be associated with a motor free of inductance. This assumption is reasonably correct for the ironless motor under consideration. The effects of inductance will be qualitatively discussed later.

Fig. 4-8(a) depicts the voltages that exist across the non-conducting switches (transistors). These voltages consist of the motor generated emf subtracted from the voltage V_M applied to the motor. Fig. 4-8(b) tags the switch which is closed at any particular instant. It can be seen that each switch conducts sequentially for 90 electrical degrees during that part of the cycle when the generated voltage in the associated winding is maximum, i.e., when the voltage across a non-conducting switch would be minimum. Fig. 4-8(c) shows the resulting scalloped motor current.

The timing and duration of switch conduction is controlled by the position sensors as a function of the relative position of rotor poles with respect to the stator windings. Proper functioning of the position sensors is critical to the performance of the motor, as can be seen in fig. 4-9. A position sensor correctly set for a four-phase motor is shown in fig. 4-9(a). Conduction is symmetrical for $\pm \frac{\pi}{4}$ radius about the generated voltage peak.

At any given speed, the instantaneous voltage generated by the motor is given by:

$$e_g = Egm \cos \omega t = Egm \cos \theta,$$

where Egm is directly proportional to speed. The instantaneous current in a conducting winding is:

$$i_m = \frac{V_M - e_g}{R_M} = \frac{V_M}{R_M} - \frac{Egm}{R_M} \cos \theta,$$

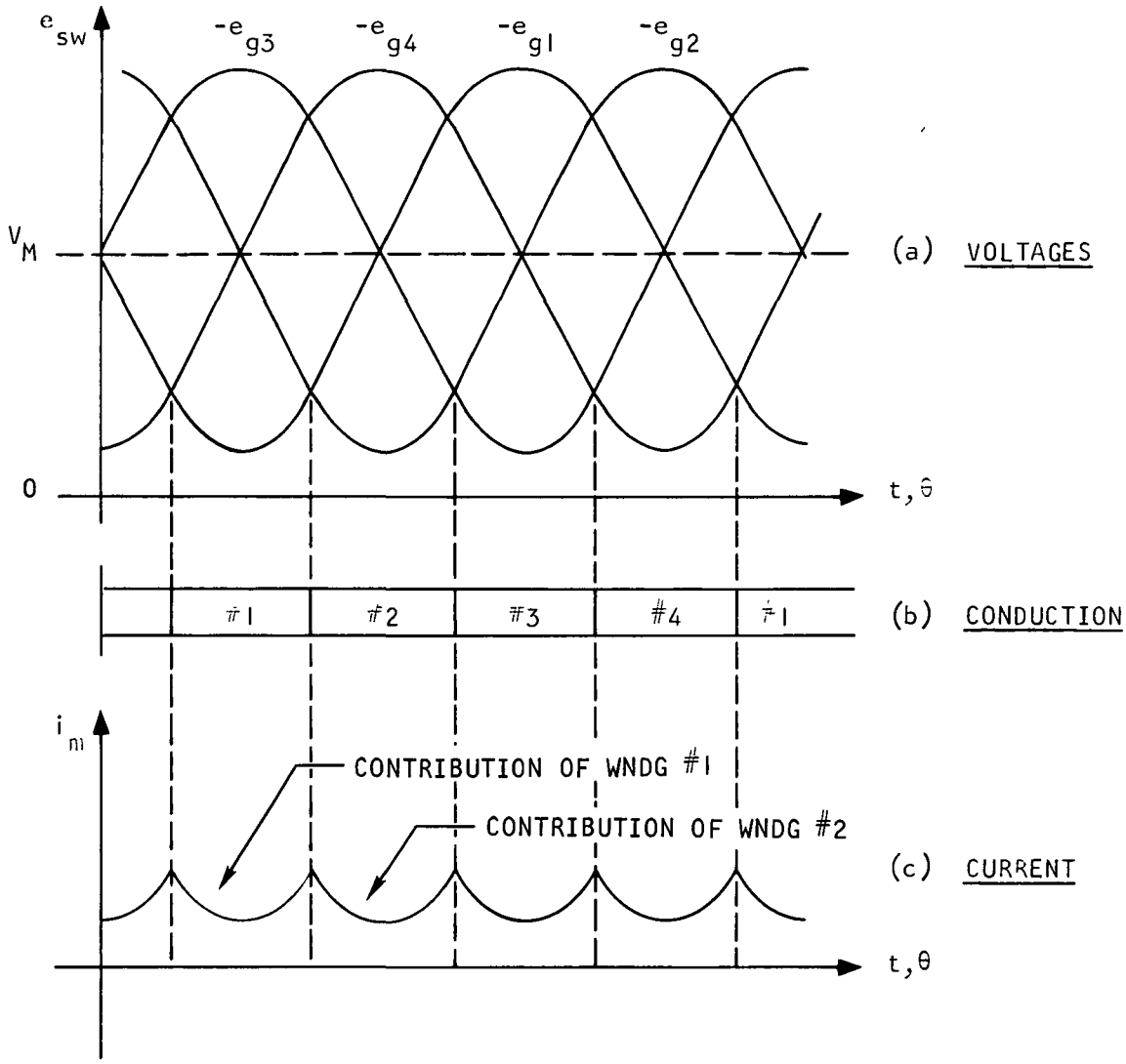
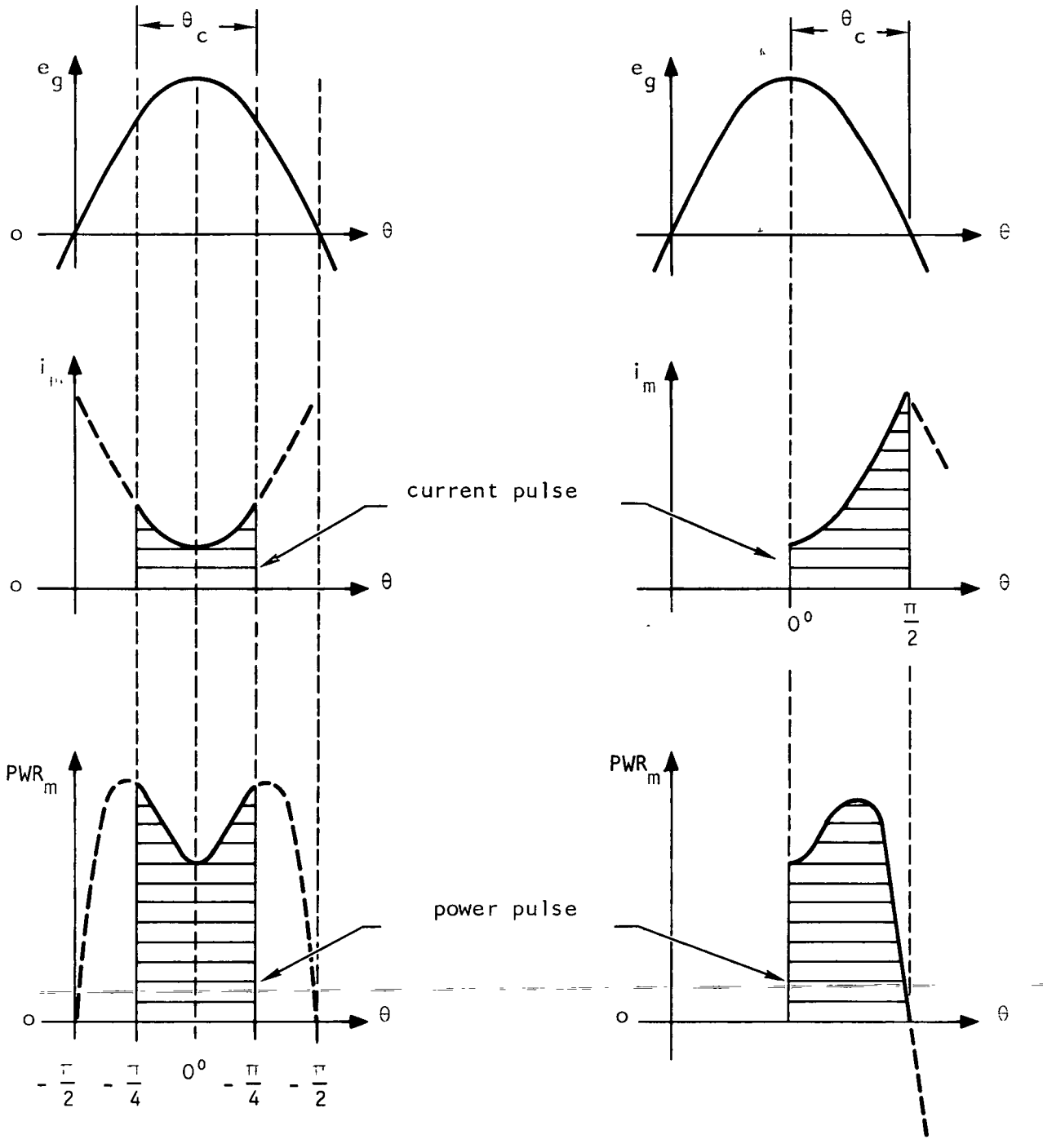


Figure 4-8. Waveforms in an Inductance-Less Motor



(a) Correct Setting

(b) Retarded conduction interval

Figure 4-9. Effects of Position Sensor Setting

from which the instantaneous mechanical power developed by the motor becomes

$$P_m = i_m e_g = \left[\frac{V_M}{R_M} - \frac{Egm}{R_M} \cos \theta \right] Egm \cos \theta.$$

Refering to fig. 4-9(a), it can be seen that as the conduction angle θ_c is increased symmetrically about 0^0, the instantaneous mechanical power increases until a peak is reached at just before 120^0 (three-phase operation), from where it then decreases sharply to zero. The ratio of instantaneous power to instantaneous current follows the e_g curve, and this is highest at $\theta_c = 0$, and is zero at $\theta_c = 180^0$, i.e., the high current at the end of a pulse produces no torque at all. Thus the selection of conduction angle is a trade-off between efficiency and a reasonable number of phases and their associated electronics channels. The four-phase configuration used at AiResearch represents a good compromise, and may well be optimum when all factors are considered.

Fig. 4-9(b) shows the condition situation resulting from a 45^0 (electrical) shift of the conduction angle. In a six-pole machine this corresponds to 15^0 mechanical. It can be seen, that although a respectable power pulse is obtained, the current has increased greatly, reducing the efficiency of the machine. A further shift would result in negative, i.e., retarding power, until at a 30^0 (mechanical) shift, the motor produces no power yet draws stall current. Experience operating this motor indicates the shutter should be set to within approximately three mechanical degrees for essentially optimum performance.

It is clear that the proper operation of the position sensors is especially critical to performance of this motor in order to minimize its in-tank I^2R losses. Since the position sensors operate immersed in the cryogenic fluid, their design and test comprised the major portion of the electronics development effort.

The effects of motor inductance are considered with the aid of fig. 4-10, which is a photograph of motor waveforms taken during operation in liquid nitrogen during the development tests. The upper waveform shows the current pulse. The effect of the inductance is to slow the current rise and to shift the phase of the sinusoidal portion. The effect is small due to the low value of inductance associated with the ironless winding of the AiResearch motor. The lower waveform is the voltage across the phase-A transistor, shown inverted due to the instrumentation setup. It is noted that the waveform is distorted. This is due to $M \frac{di}{dt}$ contributions of the other phases. In the first segment, for example, the contribution is from phase-B conduction.

The voltage spikes are by-products of motor commutation, and are the result of rapid current decay in L_w, the winding self inductance. The switching transistors are protected by zener diodes against the harmfull effects of these spikes. Referring to fig. 4-10, the second spike seen after the conduction interval is coupled from phase-B, and the third spike from phase-C. The latter is clipped at the zero axis by forward conduction of the zener; it is more

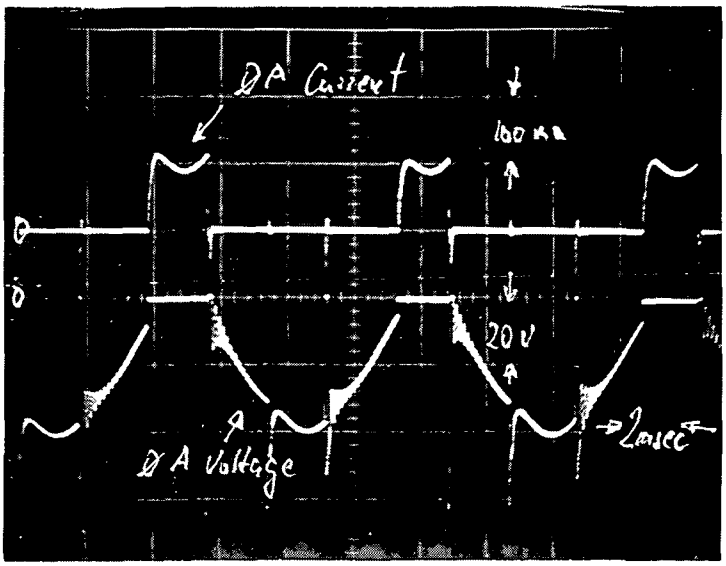


Figure 4-10. Motor Waveforms in LN_2 Speed 2730 RPM, 28 vdc Power Supply, 70 Ohm External Resistance

F-18432

pronounced than the previous spike because phases A and C, by the nature of the winding, are very tightly coupled. The winding is basically a two-phase bifilar type. Two of the four phases required are obtained by reverse connecting half the conductors in the original phase A. These reversed conductors are designated phase C and are 180 electrical degrees out of phase with the remaining conductors in phase A. While these conductors now represent two phases, they are intermingled in the same coil which results in the tight electrical coupling. Phases B and D are handled in the same way, creating the four phases 90 electrical degrees apart. The phase D spike is not seen because it takes place slightly after the start of phase A conduction and would therefore not reflect itself on phase A, being in effect filtered out by the power source.

If I_c is the motor current just prior to commutation, then the energy stored in the winding inductance is:

$$E = \frac{L_w I_c^2}{2} .$$

This energy is transferred, principally to the zeners, during the commutation process, and thus represents a power loss of:

$$PWR_c = \frac{L_w I_c^2}{2} \times f_c$$

where f_c is the number of commutations per second, i.e.,

$$f_c = \left(\frac{rpm}{60}\right) \times \frac{P}{2} \times (\text{number of windings}) = \frac{rpm}{5} .$$

The inductance of the motor winding was measured to be 14.5 mH, thus, for the particular conditions of fig. 4-10·

$$PWR_c = \frac{14.5 \times 10^{-3} \times (.11)^2}{2} \times \frac{2730}{5} = 48 \times 10^{-3} \text{ W.}$$

Position sensor development.--Virtually no data were available on performance of position sensing devices at these temperatures. Therefore, analytical and laboratory investigations of the following types of devices were performed:

Variable Q oscillator

Solid state optical light emitter and detector pairs

Variable magnetic reluctance units

The basic application of the position sensors described herein requires the use of a shutter disc or cup. This commutation device is secured to the motor shaft and is provided with indexes that serve as position indicators.

An analysis of the optimum number of sensors showes a four-sensor system to be most advantageous. From a circuit standpoint, a minimum of two sensors could be used, however, this approach would increase the complexity of the interface electronics between the sensor outputs and the main transistor switches. Moreover, if one sensor failed, the motor would stop and would not be restartable.

The four-sensor system has two distinct advantages. First, if one sensor failed, the motor would continue to operate, and, if stopped, it would have a 75-percent chance of starting.

To facilitate the initial development and testing program for the various sensors, work was done at room ambient and at liquid nitrogen temperatures. The selection of liquid nitrogen was based on two factors: (1) it was easily obtainable and posed no major personnel hazard due to evaporation, and (2) its temperature, from a gross viewpoint, is nearly the same as liquid hydrogen, (-198^0 and -256^0C, respectively). Therefore, the effect of thermal stress due to immersion was nearly the same and was adequate for the early test period.

The variable Q oscillator circuit was originally developed to measure the linear displacement of metal surfaces. The circuit used an oscillator in which the ac signal level is a linear function of the spacing between the oscillator coil assembly and a metal surface. The oscillator output voltage is demodulated into a dc analog of displacement. For purposes of this application, the circuit was modified to provide for on-off switching. The resulting circuit, as shown in fig. 4-11 was used for the tests described herein. The oscillator requires a high-Q inductor in order to sustain oscillations. If the inductor Q is sufficiently reduced, oscillations stop.

For the purpose of testing the commutator performance, a notched aluminum disc and a sensing coil were mounted in a test fixture. The disc was driven by a dc motor at speeds varying from 1000 rpm to 13 000 rpm. Fig. 4-12 shows the relative position of the chopper disc and a 1/8-in. coil which demonstrated the best performance of the four different sensing coils tested. The disc had four 45^0 notches equally spaced around its periphery. At the maximum motor speed this provided a chopping rate of approximately 900 Hz. The inductor coil, having dimensions compatible with the motor, consisted of 30 turns of 50 gage wire on a 0.125-in. (3.3×10^3m) bobbin. The coil was encapsulated in a porcelain filled epoxy in order to minimize the dissipation factor at the 3 mHz oscillation frequency.

The commutator performance was observed over a range of -320^0F (-196^0C) to $+215^0$F (102^0C). The duty cycle of the commutator varied with both speed and temperature. The "on" period decreases with both increasing speed and temperature. Operation was observed to be very sensitive to circuit adjustment and coil to disc gap. For proper operation the gap had to be held to within 0.005 and 0.010 in. (1.3×10^{-4} to 2.5×10^{-4}m).

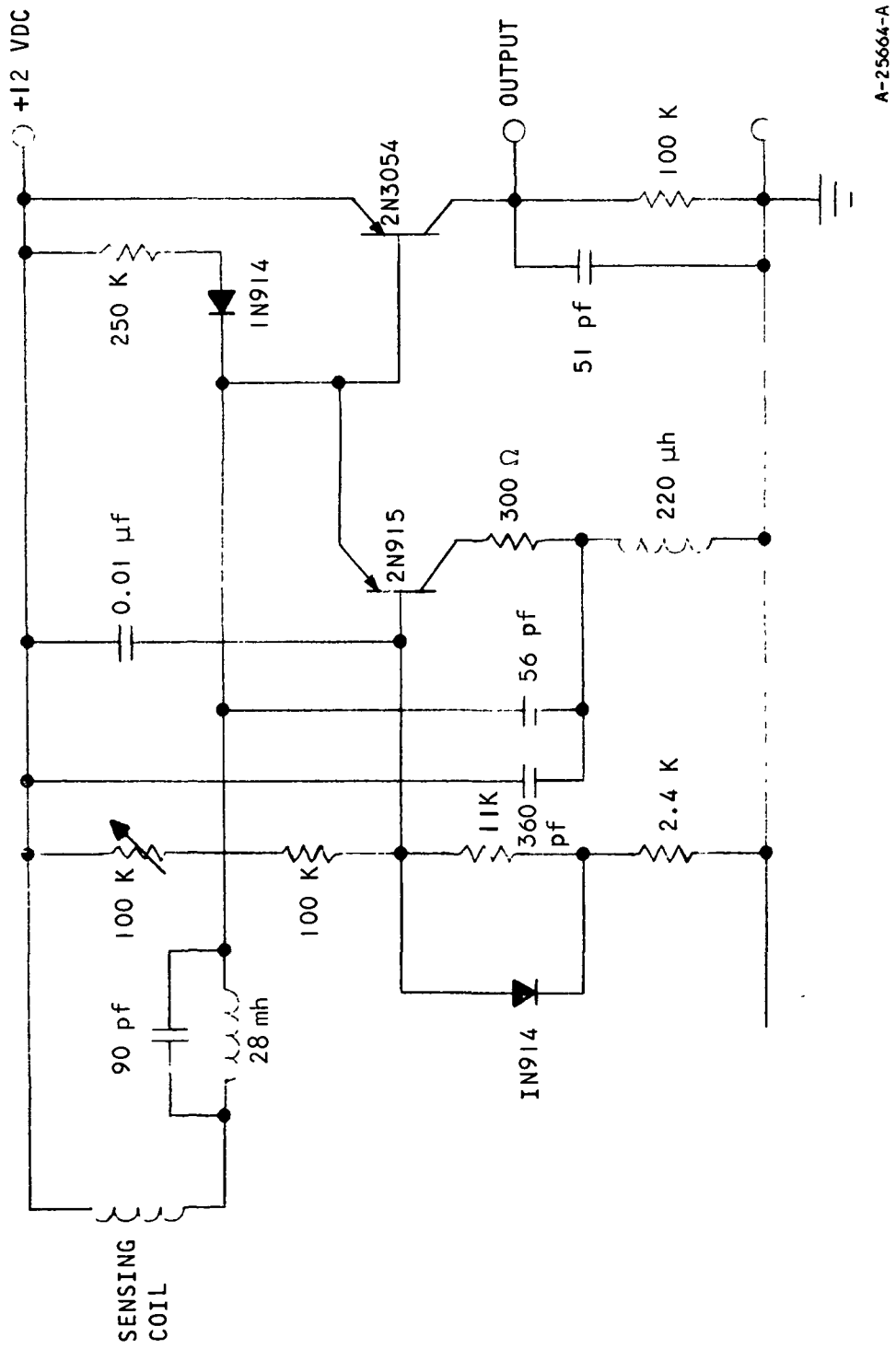


Figure 4-11. Variable Q Switching Oscillator

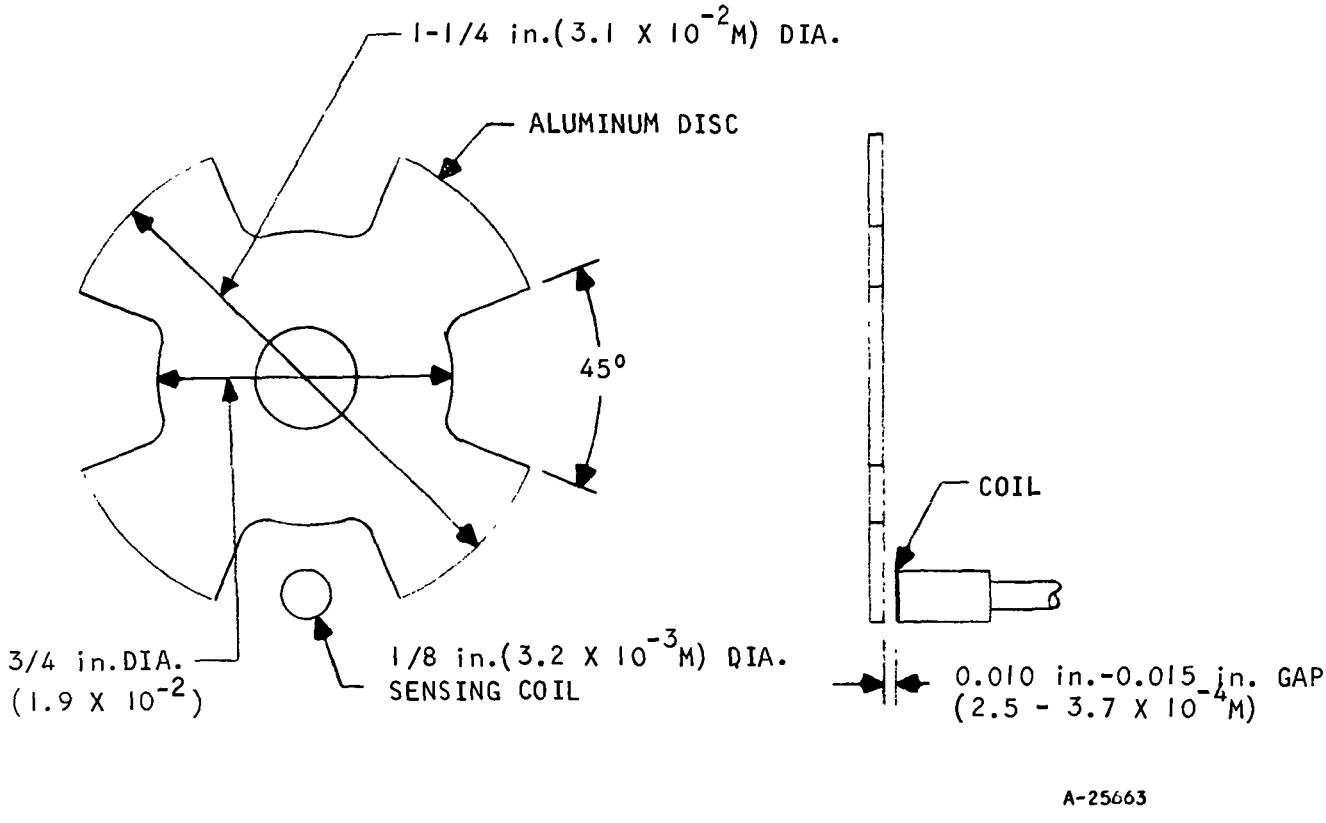


Figure 4-12. Arrangement of Commutator Coil and Disc in the Test Fixture

In addition to complexity and the requirement for four coaxial cables to connect the motor to the electronics, the circuit proved too critical to be considered for this application. A plot of inductor Q vs gap length shown in fig. 4-13. The contraction of stainless steel from +25°C to -256°C is 0.003 in./in. Thus, for a 3-in. motor shaft an allowance of 0.009 in. has to be made. This, combined with manufacturing tolerances indicates that the gap would have to approach 0.020 in. (5.1×10^{-4}m) to preclude possibilities of binding. A glance at fig. 4-13 shows that at this gap the Q-ratio would be 21/15 = 1.4, obviously too low for reliable operation. For this reason the variable Q oscillator was considered unsuitable for this application, and was abandoned.

The consideration of field effect devices for this application developed from work done on the optical position sensor. Historically, AiResearch brushless dc motors used (and still use) a photo-electronic pair per winding in order to develop the logic signals required to switch the solid state commutator. This method has the advantages of simplicity, low parts count, and precision. Normally this pair consists of a solid-state infrared emitting diode and of a bi-polar photo transistor pickup; this works well over the normal temperature range associated with bi-polar transistors, say -55°C to +85°C, where the upper limit is imposed primarily by the current state of the art of Gallium Arsenide light emitters. At cryogenic temperatures, however, the situation is somewhat different. The photo transistor is a minority carrier device. Photons impinging on the collector to base junction region generate a current which acts in the same manner as the base current acts in any bi-polar transistor. Thus, just as the gain of a "normal" silicon transistor decreases rapidly with decreasing temperature, so does the sensitivity of the photo transistor decrease rapidly with temperature. An additional factor in this sensitivity decrease is the dimunition of photocurrent with decreasing temperature. At the time this project commenced, it was felt, that, at low temperatures, the decrease of detector efficiency would not be sufficiently offset by the increase in the emitter's quantum efficiency. Thus, an alternate optical approach, using photofets, was investigated. The photofet, like other field effect devices, is a majority carrier device, and thus its temperature characteristics are determined by different phenomenae. Specifically, the devices should operate quite well at low temperatures.

The basic components of this position sensing system are a solid-state light emitter and a corresponding light detector. The emitter considered was a P-N planar gallium arsenide (GaAs) diode (TIXL09) manufactured by Texas Instruments. The detector considered was a field-effect transistor with an integral lens (FF600) manufactured by Crystalonics Incorporated. Electrically, the two devices are connected as shown in fig. 4-14. Current conducted through the GaAs diode causes it to emit a narrow beam of light at a wave length of approximately 0.90 A. The photofet has a matching spectral response and has been optically optimized to focus the light entering the lens directly upon the gate junction area. When this radiated energy strikes the gate area, a proportionate amount of gate current is generated. The gate current generates a voltage in the gate return resistor, the photofet amplifies this voltage, and a large output signal (drain current change) results.

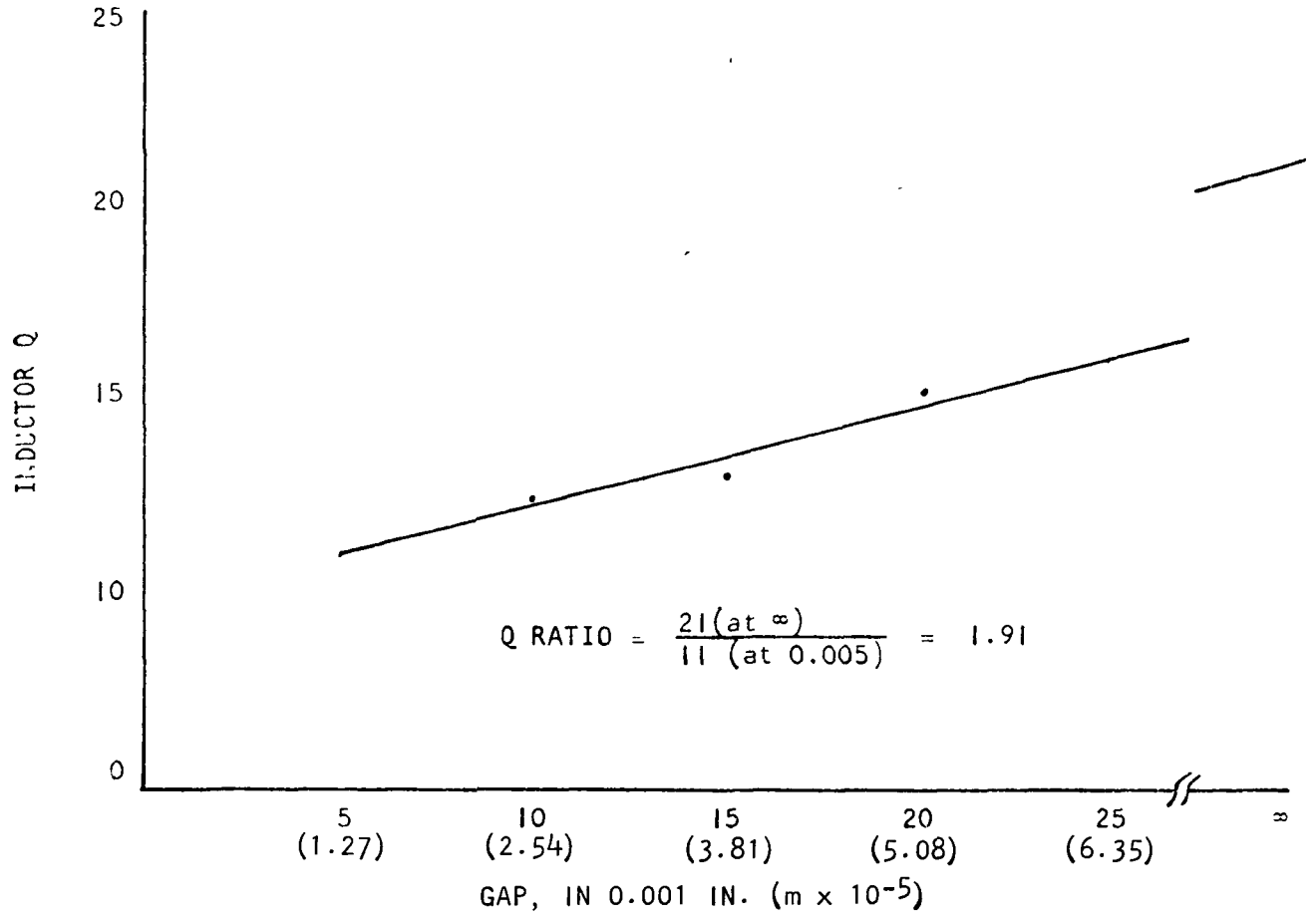


Figure 4-13. Inductor Q vs Gap Length

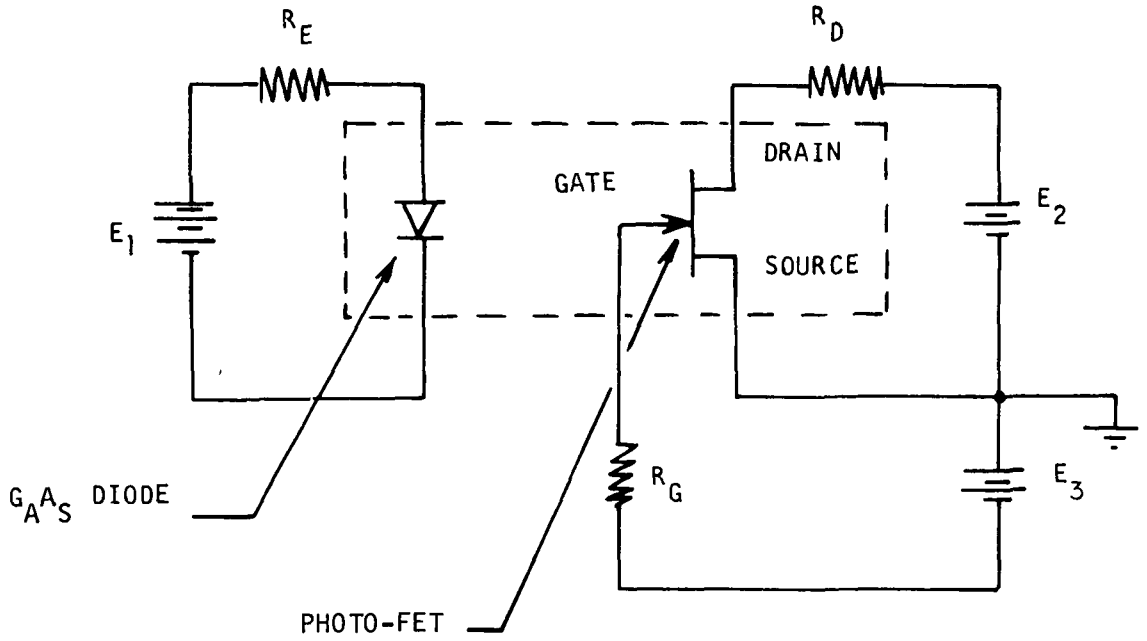


Figure 4-14. Test Circuit Photo Electronic Sensor

The system is operated as a position sensor by inserting a shutter disc between the lenses of the GaAs diode and the photofet. The disc has openings that make or break the light beam, thus resulting in a modulated drain current. As indicated earlier, the shutter disc is attached to the motor shaft and hence provides the necessary shaft position information. The drain current is then used to drive the power amplifiers, which provide motor winding excitation.

Of primary importance is the ability of the GaAs diode and/or the photofet to withstand thermal shock stress when immersed in liquid hydrogen from room ambient (or higher) temperatures. Of particular concern was the glass-to-metal seal associated with the lens of each device. To evaluate this potential problem, five sets of devices were obtained, and photo enlargements of their lens areas were made. In addition, the hermetic seal of each device was tested on a fine-leak tester. The intended test method was to immerse the photo sensor sets in liquid nitrogen until stabilized and then return them to room ambient until stabilized. This procedure was to be repeated five times and then the photo enlargements and leak tests repeated. However, the electrical test results were so gratifying that extended electrical testing was done prior to completion of the thermal testing.

Tests were conducted on four sets of photo sensors to determine their transfer characteristics, that is, the relationship between a change of current through the GaAs diode and the resultant change in the drain (load) current of the fet. To accomplish the static electrical tests, the GaAs diode and fet were mounted in an aluminum test fixture. The distance between their lenses was set at 0.1 in. This distance, which is not a critical factor was selected as a realistic spacing possible in the motor housing. Using the test circuit shown in fig. 4-14, transfer curves were made for each of the photo sensor sets at 168°F (85°C), room ambient, and -320°F (-198°C). The results are shown in fig. 4-15. The transfer curve shown is typical of each of the four sensor sets tested. It can be readily seen that the gain and linearity of the photo system significantly increased as the temperature decreased. The linear gain of the system was 3.3 at 185°F (85°C) and 16 at -325°F (-198°C). Also, the switching (on-to-off) system gain was from 0.85 at 185°F (85°C) to 6.6 at -325°F (-198°C). This results in an increase in system gain of 4.85 and 7.77, respectively. The switching gain is defined as the maximum drain current divided by the corresponding emitter current.

Tests were conducted to determine the exact gate bias voltage E3, called fet pinchoff voltage, that would result in current cutoff of each of the four fet's. The tests were run at 257°F (125°C), 185°F (85°C), 77°F (25°C), -85°F(-65°C) and -325°F (-198°C), and the results are shown in fig. 4-16. Of the four fet's tested, the characteristics of one device only differed from the others. In all units, the bias level was within the specified maximum of 5.0 V at 25°C. Therefore, if each photo system must have the same switching gain, special provisions would be required to bias each device separately. Fortunately, this condition is not required for proper operation as a position sensor. As long as sufficient emitter current can be conducted through the GaAs diode, enough energy can be radiated to cause any reasonable fet to switch.

Dynamic electrical tests were conducted to check the photo sensors in liquid nitrogen in conjunction with a rotating shutter disc. The disc was rotated at 3600 rpm with an induction motor. Fig. 4-17 shows the observed waveforms of the sensor at room ambient, and fig. 4-18 shows the liquid nitrogen temperature waveforms. The duty cycle of the output waveform is wider when immersed in liquid nitrogen because the increased gain in liquid resulted in a response to scattered light leakage in the relatively crude experimental set-up.

As mentioned earlier, a prime area of concern for this system is the ability of the devices to withstand the thermal shock associated with immersion in the cryogenic liquid.

A test program that thermally cycled the devices from room ambient to -325°F (-198°C)(liquid nitrogen) was conducted. After 26 cycles (elapsed time of 13 hr), one fet indicated an open circuit between the drain and the source leads. A second fet could not be biased off after 160 temperature cycles. The two failed devices were subjected to a failure analysis to determine the exact cause of failure (see Appendix C). Surprisingly, the failures were traced not to a fundamental problem in materials, as was originally suspected, but rather to poor process controls which would result in low reliability under any conditions.

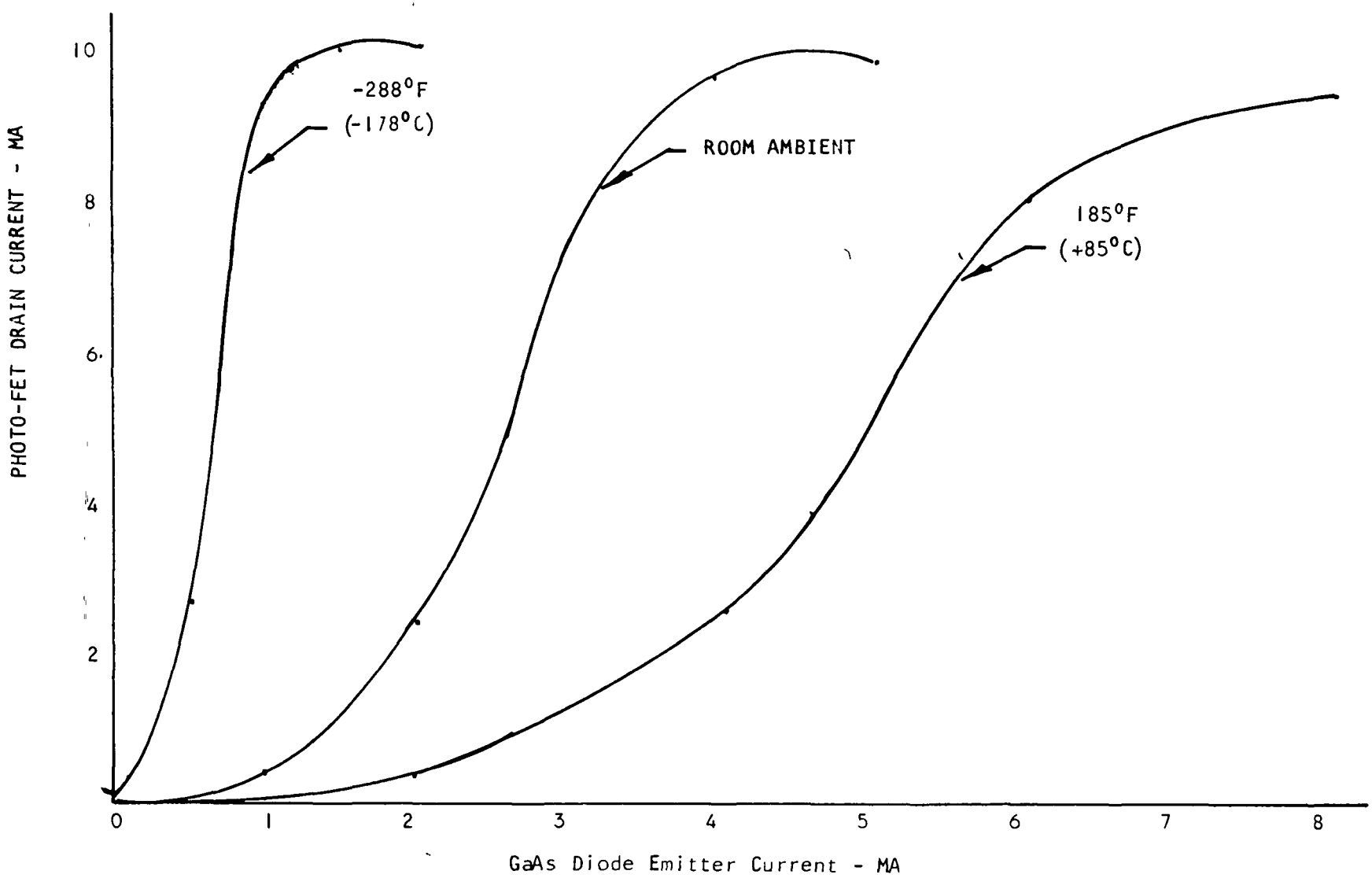


Figure 4-15. Photo Sensor Static Transfer Curve

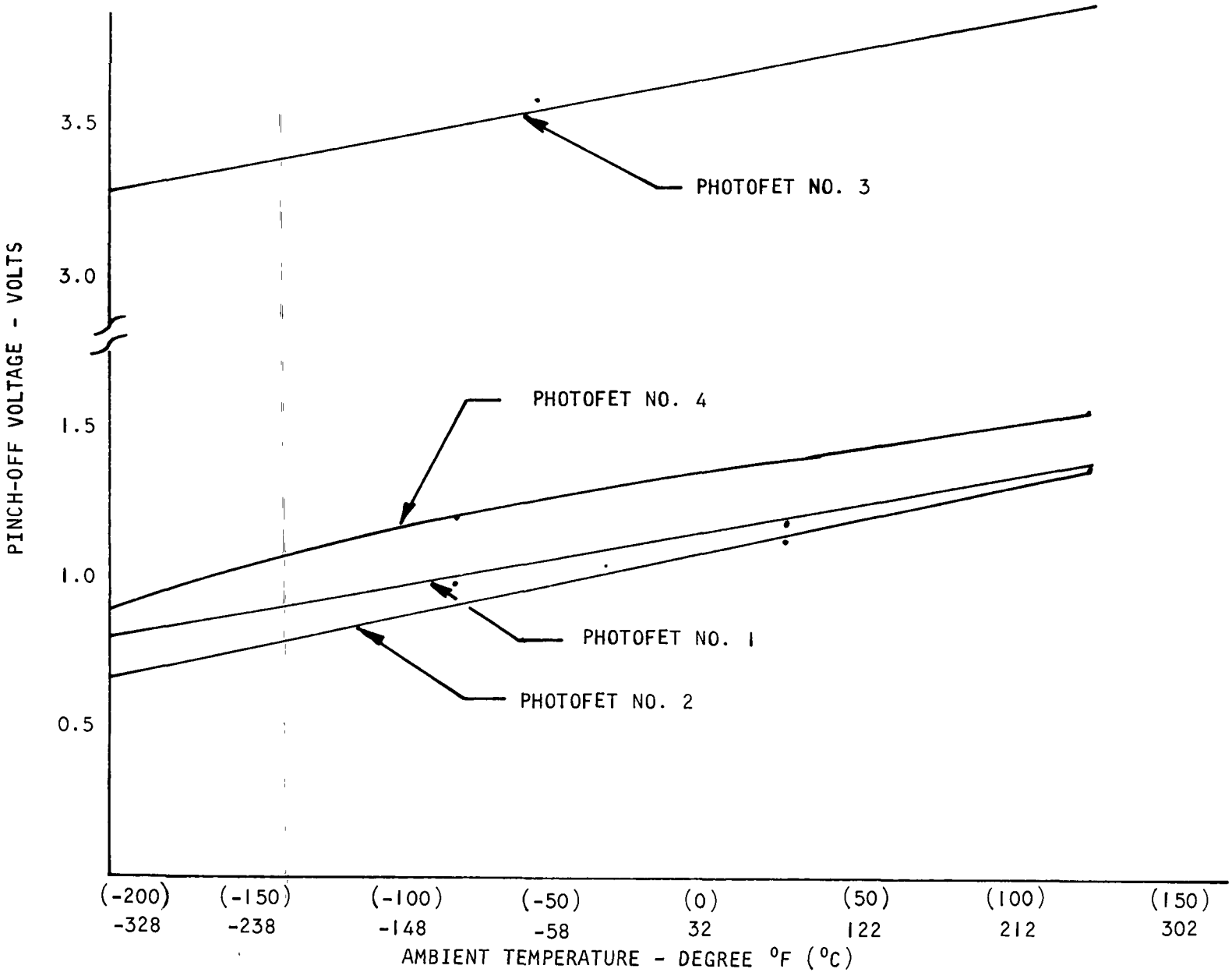


Figure 4-16. Pinch-off Voltage Versus Ambient Temperature for Fixed Drain Current

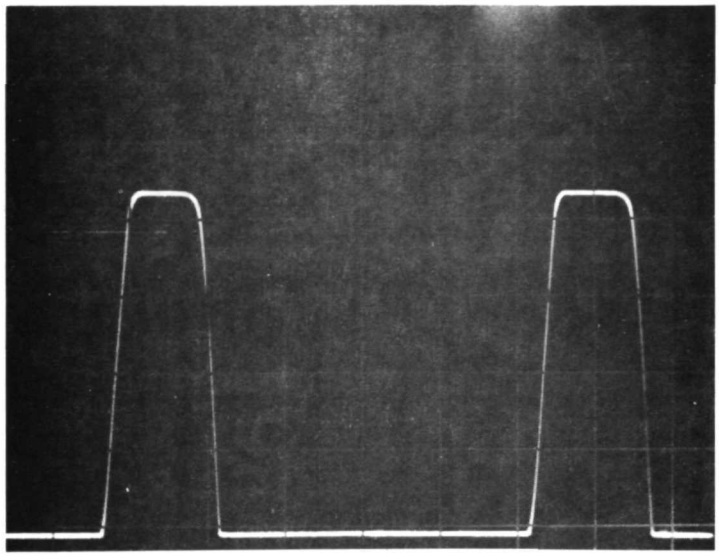


Figure 4-17. Opto-electrical Position Sensor Output Voltage at Room Ambient Vertical 2V/CM Horizontal IMS/CM

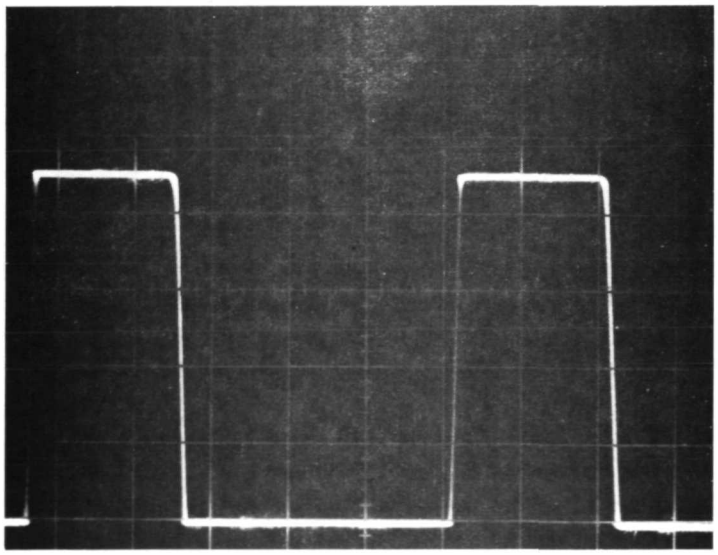


Figure 4-18. Opto-electrical Position Sensor Output Voltage at -198°C Vertical 2V/CM Horizontal IMS/CM

F-16236

This, of course, opened the possibility of introducing improved process controls and screening techniques, and possibly, the development of an alternate source of supply. The effort required to do this was outside the scope of the present program, and since the failure rate of two of six devices was obviously not acceptable, this approach was abandoned.

The variable reluctance position sensor consisted of two separate transformer windings. Each winding was wound on one half of a transformer U type core. The two halves of the sensor were separated by a gap through which the shutter passed. The primary half was excited by a 100 kHz voltage. If no metal was within the gap area, magnetic flux was coupled from the primary to the secondary core, and voltage was present at the output. When a metal passed within the area of the gap, the flux was decoupled from the secondary core by eddy current shielding, and output voltage was substantially reduced. Fig. 4-19 depicts the construction of a sensor, and fig. 4-20 shows schematically the operation of one position sensor channel.

The core losses are a function of the core size, core material, tape thickness, and the frequency of the exciting voltage. The sensors were fabricated from (1) mil Silectron tape; they dissipated approximately 30 mW each and showed no measurable change from room temperature to -320°F (-198°C). Use of 1/2 mil tape to reduce dissipation was investigated. The thinner tape had a lower watts-per-pound loss factor, but it also had a lower stacking factor which resulted in higher flux densities and increased losses. The overall sensor tank dissipation could be reduced by using only two position sensors with external gating circuitry to provide switching logic. However, as previously stated, if one sensor failed, the motor would stop. With a four-sensor system, if one sensor failed when the motor is running, the motor would continue to run, and it would still have a 75-percent chance of restarting.

The variable reluctance position sensor required a 100 kHz sine wave oscillator circuit to provide excitation for the sensors. The oscillator was also used to provide the required positive and negative low-voltage biases needed for the power amplifiers that drive the motor windings. The 100 kHz power was transmitted to and from the motor by shielded twisted pair conductors. Coaxial cable was not required.

The variable reluctance position sensors were first characterized at room ambient under the following conditions.

(a) Primary winding: 200T; No. 40 wire, resistance 14 ±3 ohms.

(b) Secondary winding: 650T, No. 44 wire, resistance 100 ±20 ohms.

(c) Core: Carstedt CMI-A

(d) Excitation. 8.5-V rms; 19-ma rms; 100 kHz; voltage and current phase angle = 80 degree

(e) Load. Rectified into a resistor filtered with a capacitor. An impedance matching transformer was not used.

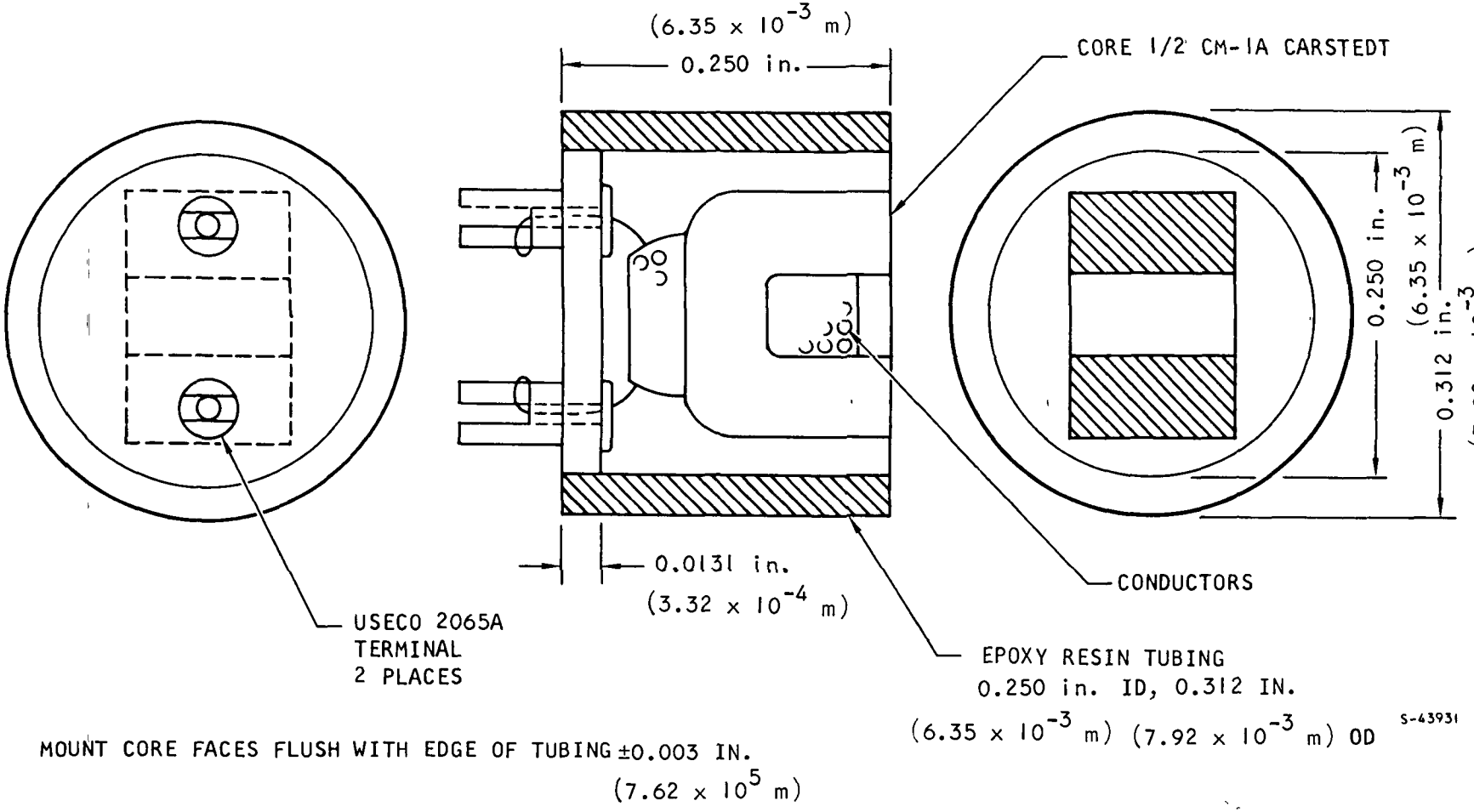


Figure 4-19 Assembly of Variable Reluctance Sensor

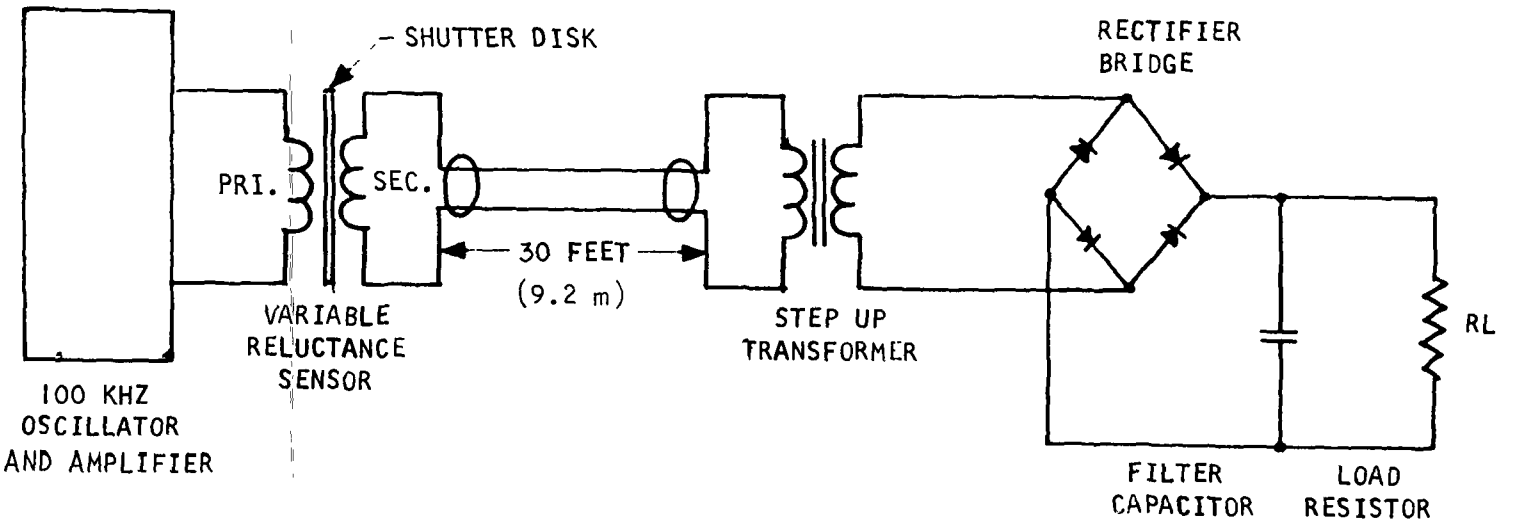


Figure 4-20 Single Channel of Variable Reluctance Position Sensor

Fig. 4-21 shows the output voltage vs core-to-core gap at a fixed load of 56 kΩ shunted by a 100 pf capacitor. Fig. 4-22 shows output voltage and power vs load resistance for a fixed gap. Fig. 4-23 shows output voltage vs load current also for a fixed gap, for the purpose of determining the output impedance of the sensors. Since the characteristic impedance of a twisted-shielded pair of conductors is in the order of 30 ohms, the 83 kΩ output impedance of the initial sensor was obviously too high for transmission via a 30 foot cable. Consequently, the secondary turns where reduced to 46, having an impedance of 41 ohms and a step-up impedance matching transformer was installed at the electronics.

Testing in LN_2 showed that the predominant in-tank power losses do not vary greatly with temperature, the following test data taken at room temperature is indicative of in-tank conditions:

(a) Excitation voltage 8.5-V rms, 100 kHz

(b) Excitation current 19-ma rms

(c) Voltage to current phase angle: 80 degrees, approximately.

Power = EI COS (ϕ)

= 8.5-V x 19-ma x COS (80^{o})

= 28 mW per sensor, typical

The above data is for a 0.001 in. (2.54×10^{-4}m) thick tape core grain oriented silicon steel. Copper losses are neglected. The position sensor coils were temperature cycled in a manner similar to tests described for the optical sensors. One failure occurred early in the tests, and was traced to a fabrication defect. It was concluded that, with a minimum of screening, these sensors are suitable for cryogenic operation.

The variable reluctance position sensors were tested dynamically for proper operation. A test rig was fabricated to support the sensors and shutter in liquid nitrogen. The shutter was driven by the motor, located outside the liquid. The sensor output was rectified and filtered to provide the proper voltages for the current switches. The first test shutter, fabricated from an aluminum disc, had four blades 45 degrees wide and equally spaced to provide a 50-percent duty cycle. A photograph of the output signal at normal operating speed is shown in fig. 4-24 and in fig 4-25. It can be seen that, for all practical purposes, operation in LN_2 is identical to operation at room temperatures. The multiple traces seen on the LN_2 photograph are due to problems with the test fixture. The waveforms are not as well defined as those obtained from the optical sensor. As discussed later, this requires more complex circuitry in order to effect sufficiently accurate commutation of the motor. In order to reduce drag, the segmented aluminum shutter disc was replaced by one eteched from copper clad epoxy. The normal 4-oz copper had to be built-up by plating additional copper in order to obtain sufficient metal thickness at the 100 kHz frequency. The shutter is .031 in. (7.9×10^{-4}m) epoxy board with .012 in. (3.1×10^{-4}m) copper plate and a 1.0 in. (2.54×10^{-2}m) O.D. Test data for this shutter is shown in fig. 4-26 and fig. 4-27. In comparing the copper-clad epoxy shutter with the aluminum, it is apparent that the copper-clad epoxy shutter provided a more sharply turned, higher-gain signal than aluminum. Both had the

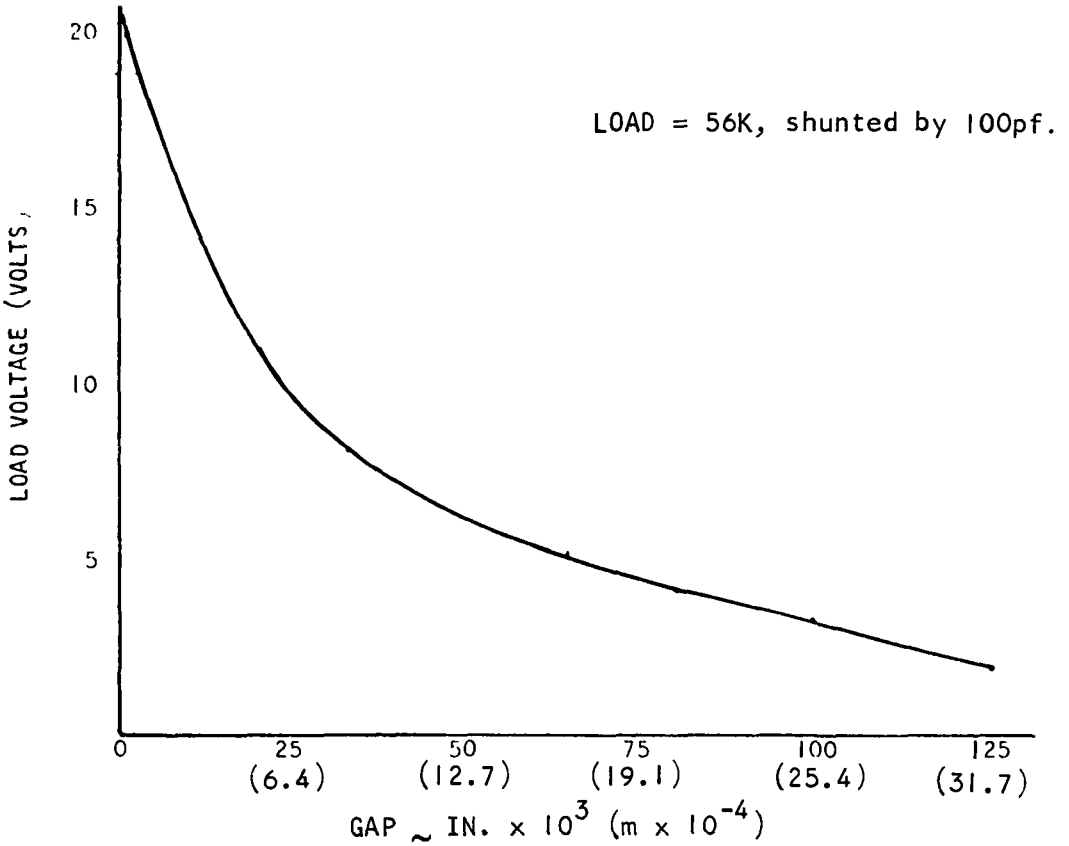


Figure 4-21. Variable Reluctance Output Volutage vs. Gap

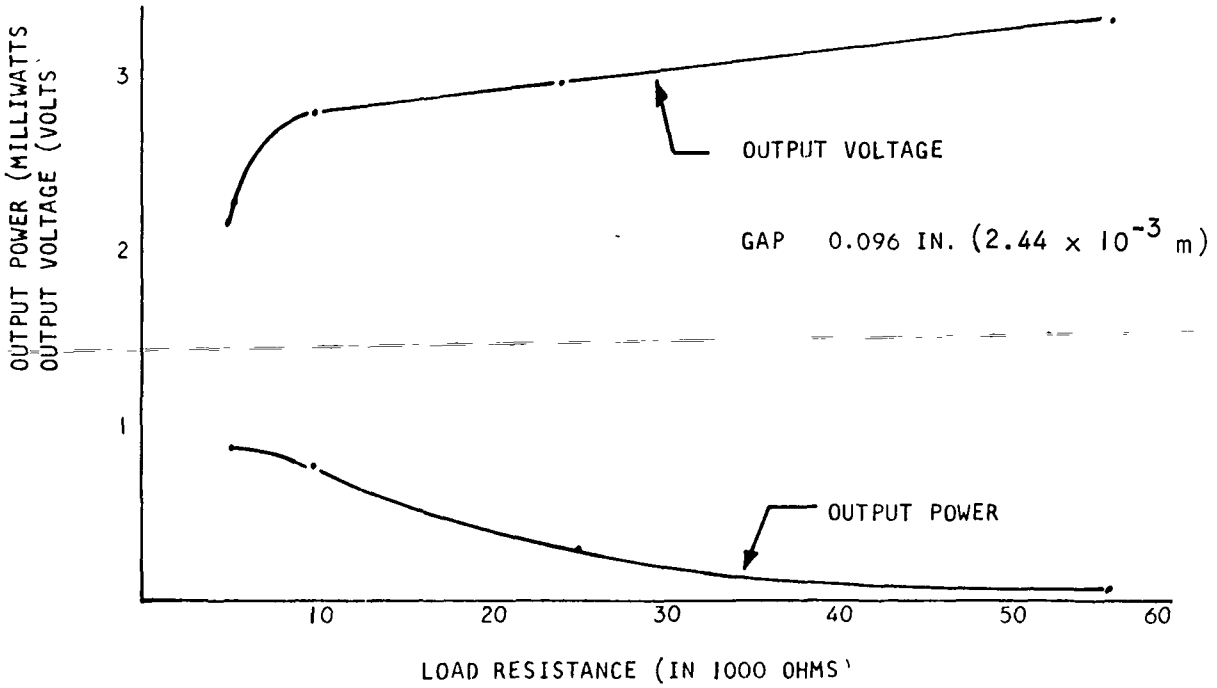


Figure 4-22. Reluctance Position Sensor Output Voltage and Power vs Load Resistance

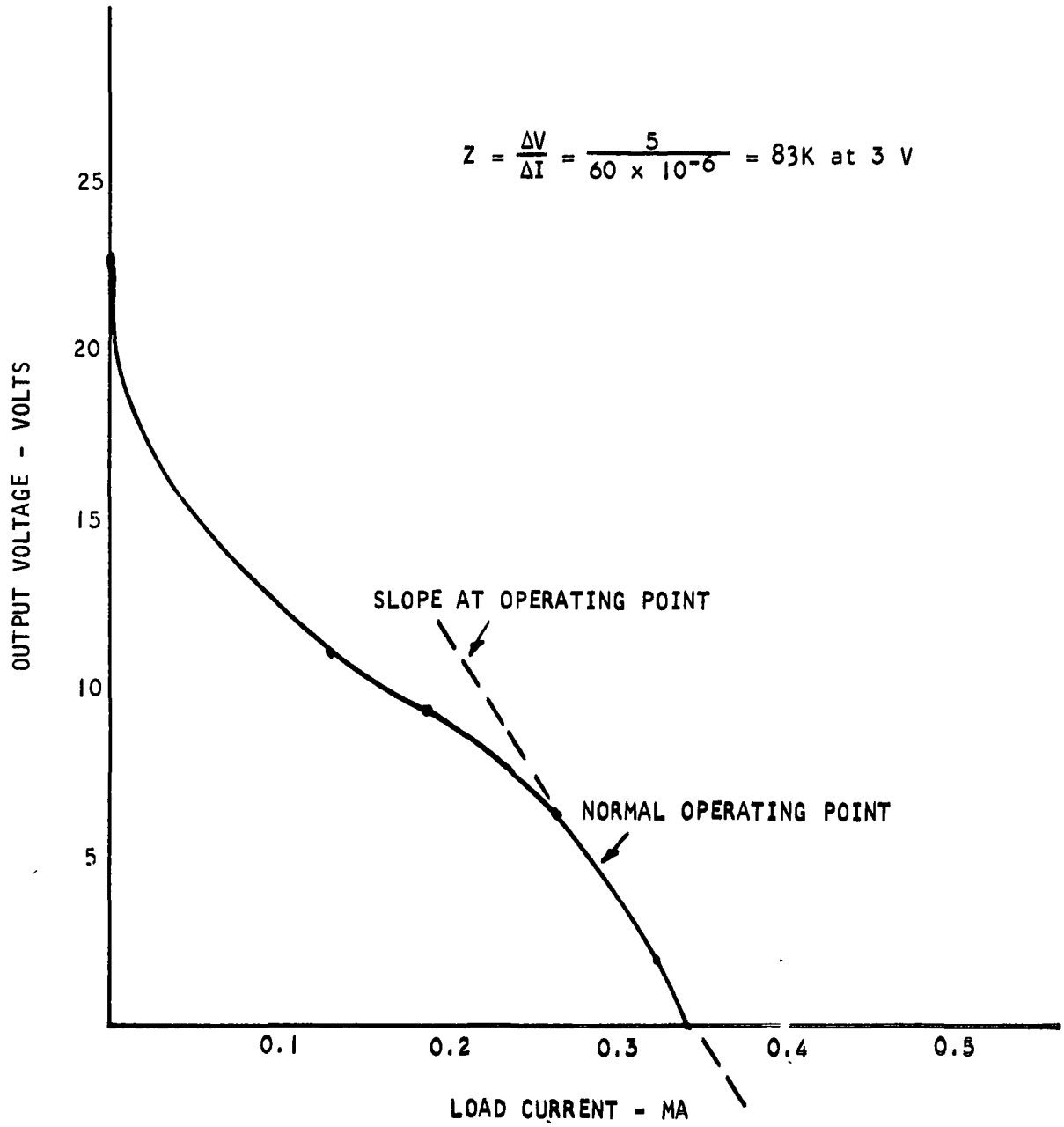


Figure 4-23 Sensor Load Characteristics

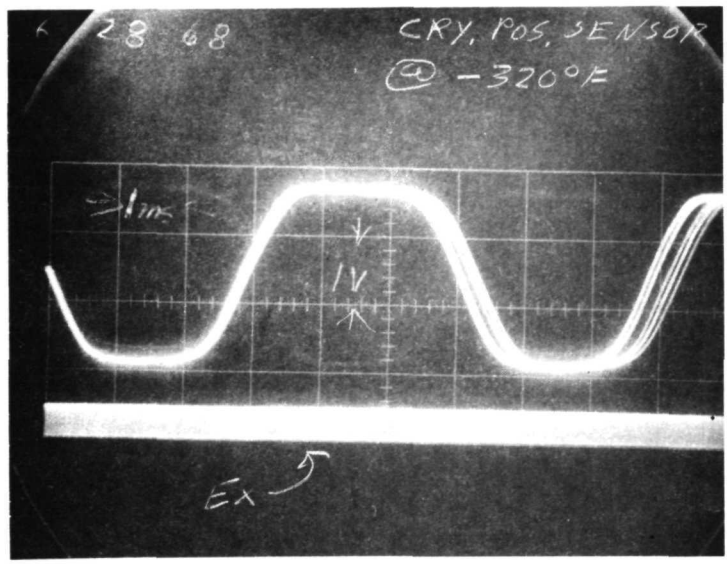


Figure 4-24. Variable Reluctance Position Sensor Output Voltage in Liquid Nitrogen, Aluminum Shutter

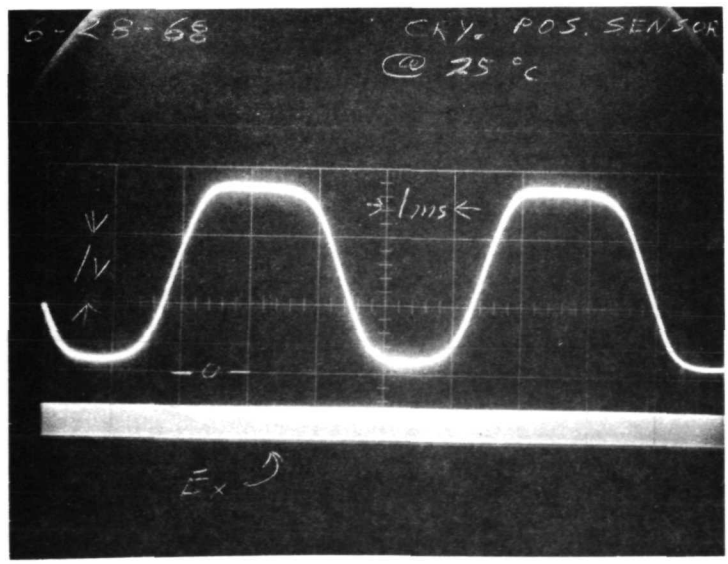


Figure 4-25. Variable Reluctance Position Sensor Output Voltage at Room Temperature, Aluminum Shutter

F-16235

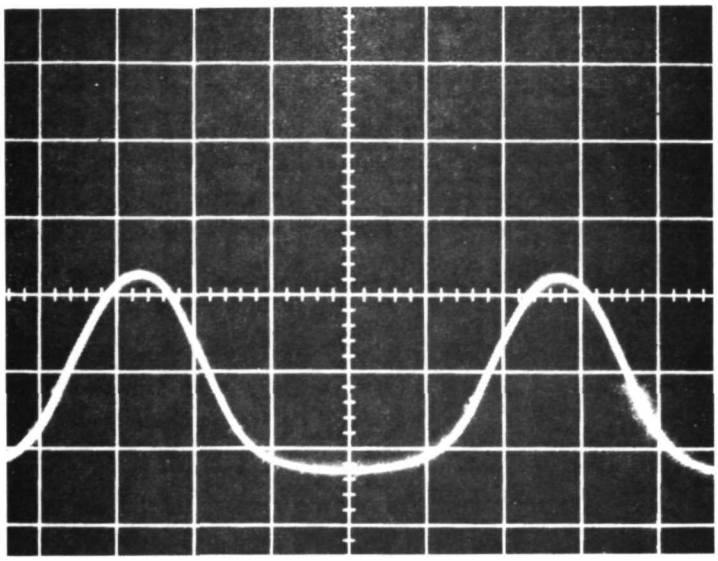


Figure 4-26. Variable Reluctance Position Sensor Output Voltage at Room Ambient Vertical 2V/CM Horizontal IMS/CM, Etched Copper Clad Epoxy Shutter

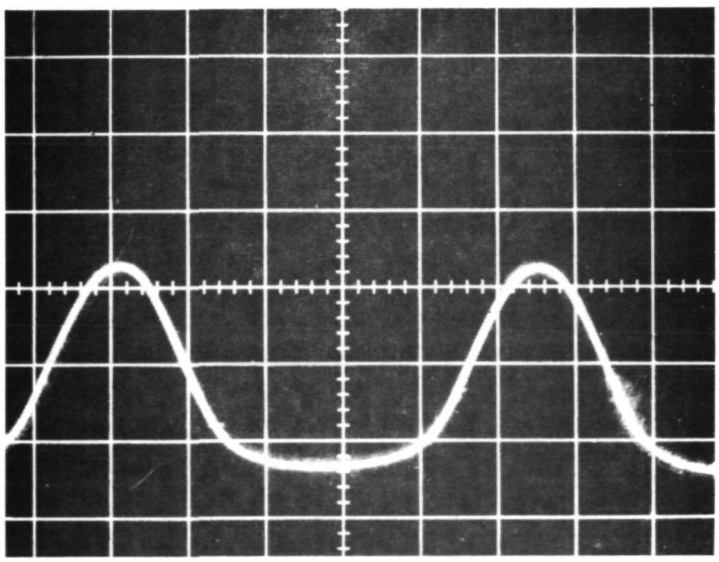


Figure 4-27. Variable Reluctance Position Sensor Output Voltage at -198°C Vertical 2V/CM Horizontal IMS/CM, Etched Copper Clad Epoxy Shutter

F-16234

same plan form geometry and rotational speed; thus, they had the same input duty cycle, but a very different output duty cycles.

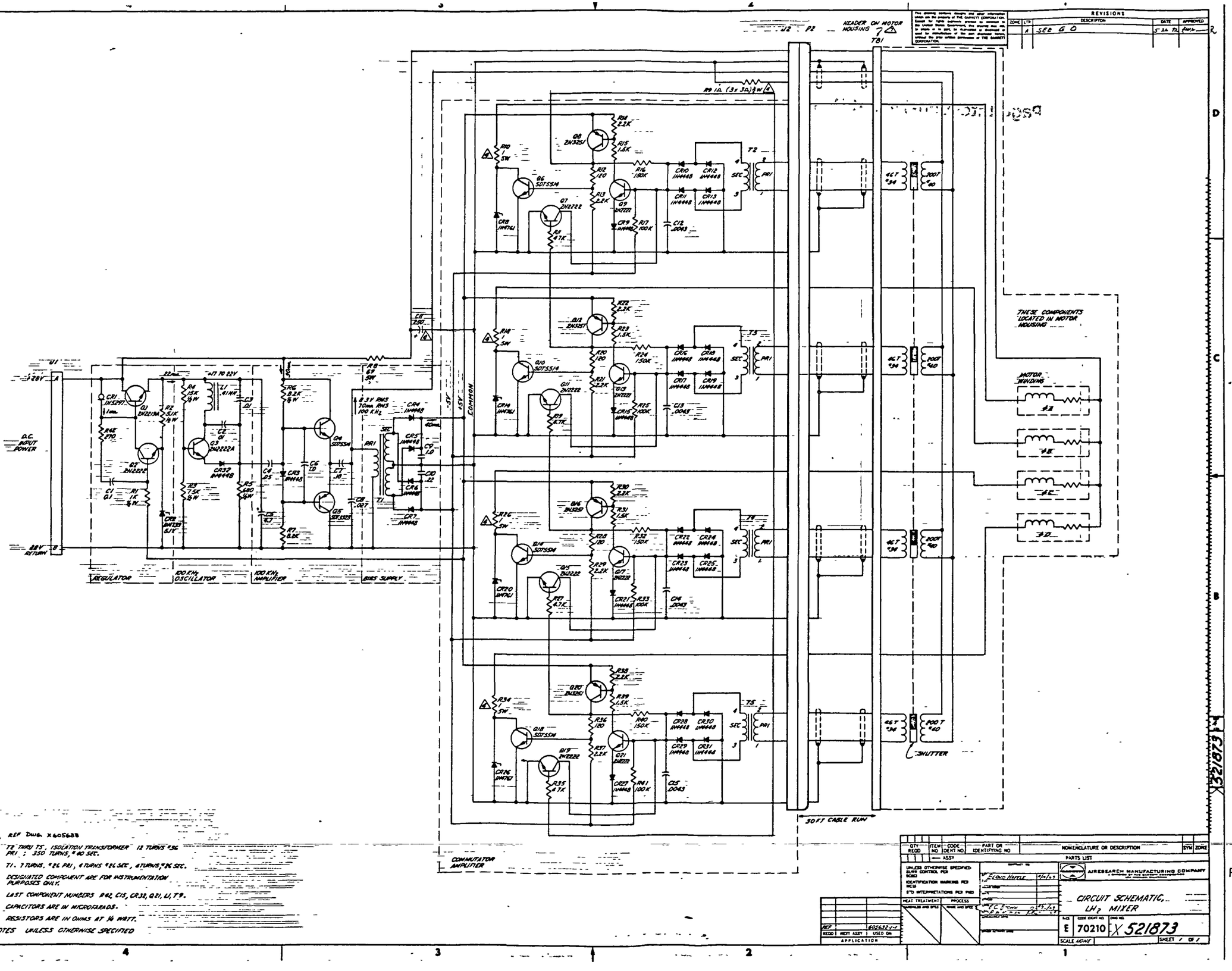
Due to the successful development tests, the variable reluctance position sensor was scheduled to use in the motor. Inspite of its higher losses, and the requirement for more complex electronics, it offered a direct and reliable solution which could be physically fit in the compressor outline, and which was compatible with the program schedule.

Circuit diagram.--Referring to the schematic diagram, fig. 4-28, it can be seen that the electronics consists of four identical motor drive channels and of a power supply. Transistor Q1 is the pass element of a series regulator. Its base is driven by field effect diode CR1 which provides a constant current. Excess current is by-passed by error amplifier Q2. Transistor Q3 is the active element of a colpitts type oscillator, the output of which is amplified by the complementary pair Q4 and Q5. The amplified 100kHz signal is fed directly to the primaries of the motor position sensors. It is also stepped down in transformer T1 and rectified to supply amplifier channel operating biases. The dc output of the rectifier is fed back to the regulator and compared to reference diode CR2 to close the loop on the power supply.

Current in phase A of the motor is switched by Q6. Transistor Q6 is driven by Schmitt trigger Q8 and Q9 in response to the rectified output signal of the position sensor. Resistor R16 provides the positive feedback needed for trigger action, and diode CR9 provides for additional threshold bias. This trigger scheme is used to overcome the problem presented by the sloppy rise-time of the position sensor output. Transistor Q7 turns channel A off as soon as channel B is switched on, thus always guaranteeing a minimum overlap independent of aperture trailing edge accuracy.

Several parts shown on the schematic are not required for circuit operation and have been included only for purposes of instrumentation. These parts are appropriately noted. Resistor R8 shapes the torque-speed characteristic so as to intercept the two required operating points of the machine. Zener diodes CR8, CR14, CR20, and CR26 are used to clip the commutation spikes. These zeners are probably not needed in this application because of the low energies involved. They have been included, however, because the second breakdown characteristics of the switching transistors were not formally defined in the cut-off region.

Development testing.--Due to the practical difficulties associated with the handling of liquid hydrogen, development tests were conducted in liquid nitrogen and in liquid helium, thereby bracketting the liquid hydrogen conditions. The motor was placed in the inner dewar vessel of the test setup shown in figs. 4-29, 4-30. 4-31, and 4-32. The dewar vessel was evacuated to 29 in. Hg, gage vacuum, (9.7×10^{-6} N/M^2), and held for one hour to dry the motor. Boil-off N_2 gas was then admitted to the inner dewar vessel to bring the internal pressure to approximately atmospheric or slightly higher. The inner dewar vessel and outer dewar vessel were vented to atmosphere and allowed to fill with LN_2 until the motor was completed submerged. The motor was loaded with an uncalibrated eddy current brake and electrical data was taken at several operating points. At the conclusion of the LN_2 tests the inner dewar vessel was pressurized with GN_2 and the LN_2 expelled as completely as possible. The inner dewar vessel was then



1. REF DWG. X605638
2. T2 THRU T5, ISOLATION TRANSFORMER 12 TURNS #36 PRI ; 350 TURNS, #40 SEC.
3. T1. 7 TURNS, #26 PRI, 6 TURNS #26 SEC., 8 TURNS, #26 SEC.
4. DESIGNATED COMPONENT ARE FOR INSTRUMENTATION PURPOSES ONLY.
5. LAST COMPONENT NUMBERS R42, C15, CR32, Q21, L1, T9.
6. CAPACITORS ARE IN MICROFARADS.
7. RESISTORS ARE IN OHMS AT ½ WATT.

NOTES UNLESS OTHERWISE SPECIFIED

REVISIONS

ZONE	LTR	DESCRIPTION	DATE	APPROVED
	A	SEE G.O.	5-24-72	

This drawing contains designs and other information which are the property of THE GARRETT CORPORATION. Except for rights expressly granted to customers of the Limited Access Department, this drawing may not be shown to or used by customers or disclosed to others for manufacturing purposes or used for any purpose without the prior written permission of THE GARRETT CORPORATION.

QTY REQD	ITEM NO.	CODE IDENT NO.	PART OR IDENTIFYING NO.	NOMENCLATURE OR DESCRIPTION	SYM ZONE
			ASSY	PARTS LIST	

UNLESS OTHERWISE SPECIFIED
BIAS CONTROL PCB
IDENTIFICATION MARKING PER MC10
ETD INTERPRETATIONS PER P185
HEAT TREATMENT
PROCESS

F. Lloyd Hartle 4/5/72
4/5/72

AIRESEARCH MANUFACTURING COMPANY

CIRCUIT SCHEMATIC, LH_2 MIXER

SIZE E | CODE IDENT NO. 70210 | DWG NO. X 521873

SCALE NONE | SHEET 1 OF 1

REF REQD | NEXT ASSY | USED ON APPLICATION | 605692-1-4

X521873

Figure 4-28. Mixer Electronics

Page Intentionally Left Blank

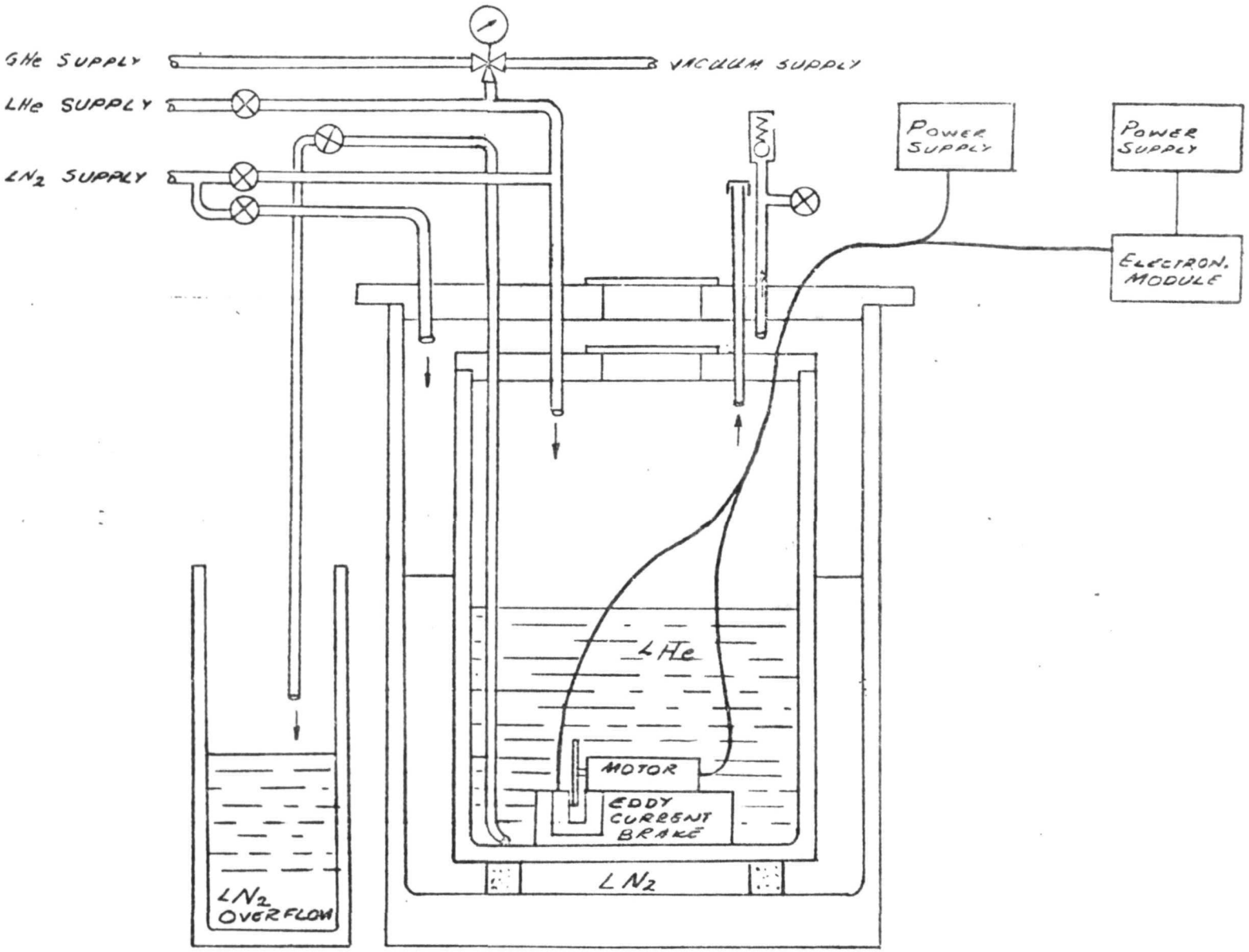


Figure 4-29 Motor Test Setup

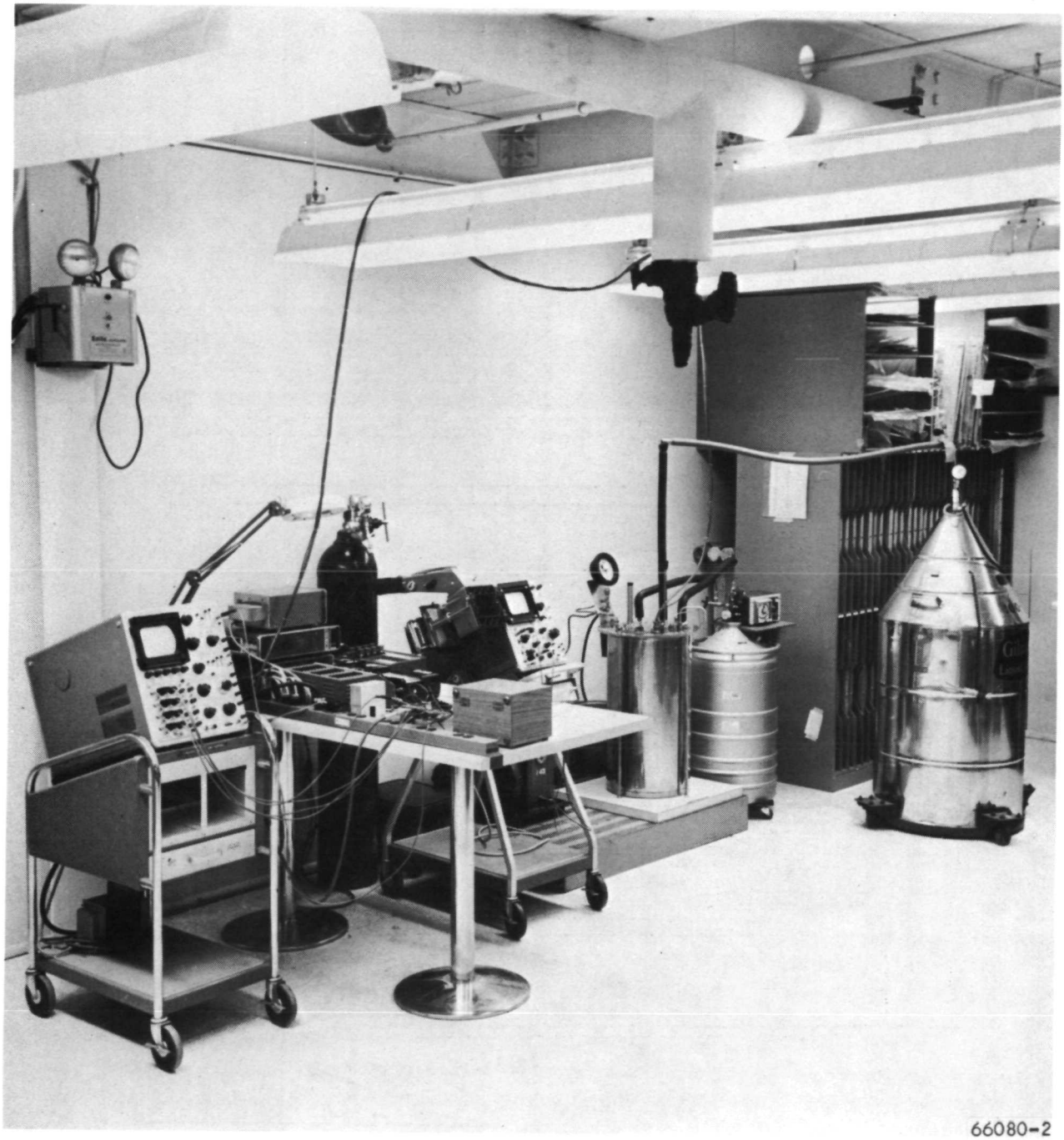


Figure 4-30. Liquid Nitrogen and Liquid Helium Test Setup, Overall View

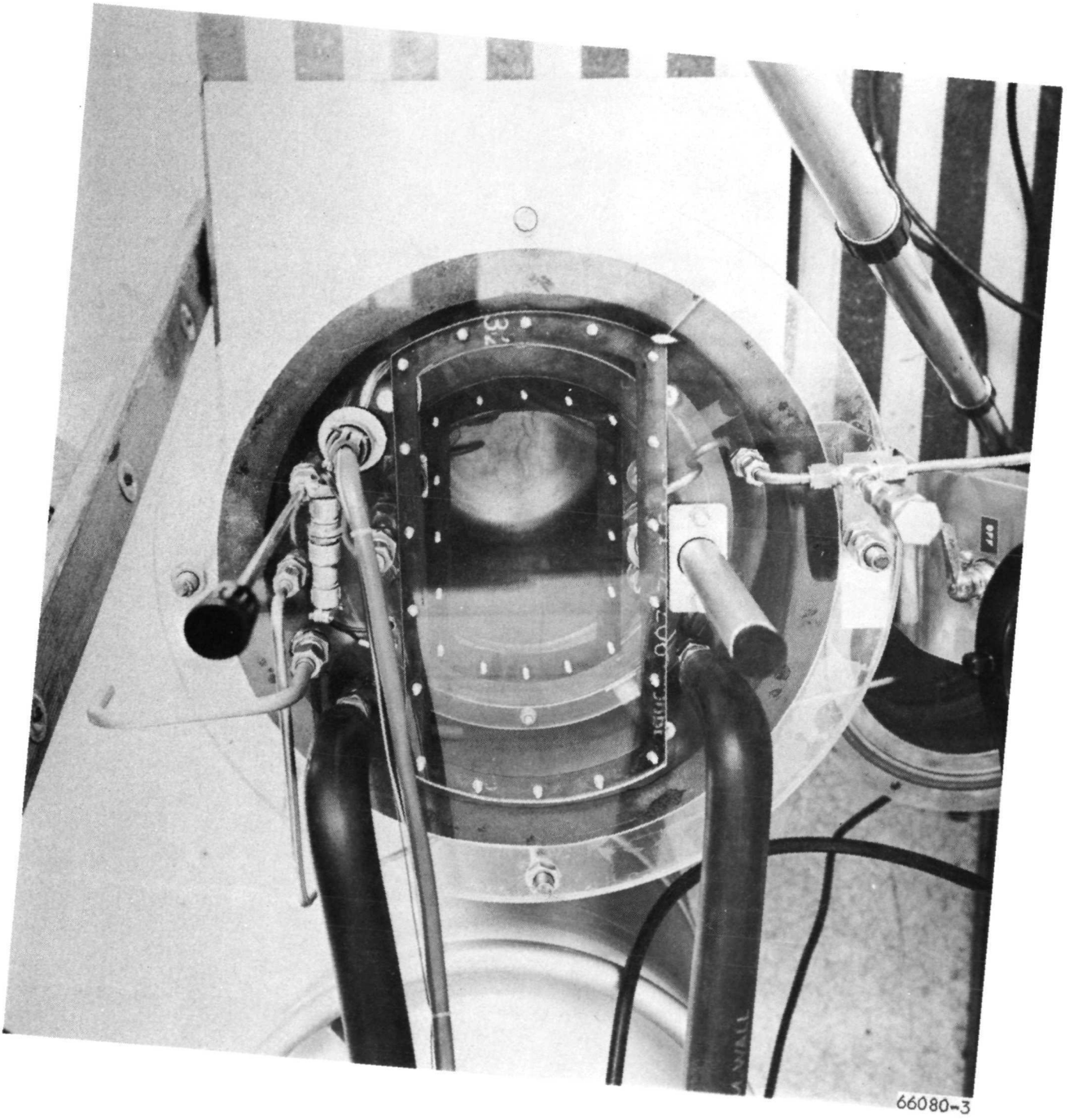


Figure 4-31. Guarded Dewar Used for Liquid Helium Testing

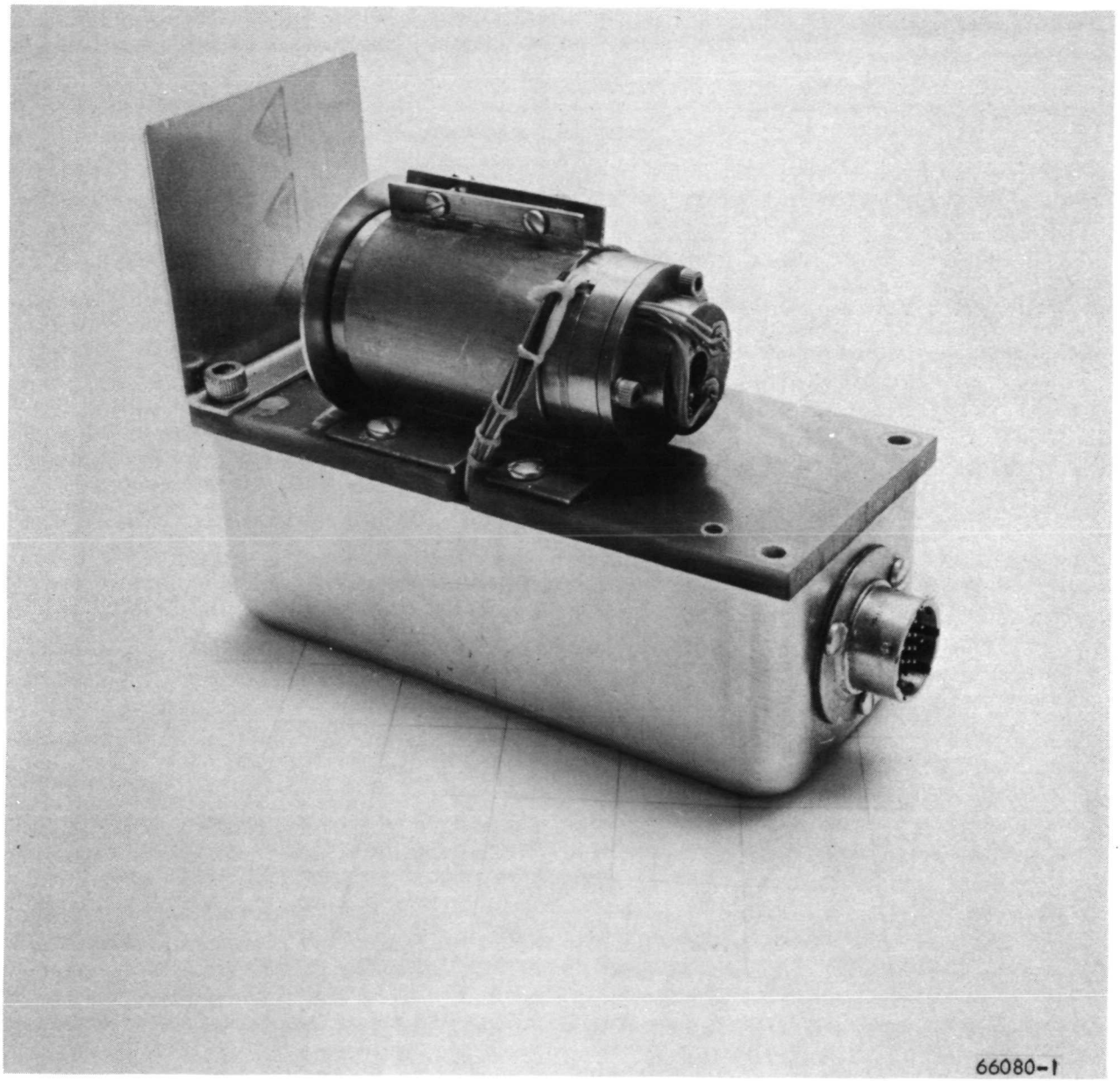


Figure 4-32. Liquid Hydrogen Mixer Motor Mounted on Eddy Current Brake

evacuated to approximately 29 in. Hg, (9.7×10^{-6} N/M^2) gage vacuum, to remove the LN_2 remaining within the motor. At a pressure of 29 in. Hg, gage vacuum, nitrogen freezes, so the motor was checked for rotation briefly, to assure no blockage of the bearings due to frozen nitrogen. Boil-off helium was then admitted to the dewar vessel, bringing the pressure of the inner dewar vessel to approximately one atmosphere. With the inner dewar vessel vented to atmosphere, filling with LHe continued until the motor was completely submerged. The motor was again operated with the eddy current brake to obtain performance data in liquid helium.

The significant results of the above tests are summarized in fig. 4-33 for liquid nitrogen and in fig. 4-34 for liquid helium. These speed-power curves show three lines. The highest power line represents the input power to the electronics or total power input. The middle line is the input power to the motor itself, and the lower line represents the electromagnetic power available in the motor. The first two lines represent measured data, excluding the power supply in the first case and the 112 mW of sensor power in the second case. The electromagnetic power was calculated as follows:

$$PWR_E = \frac{\text{Torque} \times \text{Speed}}{1352}$$

where torque is in in.-oz and speed in rpm. The torque was calculated for each operating point using the torque constant of the motor and the measured average motor current. The successful completion of these tests indicated that the motor and its associated electronics are fully capable of operation in the cryogenic fluid, and layed the ground work for final tests and calibration with the impeller attached.

In all cryogenic testing, it was necessary to pull a vacuum of 29.5 in. Hg (9.9×10^{-6} N/M^2) or greater to remove moisture before immersing in cryogenic fluid or the bearings would freeze. It was also found that leakage of nitrogen gas from the guard dewar into the liquid helium dewar produced "nitrogen ice" which would also block the bearings.

Fabrication

Fabrication of the mixer and motor was basically straightforward. The problem areas were the stator windings, position sensor coils, welding of the mounting base to the electrical connection header and physical handling of small screws in the position sensing-commutating section of the motor, see fig. 4-3.

The stator windings are of No. 39 magnet wire with the i.d. formed by a mandrel. It was necessary to be very careful in removing the mandrel to prevent wires from breaking. Several different mold release agents were tried with the most successful being Miller Stepphensen MS122 Flurocarbon. It is believed that use of a mandrel with removable conical ends might improve this procedure.

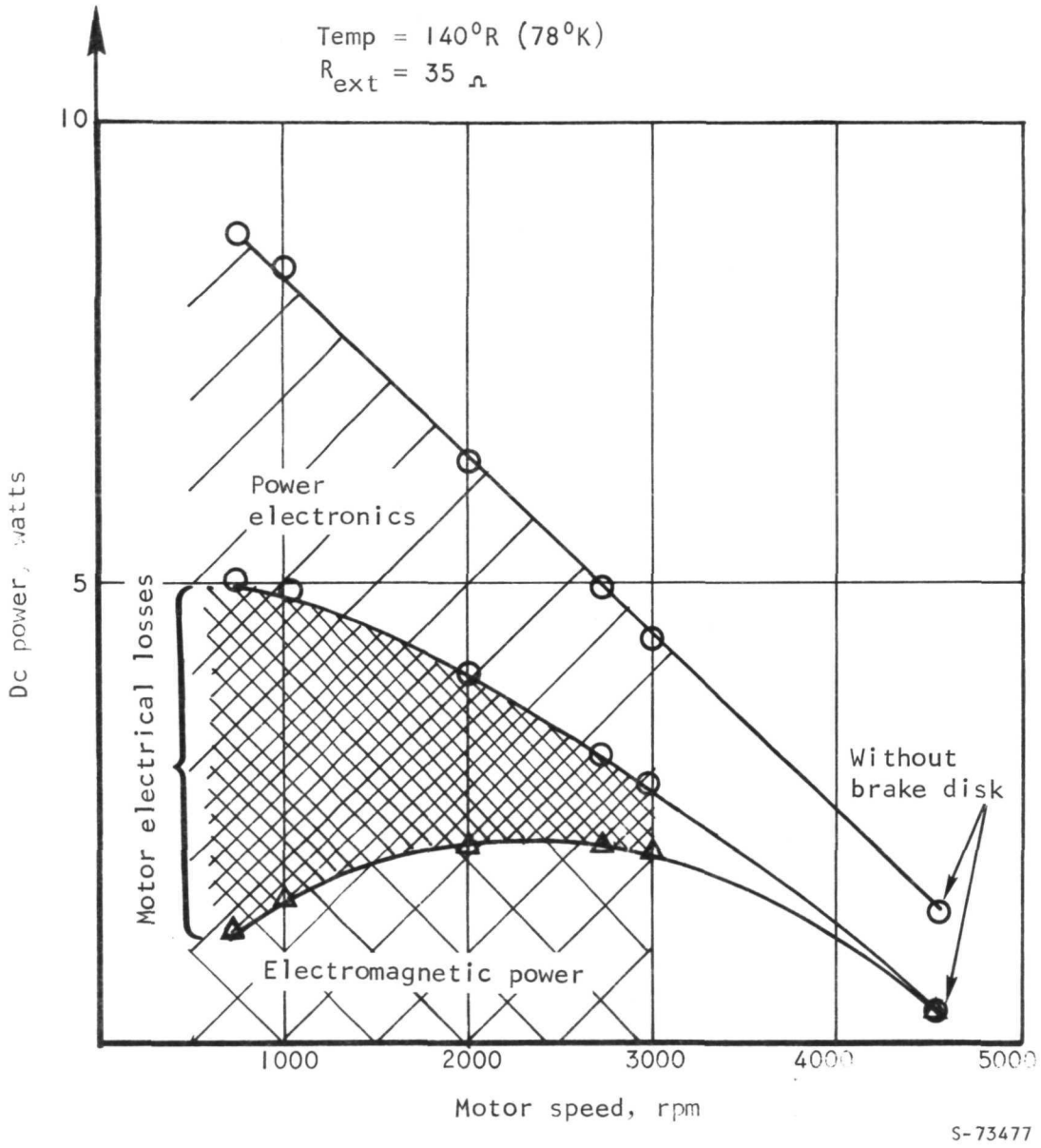


Figure 4-33. Motor Performance Test in Liquid Nitrogen

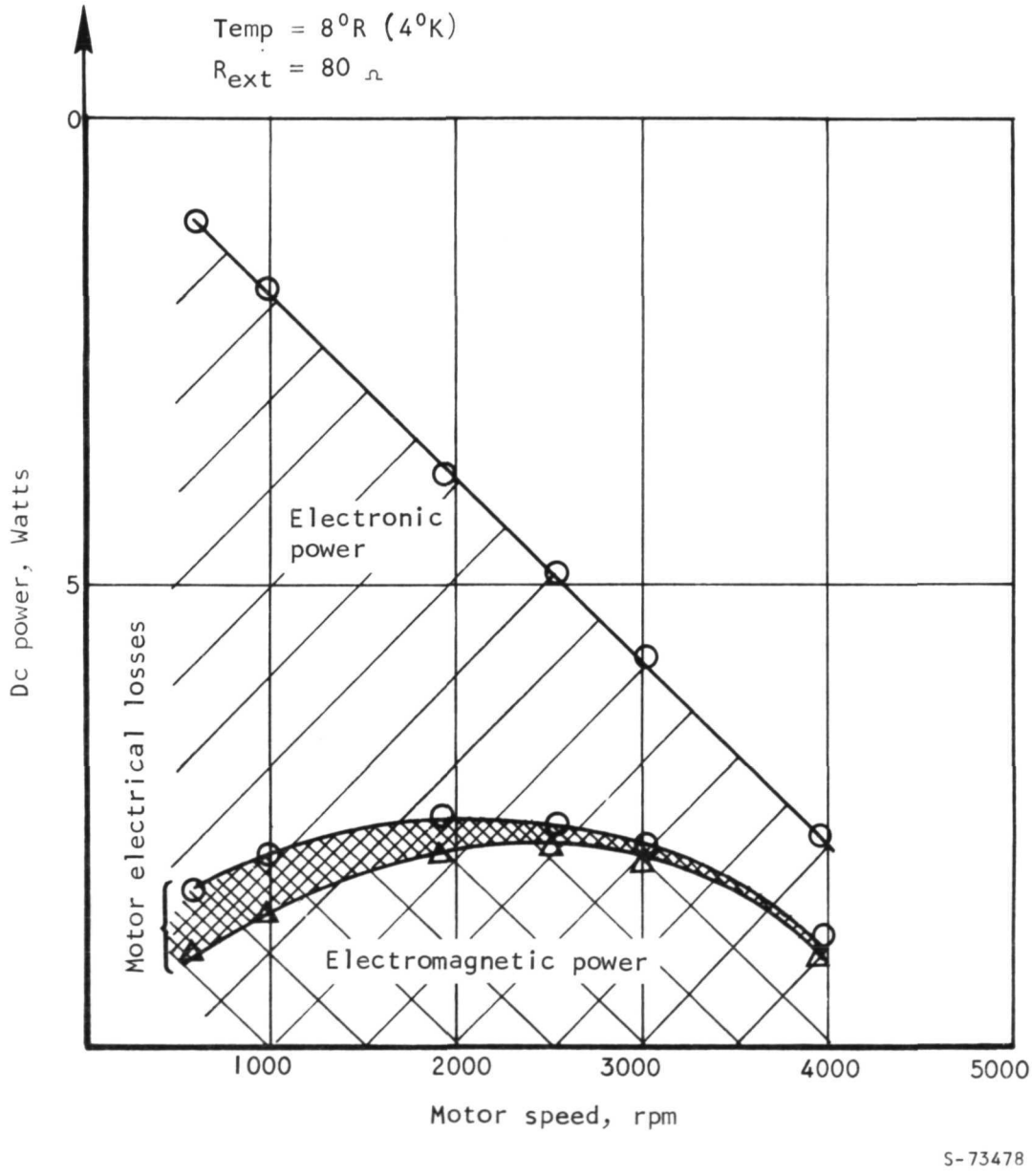


Figure 4-34. Motor Performance Test in Liquid Helium

The position sensing coils are made of No. 44 magnet wire on laminated cores. These coils were hand wound with great care. After the sensors were wound, they were potted and the "gap" end was ground flush. The problems were that the wire broke during winding and there was a tendency of the core lamination to cut through the wire insulating varnish, shorting the coils. In addition, when the surface of the potted sensor was ground to the proper dimension, there was a chance that a strand of wire might be cut through. In all, three sensors had to be started to finish with one useable device. It is believed that a special lamination stack deburring procedure and more sophisticated encapsulation tooling would considerably reduce the number of parts lost in fabrication.

The electrical connection header uses a manufacturer's standard fused glass insulator with conductor pins and a metal ring around the outside. This metal ring was electron beam welded to a stainless steel mounting plate. A total of five pieces was obtained and attempts made to weld the mounting plate. In each instance the glass cracked. One piece, having only a small crack was thermally shocked by dropping into a container of liquid nitrogen. The part was not further damaged, so it was used. It is believed that a special order part with the glass fused directly to the mounting plate could be made without difficulty. For such a header there would be special tooling and a long lead time would be involved.

The positioning sensors must be mounted to the shaft of a dc brushless motor. The most logical place was at the end of the shaft opposite the impeller. The location and overall dimensions reduced all sizes and resulted in some screws as small as No. 0 being used. Parts of this size are difficult to handle and care must be taken in torquing such screws. Within the constraints of the required performance of the machine, there appear to be few options regarding the size of fasterner to use.

There are a number of considerations involved in assuring that the stator assembly is properly fabricated. There are no iron teeth in the stator assembly to guarantee the winding position and flux linkage. A Teflon liner for the stator ID was initially tried to protect the stator windings from damage when removed from the assembly mandrel. This liner shrunk excessively during low-temperature operation, causing the rotor to drag. A loose-weave glass cloth liner replaced the Teflon and bonded well enough to eliminate the problem. Proper tooling must be fabricated and test procedures instituted to achieve consistently good production stators. The brushless dc motor stators which AiResearch makes in production are built using a fixture which simulates the locating feature of normal stator iron teeth. The windings, after they are in place, are tested statically and dynamically. The static test is a resistance measurement which assures that all connections are properly made and that the number of turns and wire size in each phase is correct. The dynamic test consists of operating the stator with a rotating magnetic field as a generator. The phase terminal voltage and line-to-line terminal voltages are measured. Compliance with this type of test provides assurance that the deeign flux-linkages have been obtained. Reversed coils, shorted turns, or poor geometrical wire layout would be detected here. All tests are repeated after encapsulation. The test generator would not fit the stator used in this motor and since only one unit was being built, a new generator was not fabricated.

In that the cryogenic mixer motor was the first of its size built, there was some difficulty in establishing the actual flux-linkage level. This necessitated one winding design change. Because of the one unit requirement of this program, production test fixtures for this size hardware were not built. Comparable tests were accomplished using the motor rotor and a test housing.

Evaluation

The mixer was tested to:

(a) Insure that it operated in LH_2, GH_2, GHe with "slugging" flow of mixtures of liquid and gaseous hydrogen.

(b) Measure its performance in each of the above fluids.

(c) Determine the condition of the unit after 100 hr of operation in LH_2.

(d) Evaluate the measured performance and efficiencies with respect to the values calculated during design.

Demonstrations of unit performance in each test fluid (LH_2, GH_2 and GHe) were accomplished at the Lockheed Missles and Space Company Cryogenics Systems Test Facility at Santa Cruz, California. Pressure rise, flow rate, operating speed and input power to the total system (electronics and motor driven mixer) and to the motor were measured.

At the start of testing at Santa Cruz, an irregularity in the shape of two of the switching transistor current waveforms was observed. All other waveforms had the correct shape. This had gone undetected in preliminary checks at room temperature and in liquid nitrogen because only two transistors were looked at by a dual-beam scope to check commutation. The trouble was found to be a reversed coil in one of the stator windings. This was not detectable with normal resistance and inductance measurements because of the nature of the stator and of the problem. The reversed coil could only be detected with the stator electrically excited and a search coil used to measure the field created. This stator had replaced the original stator used for LHe testing because the original stator was damaged during removal from the LHe test housing.

During the initial investigation of the motor waveform problem, a routine check of the power supply voltages revealed that the ±5-V biases were at about ±2.5 V. Investigation of this problem led to the conclusion that this was not a recent "failure" but that this condition had existed undetected for some time. A close look at the data taken during previous motor tests indicated that this voltage was low during those tests, and also that the motor performance was virtually unaffected by this low voltage. The low voltage was caused by a low gain transistor in the series regulator. When the series regulator transistor was replaced, the power supply voltages were restored to the correct levels. During the checkout of the power supply problem, the power consumption of the

magnetic shaft position sensors was measured, and appeared to have increased substantially over earlier measurements.

After eliminating the possibility of significant characteristic changes in the position sensor exciters, a review of the measurement techniques was considered necessary. Careful investigations showed that the low value sampling resistors used to measure excitation current do have a significant reactance at the 100-kHz excitation frequency. The particular 0.1-ohm resistor which was installed on the breadboard indicated a phase shift in the order of 20^0, depending on its lead length and on the exact point of measurement. Calculations now show that the phase shift errors can be reduced to a tolerable level, in the order of 1^0, if a 1-ohm carbon resistor is used for current sampling. To this end, the breadboard was modified and new readings of power consumption were taken. The power consumption of the position sensor is now established to be in the order of 112 mW. This value can be reduced to about 70 mW if the amplitude of the 100-kHz oscillator is reduced by approximately 40 percent. This reduced amplitude is more than adequate for proper operation. However, since this change required a new excitation transformer, it was not incorporated in the present breadboard.

After making the changes to the motor and to the breadboard as noted above, the mixer was operated in both liquid nitrogen and liquid helium in order to check its cryogenic performance as well as to affirm the validity of earlier test results. The load changes required in order to sample the torque-speed characteristic were obtained by varying the depth to which the impeller was submerged in the cryogenic fluids. A plot of this data showed very good agreement with the previous cryogenic development test, and thus the calibration data obtained in the past is valid with the exception of the power lost in the position sensor excitation.

New bearings were installed in the unit and the unit was tested in liquid nitrogen and liquid helium prior to going into test at Santa Cruz. The test setup at Santa Cruz was also found to contain "goose-necks" in which liquid could become trapped, resulting in erroneous pressure readings. These were eliminated before testing was resumed. The testing is reported in Lockheed Report LMSC/73465, which included in this report as Appendix A. The mixer was first calibrated in GH_2 then in LH_2. The total pressure rise was 2.27 in H_2O (565 N/m^2) at 5.01 cfm (2.36×10^{-3} m^3/sec) as opposed to the design goal of 2.0 in. H_2O. There were no design goals for GH_2 operation. The next test was an endurance test of 87 operating hours in LH_2. Shortly after starting this test, a decrease in speed from approximately 2550 rpm to approximately 2250 rpm was observed. Since there was no evidence of distress, testing was continued and the unit successfully operated for 87 hr in LH_2, one hour (approximately) of which was in slugging (liquid and gas mixture) flow. The GHe calibration was then performed and 12 hr of endurance testing in GHe were completed.

At the conclusion of the test it was found that the 5-W 68-Ω shaping resistor had been damaged by some unknown mechanism and its resistance had increased to 120 Ω. This increase in resistance was responsible for the observed reduction in the LH_2 endurance test operating speed. It also reduced the operating speed in GHe.

The actual resistance of the shaping resistor can be determined by calculating the voltage drop across the resistor and dividing by the motor current. (The transistor switch drop is insignificant.) Because of the accuracy of the meter readings involved in this calculation some inconsistency in values at a given load condition can be seen. However, a basic trend showing resistor degration and a change in value from approximately 65 Ω to approximately 120 Ω over the test period can be established. This occurred because inadvertently a wire-wound resistor was not used.

The speed at which a dc motor will run is established when the sum of the generated back emf and the voltage drop in the stator winding is equal to the voltage at the motor terminals. Thus, knowing the motor voltage, the back emf constant (volts/rpm) and the motor current, the effective motor winding resistance (R_m) can be calculated.

$$R_m = \frac{\text{Motor Voltage - (Back emf Constant) (RPM)}}{\text{Motor Amps}}$$

Using this relationship with the test data of LMSC/73465 Report pages 12, 13, and 14, it appears the motor winding resistance per phase varies from 8.5 ohms to 16 ohms, the higher values being associated with the higher current. Again the accuracy of the readings reflect in this calculation, but the fundamental result indicates that the basic resistance of the winding is higher than assumed from analytical data on pure copper at cryogenic temperatures. This may be due to impurities in the copper magnet wire and internal heating due to the motor current. Increasing this current correspondingly increases the stator I^2R loss which tends to increase the stator resistance.

The performance in GHe was calculated for the mixer operating with a 68-Ω resistor.

$$N_{CORR} = N_{OBS} \left[\frac{V_{MTR} - 68\ (I_{CORR})}{V_{MTR} - 120\ (I_{OBS})} \right]$$

But, I is proportional to T and, for a fan, T is a function of N^2; therefore, I is a function of N^2

$$I_{CORR} = I_{OBS} \left(\frac{N_{CORR}}{N_{OBS}} \right)^2$$

A quadratic solution to the above equations results in:

$$N_{CORR} = \left\{ \frac{-V_{MTR} + 120\ (I_{OBS}) \pm \sqrt{\left|(V_{MTR} - 120(I_{OBS})\right|^2 - 4\left\{\left[\frac{68(I_{OBS})}{N_{OBS}}\right]\left[-N_{OBS}\ V_{MTR}\right]\right\}}}{2\left[\frac{68\ (I_{OBS})}{N_{OBS}}\right]} \right\}$$

$$= \left\{ \frac{-26.2 + 120\ (.018) \pm \sqrt{\left|26.2 - 120(.018)\right|^2 - 4\left\{\left[\frac{68(.018)}{3700}\right]\left[-3700(26.2)\right]\right\}}}{2\left[\frac{68(.018)}{3700}\right]} \right\}$$

$$N_{CORR} = 3838 \text{ RPM.}$$

The flow rate is a linear function of speed. The pressure rise is a squared function of speed. The power is a cubic function of speed; however, in plotting the corrected figure 4-35 curves, the 120 ohm shaping resistor power was subtracted. The cubic relationship on speed was then applied and the power consumed by a 68-ohm shaping resistor was added back in. An additional correction proportional

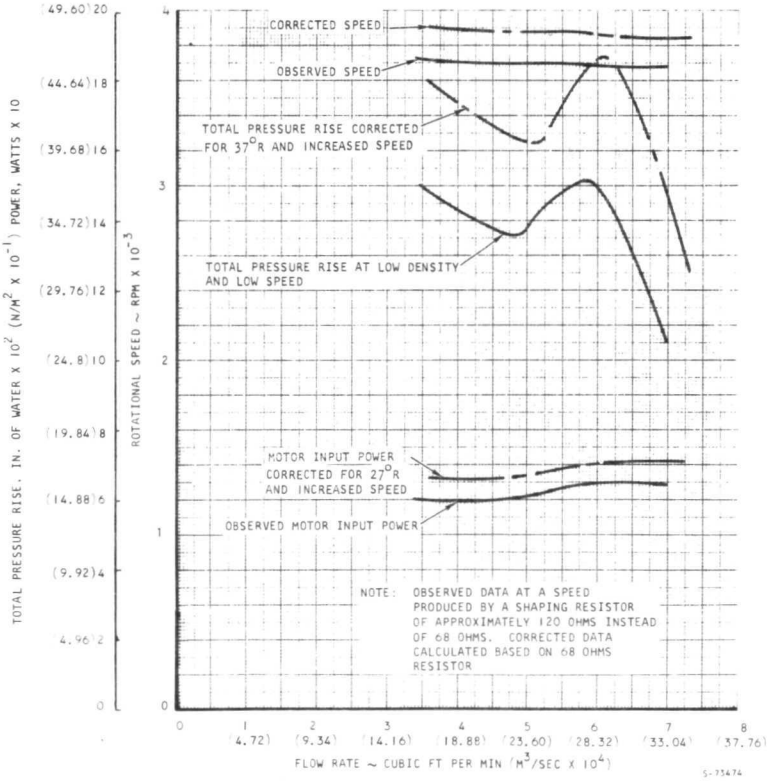


Figure 4-35. Power, Speed and Pressure Rise of a Mixer Unit PN 605632-1-1 as Functions of Flow, Operating at Temperatures Near 41°R in Gaseous Helium and 16 psia

to the density change was then made. The dashed curves of fig. 4-35 were calculated from those relationships to account for the speed increase operating with a 68 ohm resistor. The total pressure rise was calculated to be 0.166 in. H_2O or 20.5 percent lower than the design goal of 0.2 in. H_2O. If the 0.2-in. H_2O pressure rise were required in gaseous helium, the best method of achieving it would be by reducing the impeller tip diameter to 1.69 in. (from 1.8 in.) and increasing the motor speed by 9 percent in GHe and 13 percent in LH_2.

Figs. 4-36 through 4-40 are plots of measured performance and calculated efficiences in LH_2, GH_2 and GHe. The curves are smooth plots to show the true performance rather than exactly joining every data point. The rotational speed and flow rates were taken directly from test data. The test measured pressure rise from total-to-static. The pressure rise was converted to a total-to-total basis by adding one velocity head as discussed under design philosophy. Input power to the electronics was the product of applied emf and applied current. Motor power (in tank power) is the product of motor emf and current plus the power lost in the position sensors less the power returned from the motor to the electronics and dissipated in the electronics as switching losses. The position sensor losses were measured and found to be 112 mW. The switching power is composed of two components: (1) the energy dissipated in the switching transistor is $\frac{LI^2}{2}$, and (2) the I^2R in the current sensing resistor. In LH_2 at 6.02 cfm there are:

$$PWR_L = \frac{RPM(P)W}{60(2)} \quad (1.45 \times 10^{-2})\ I^2/2$$

$$= \frac{2590(6)4}{60(2)} \ (1.45 \times 10^{-2}) \ \frac{(.116)^2}{2} = 5.053 \times 10^{-2} W$$

$$PWR_R = I^2R$$

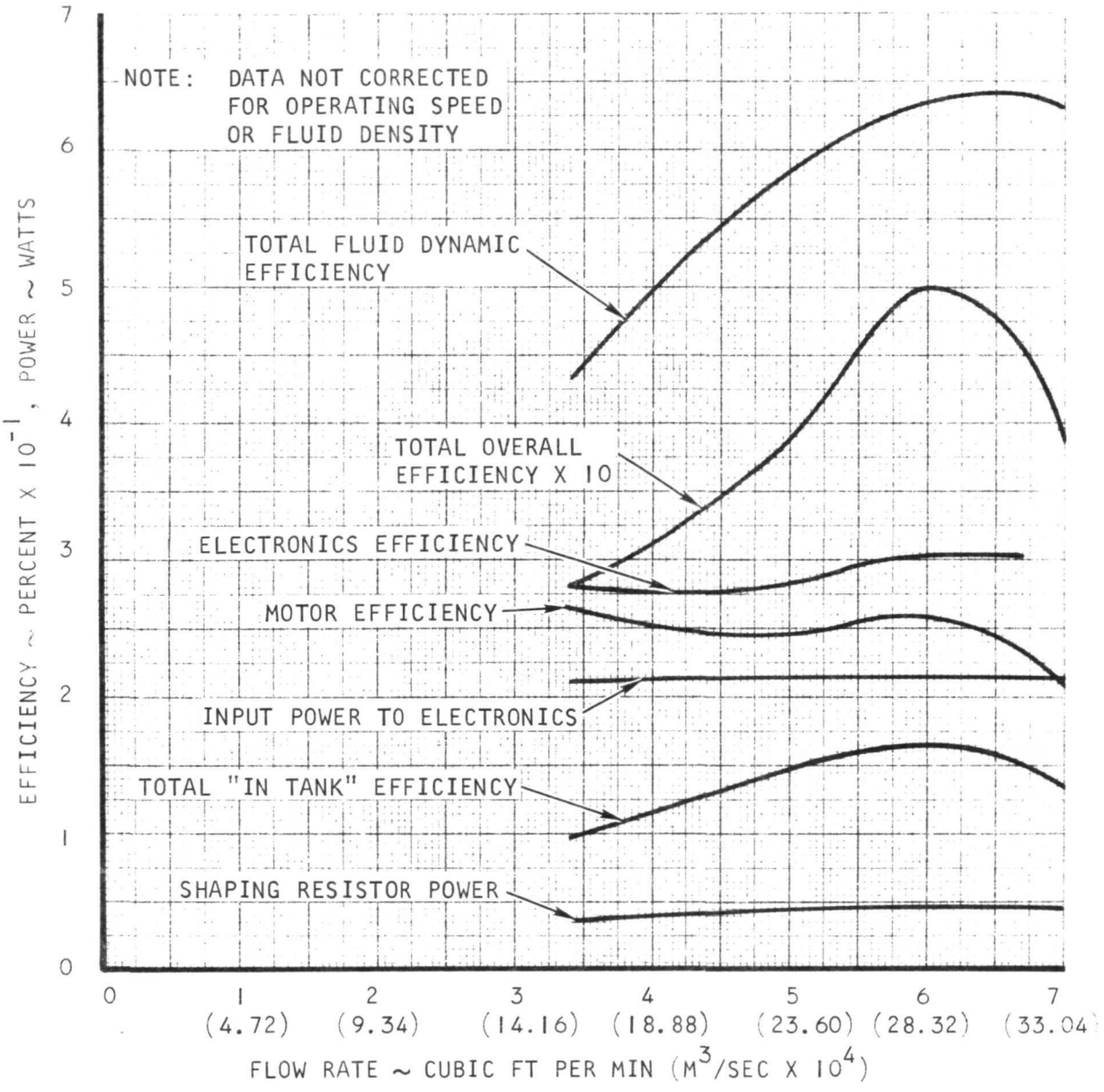
$$R = 1\Omega$$

$$PWR_R = (0.116)^2 \ (1) = 0.0135 \ W$$

"In-tank efficiency" is fluid dynamic power divided by motor input power.

$$\eta_{it} = \frac{11.7 \times 10^{-2} \ (CFM)\Delta P}{E_{mtr} \ I_{mtr} + PWR_{sensors} \ PWR_{switch}} \quad X100$$

At 6.02 cfm ($2.84 \times 10^{-3} m^3/sec$), ΔP_t = 1.94 in H_2O (358. N/m^2)



S-73472

Figure 4-36. Power and Efficiencies as Functions of Flow Rate of a Mixer Unit PN 605632-1-1 Operating in Gaseous Helium at Temperatures Near 41°R (23°K)

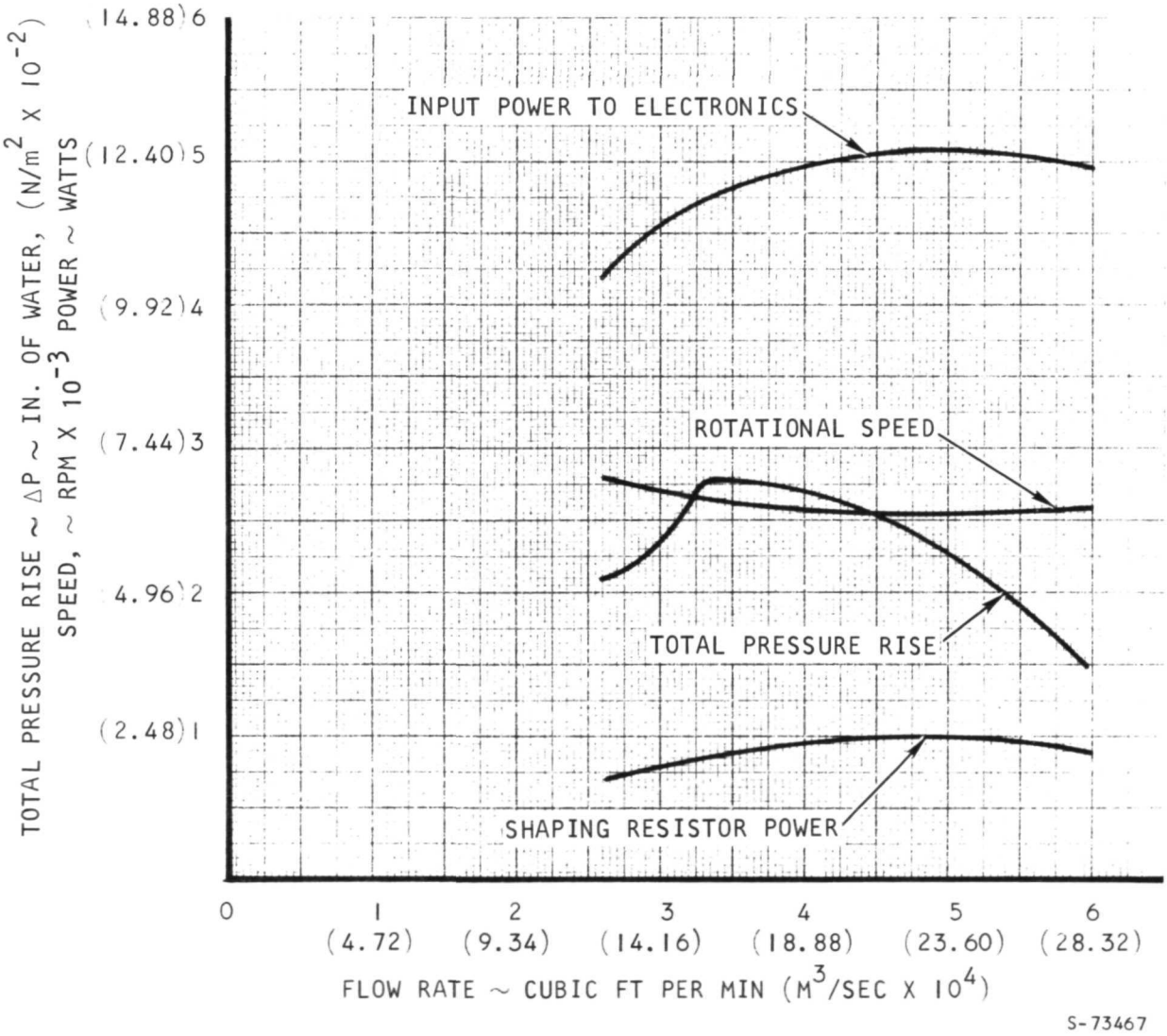


Figure 4-37. Power, Speed and Pressure Rise as Functions of Flow for a Mixer Unit, AiResearch PN 605632-1-1, Operating in 37°R (20°K) Liquid Hydrogen

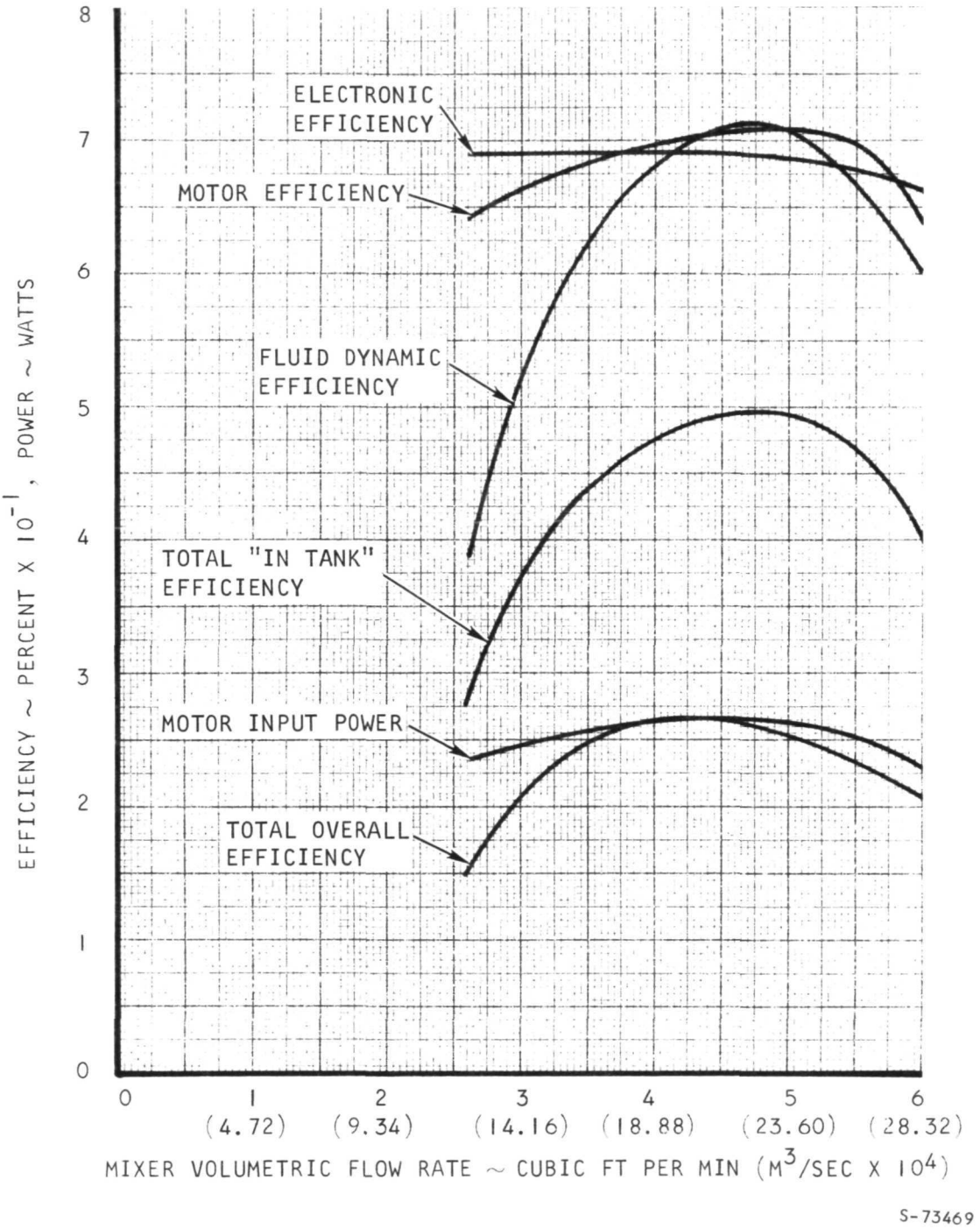


Figure 4-38. Efficiencies and Motor Power as Functions of Flow for a Mixer Unit, AiResearch PN 605632-1-1 Operating in 37°R (20°C) Liquid Hydrogen

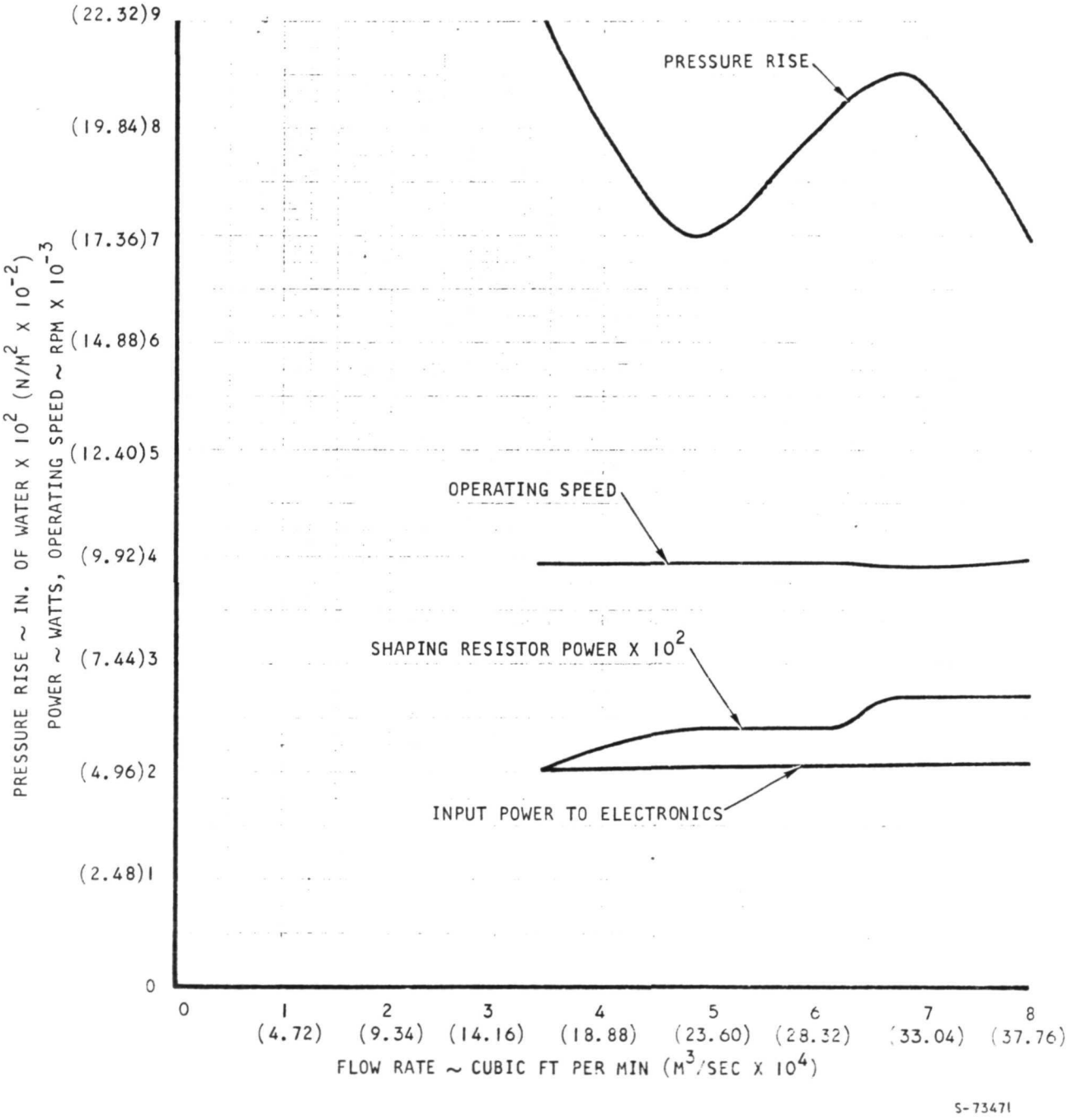


Figure 4-39. Pressure Rise, Speed and Power of a Mixer Unit, AiResearch PN 605632-1-1 as Functions of Flow Operating in Gaseous Hydrogen at 38°R and 14 psia

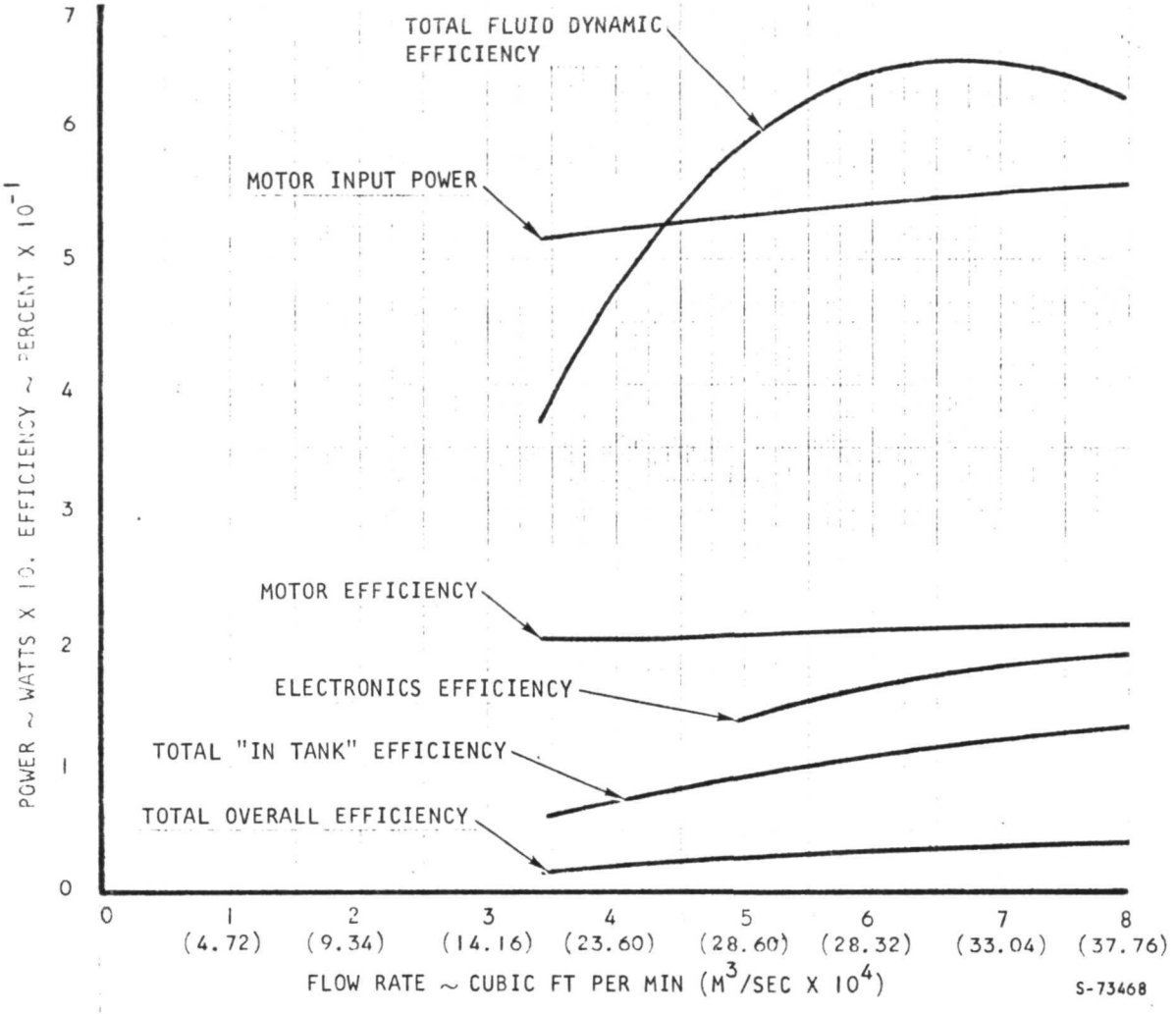


Figure 4-40. Efficiencies and Power of a Mixer Unit, AiResearch PN 605632-1-1 as Functions of Flow Operating in Gaseous Hydrogen at 38^0R and 14 psia

$$\eta_{it} = \frac{11.7 \times 10^{-2} (6.02)\ 1.44}{20.7\ (.116) + 0.11 - .013 - 0.05} \times 100$$

$$\eta_{it} = 41.6 \text{ percent}$$

In a similar fashion the total overall efficiency is fluid dynamic power divided by input power to the electronics:

$$\eta_{oa} = \frac{11.7 \times 10^{-2}\ (CFM)\ \Delta P}{E_{in}\ I_{in}} \times 100$$

$$= \frac{11.7 \times 10^{-2} (6.02)\ (1.44)}{28.6\ (0.173)} \times 100$$

$$= 20.5 \text{ percent}$$

The power input to the shaping resistor is:

$$\text{WATTS} = I_{mtr}^{\ 2} R_{shape}$$

$$= (0.116)^2\ (68)$$

$$= 0.91 \text{ W}$$

The electronics efficiency is:

$$\eta_{EL} = \frac{E_{mtr}\ I_{mtr} + I_{mtr}^{\ 2} R_{shape}}{E_{in}\ I_{in}}$$

$$= \left[\frac{20.7\ (0.116) + (0.116)^2\ 68}{28.6\ (0.173)}\right] \times 100$$

$$= 67.0 \text{ percent}$$

Motor efficiency is the shaft output power divided by the input power ($E_{mtr}\ I_{mtr}$). In order to obtain motor efficiency, the shaft load must be known. Measurement of torques of 0.05 to one oz-in. at liquid hydrogen temperature is very difficult because no known convenient method exists. As a result, it was decided to calibrate the mixer impeller in air, correct for operating fluid density, and use it as the load to determine motor shaft power. The methods for accomplishing the calibration are discussed in Appendix B (Section 4 of AiResearch Report 68-4223). The calibration data were obtained for these conditions and are presented in Lab Data Sheets on tables 4-1 through 4-3. It was originally intended to maintain complete dimensional similarity between test and operation by adjusting the air pressure such that:

$$\rho_{cal} = \rho_{operating} \frac{\mu_{cal}}{\mu_{operating}}$$

For LH_2 this is:

$$\rho_{cal} = 4.38 \frac{(1.27 \times 10^{-7})}{0.88 \times 10^{-7}}$$

$$\rho_{cal} = 6.32\ LB/FT^3 (100.8 kg/m^3)$$

Which corresponds to a pressure of 1260 psia ($8.69 \times 10^6\ N/m^2$) at 80°F (29°C) rather than the 161 ($1.11 \times 10^5 N/m^2$) Psia called out in report 68-4223. The pressures specified to simulate conditions in GHe and LH_2 contain similar errors. The test data was corrected by solving for the Reynolds number at test conditions as described in the design philosophy section and finding the aerodynamic efficiency from fig. 4-1. This figure is a plot of the ratio of actual efficiency obtained by AiResearch fans to the efficiency available at Reynolds numbers above 3×10^5. The Reynolds number under operating conditions was computed and its relative efficiency found from fig. 4-1. The calibration efficiency was found and increased by the ratio of operating efficiency to calibration efficiency as follows:

From aerodynamic test data at 148 psig (table 4-1) at a flow rate of 6.02 cfm

$N_{R\ cal} = 9.4 \times 10^4$

$\eta_{f\ cal} = 88.7$ percent relative

$N_{R\ LH_2} = 7.04 \times 10^5$

$\eta_f = 100$ percent relative

TABLE 4-1

FORM #1339A
AIRESEARCH MFG. CO.

FAN LAB DATA SHEET

Page ____ of ____

EWO 3404-25089-02-0102 DATE 7-28-67 TEST PURPOSE DEVELOPMENT: CALIBRATE LH_2 MIXER

P/N 605632-1-1 BAROM — UNIT IN 198 PSIG AIR

S/N ____ TEMP — TEST PERS. WEAVER & MORGAN

NO.	1	2	3	4	5	6	7	8	9	10	11	12	13	14	15	REMARKS
	INLET PRESS (TANK) PSIG	FAN SPEED CPS	FLOW METER #2903 CPS	INLET TEMP °F	FAN PRESS RISE IN H_2O	MOTOR EMF D.C. VOLTS	MOTOR CURRENT MA		FAN SPEED RPM	FAN FLOW CFM						
1	148	510	43.5	82	0.330	27.7	31.0		2550	6.45						
2	148	516	36	80	0.420	27.7	31.0		2579	4.65						
3	148	529	25.5	80½	0.405	26.8	27.3		2691	3.55						
4	148	556	18	82	0.400	26.5	26.5	A	2780 2590	2.6						
5																
6																
7																
8																
9																
10																
11																
12																
13																
14																
15																
16																
17																
18																
19																
20																
21																

TABLE 4-2

FORM #1339A
AIRESEARCH MFG. CO.

FAN LAB DATA SHEET Page ____ of ____

EWO 3404-250089-02-0100 DATE 7-28-69 TEST PURPOSE DEVELOPMENT: CALIBRATE LH2 MIXER

P/N 605632-1-1 BAROM — UNIT IN 60.5 PSIG AIR

S/N — TEMP — TEST PERS. WEAVER & MORGAN

NO.	1	2	3	4	5	6	7	8	9	10	11	12	13	14	15	REMARKS
	INLET PRESS (TANK) PSIG	FAN SPEED CPS	FLOW METER #2903 CPS	INLET TEMP °F	FAN PRESS RISE IN H_2O	MOTOR EMF D.C. VOLTS	MOTOR CURRENT MA		FAN SPEED RPM	FAN FLOW CFM						
1	60.5	778	61	79	0.310	35.5	31.8		3790	8.0						
2	60.5	782	50	80	0.365	35.2	31.1		3910	6.8						
3	60.5	784	45	80	0.360	35.0	29.7		3920	6.2						
4	60.5	784	38	81	0.350	34.4	27.0		3920	4.9						
5	60.5	786	23.5	82	0.300	34.1	25.4			3.4						
6																
7																
8																
9																
10																
11																
12																
13																
14																
15																
16																
17																
18																
19																
20																
21																

TABLE 4-3

FORM #1339A
AIRESEARCH MFG. CO.

FAN LAB DATA SHEET

Page ____ of ____

EWO 3404-250088-02-0102 DATE 7-22-69 TEST PURPOSE DEVELOPMENT: CALIBRATE A LIQUID HYDROGEN MIXER UNIT IN 17.5 PSIG AIR

P/N 605632-1-1 BAROM —

S/N ____ TEMP — TEST PERS. WEAVER & MORGAN

NO.	1	2	3	4	5	6	7	8	9	10	11	12	13	14	15	REMARKS
	INLET PRESS (TANK) PSIG	FAN SPEED CPS	FLOW METER #2903 CPS	INLET TEMP °F	FAN PRESS RISE IN H_2O	MOTOR EMF D.C. VOLTS	MOTOR CURRENT MA		FAN SPEED RPM	FAN FLOW CFM						
1	17.5	736	47.5	80	0.100	29.3	18.1		3680	7.0						
2	17.5	736	45.0	80	0.100	28.3	18.0		3680	6.7						
3	17.5	736	42.5	80	0.105	29.3	17.85		3680	6.4						
4	17.5	736	39.5	80	0.105	28.2	17.5		3680	6.0						
5	17.5	740	34.9	80	0.105	28.1	16.85		3700	5.3						
6	17.5	740	30.5	80	0.095	28.9	16.1		3700	4.0						
7	17.5	745	20.0	80	0.085	28.1	14.9		3725	3.4						
8																
9																
10																
11																
12																
13																
14																
15																
16																
17																
18																
19																
20																
21																

So the test fan efficiency was increased to:

$$\frac{100}{88.7} = 1.13 \text{ times the test value}$$

$$\eta_f = \frac{\text{Aerodynamic hp}}{\text{Shaft hp}}$$

$$\text{Shaft hp} = \frac{T\ (\text{rpm})}{1.013 \times 10^6}$$

Where torque was determined from the room temperature motor calibration as plotted in fig. 4-41. Over the range of values plotted, motor torque was a linear function of motor current. At 5.45 cfm, motor current = 31 ma, so from fig. 4-20, the torque was 0.1865 oz-in., rpm = 2550

$$\text{Shaft hp} = \frac{0.1865\ (2550)}{1.013 \times 10^6}$$

$$= 4.7 \times 10^{-4} \text{ hp}$$

With an observed pressure rise of 0.305 in H_2O the air hp is:

$$\text{hp} = 0.000157\ (\text{cfm})\ \Delta P$$

$$= 0.000157\ (5.45)\ .305$$

$$= 2.61 \times 10^{-4}$$

So the test aerodynamic efficiency is:

$$\eta_f = \frac{\text{Air hp}}{\text{Shaft hp}} \times 100$$

$$= \frac{2.61 \times 10^{-4}}{4.7 \times 10^{-4}} \times 100$$

$$= 55.5 \text{ percent}$$

Correcting for N_R effects:

$$\eta_{f\ \text{correct}} = 55.5\ (1.13) = 62.7 \text{ percent}$$

The motor efficiency, then was found by dividing the "in tank" efficiency by the fluid dynamic efficiency; thus at 5.45 cfm in LH_2 this is:

$$\eta_{mtr} = \frac{47.5}{.67} = 71 \text{ percent}$$

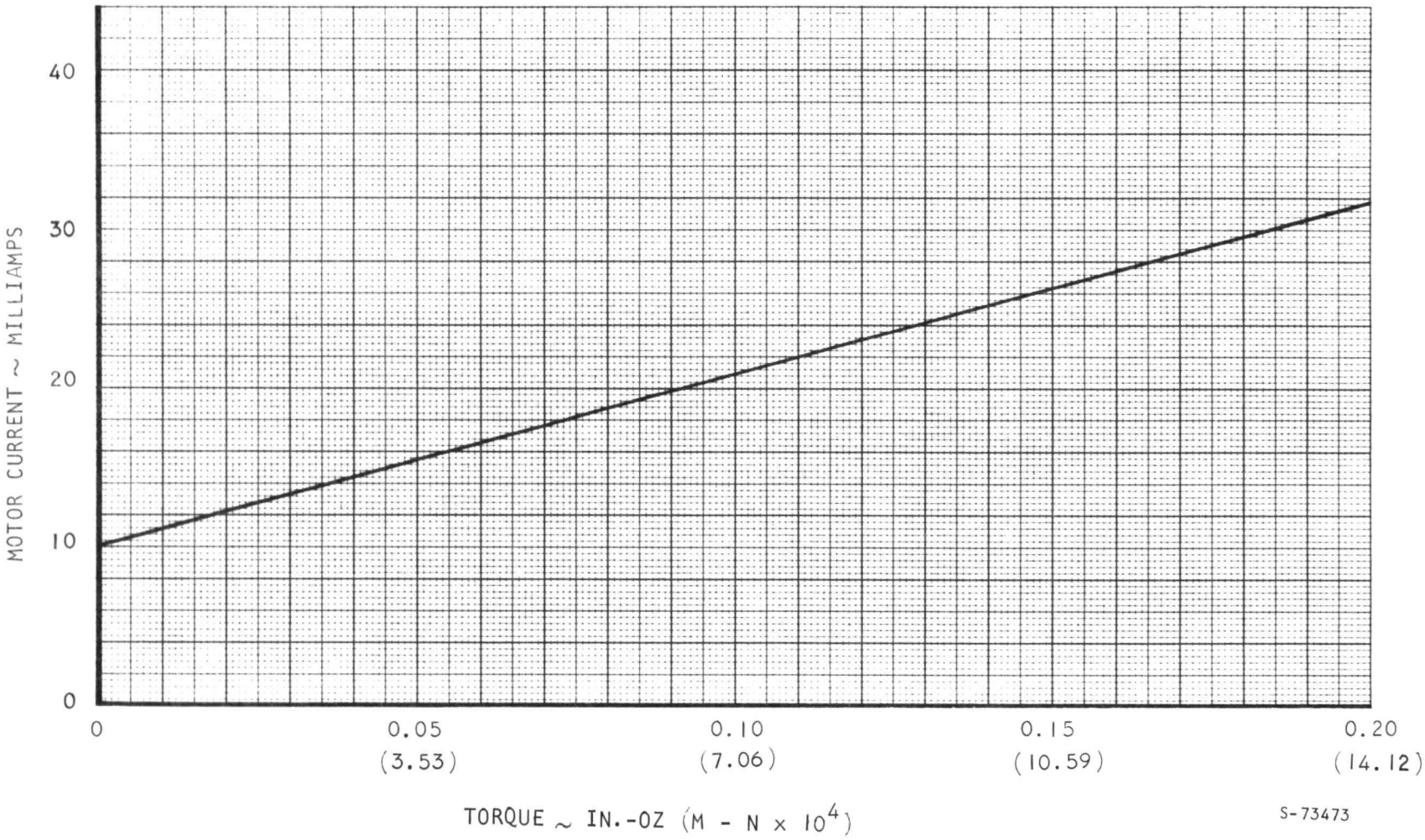


Figure 4-41. Shaft Torque as a Function of Current for Liquid Hydrogen Mixer Motor at Room Temperature

The gaseous helium data is plotted in figs. 4-35 and 4-36. All observed data and values calculated directly from observed data are shown as solid lines. All calculated data based on increased speed conditions to correct for the improper resistor value, are shown dashed. The performance at the design point is 20 percent low. This performance reduction was caused in part by operation at slightly less than design speed. It is hypothesized that this slightly lower speed may have been caused by the use of a slightly more powerful magnet in the motor rotor than design calculations assumed. Operation at design speed would have resulted in a pressure rise of approximately 2.2 in. H_2O, or essentially the design point pressure rise at aerodynamic stall.

It was intended that the GHe operating point would be at or just to the right of aerodynamic stall. Aerodynamic stall was computed from fig. 4-2 using the methods set forth in the design philosophy section. Actual aerodynamic stall took place at approximately 6.1 cfm (2.87 m^3/sec) instead of 5.3 cfm (2.49×10^{-3} m^3/sec). This indicates that the fluid incidence angle with the blade was lower than normally associated with stall. The reasons for the shift are unknown; it is believed that possible errors in measurement are unlikely to have caused the apparent shift. It is possible that at lower Reynolds Numbers, the impeller hub and tip clearances from the housing may exert larger influences than formerly throught. This could result in more tip leakage which would cause premature boundary layer separation at the blade tip, resulting in a premature stall.

The liquid hydrogen test (see figs. 4-37 and 4-38) produced 13 percent more performance than predicted, probably because the forecast fluid dynamic losses were higher than those that actually occurred and because 10 percent of excess performance was built into the design by not fully allowing for efficiency improvements due to increases in N_R. Since the design torque was not required, power consumption was lower than forecast. The dashed portion of the fluid dynamic efficiency curve is extrapolated.

There were no requirements for flow or pressure rise in GH_2, so no analysis of that condition was made. With motor power of the order of 0.4 W and mixer pressure rises of the order of 0.1 in. H_2O, values become so small that accuracy diminishes rapidly. The general trend of the data in figs. 4-39 and 4-40 appears proper, but the apparent steps and discontinuities of the curves of efficiencies and shaping resistor power probably are cumulative measurement errors.

At the conclusion of the cryogenic testing, the mixer was disassembled and inspected. Other than the partially failed shaping resistor, no signs of damage or distress could be found. The bearings were removed and examined in detail the bearings had operated for more than 100 hr. At liquid hydrogen temperature plus approximately half an hour in liquid nitrogen and liquid helium, and approximately 10 min. in room temperature air. Fig. 4-42 and 4-43 are photographs of the bearings with their shields removed; fig. 4-44 through 4-47 show them disassembled. Only three balls of each bearing were shown to avoid possible cluttering of the photo, although there was no observable difference in the balls. The

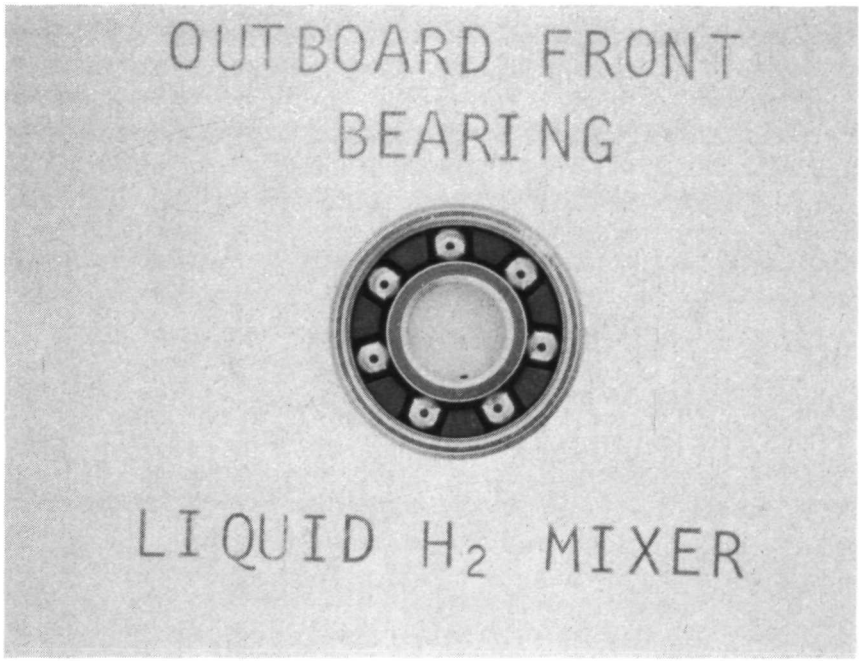


Fig. 4-42 AiResearch PN 605632-1-1, with shield removed after 100 hr test

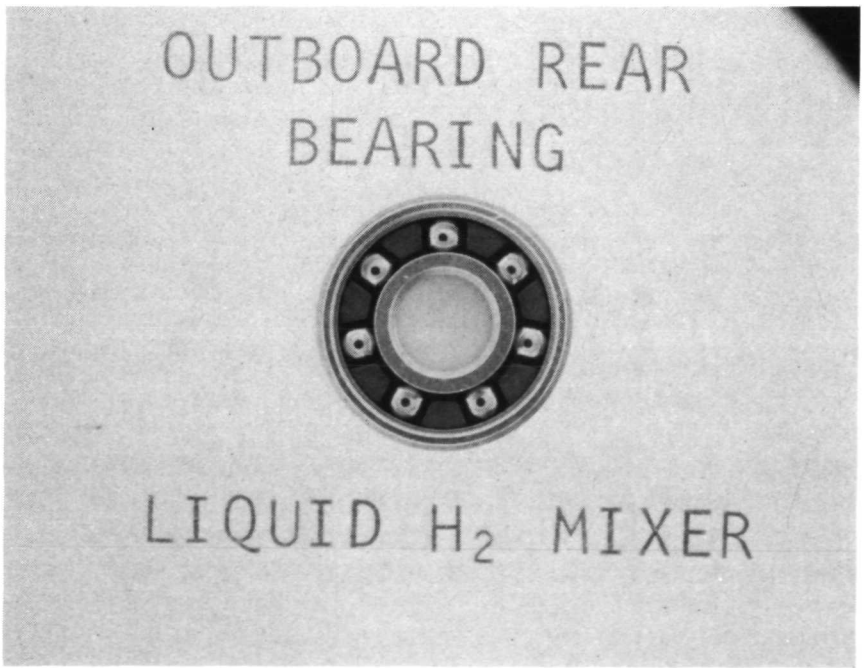


Fig. 4-43 AiResearch PN 605632-1-1, with shield removed after 100 hr test

F-16233

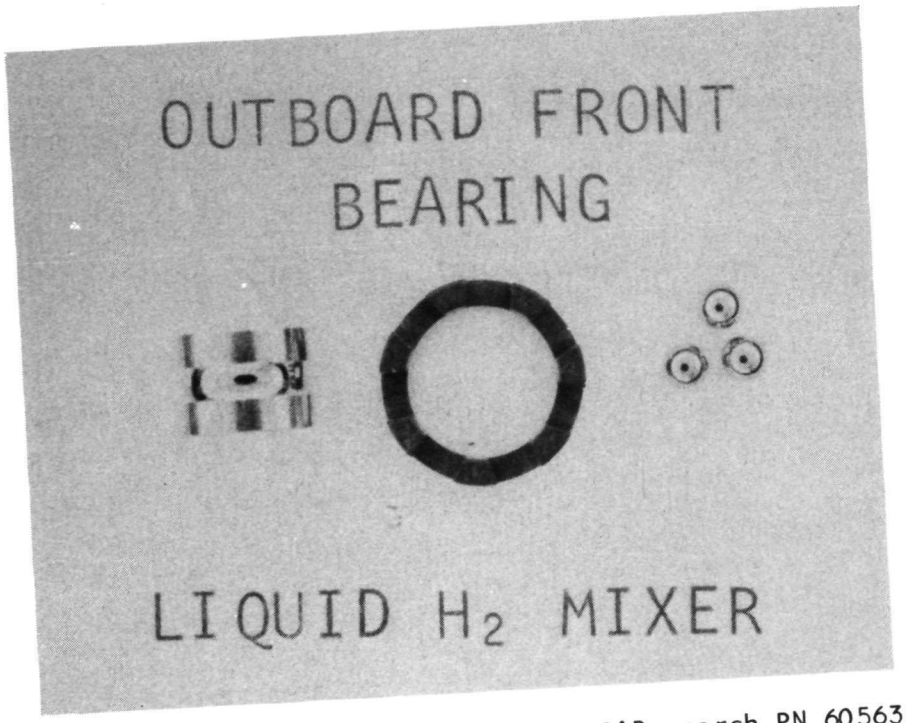


Fig. 4-44 Disassembled after 100 hr test, AiResearch PN 605632-1-1

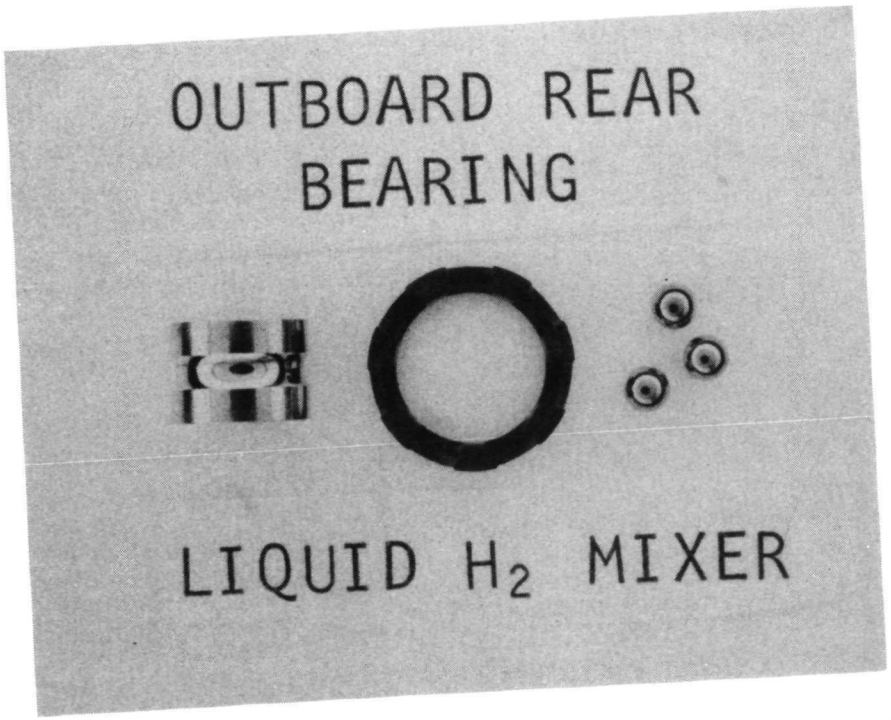


Fig. 4-45 Disassembled after 100 hr test, AiResearch PN 605632-1-1

F-16232



Figure 4-46. Enlarged View of Liquid Hydrogen Mixer, AiResearch PN 605632-1-1, Front Bearing Inner Race and Ball Separator Showing No Signs of Distress After 100 Hr Test

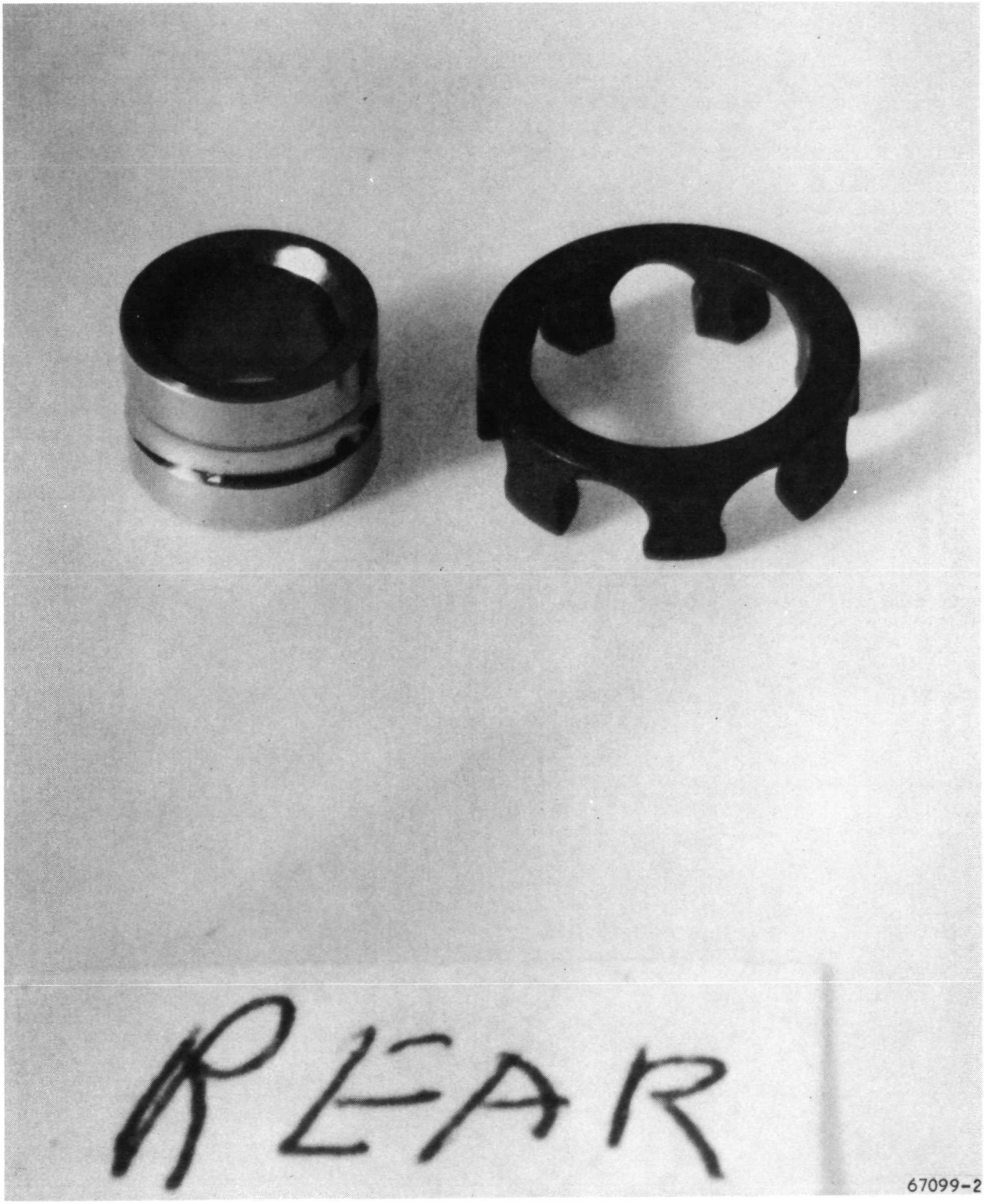


Figure 4-47. EnlargedView of Liquid Hydrogen Mixer, AiResearch PN 6056352-1-1, Rear Bearing Inner Race and Ball Separator, Showing No Signs of Distress After 100 Hr Test

bearings were microscopically examined and found to be in excellent condition and would have very possibly operated for 5000 hr in LH_2. Appendix D is a copy of the bearing report.

SECTION 5
CONCLUSIONS

The mixer performed well in all fluids. Performance was in excess of design goals in LH_2 and almost up to design goals in GHe.

Should it be desired to reduce weight, the basic material of construction could be changed from stainless steel to aluminum.

In-tank power could be reduced by 50-75 mw by reducing the position sensor voltage. A more substantial change could probably be achieved by further development and use of photo-electric position sensors.

It is believed that a redesign of the electric cable header at the mixer would eliminate the problem of glass cracking found in this program.

The impeller tip diameter could be reduced to approximately 1.695 inches (4.3×10^{-2} m) and the operating speeds increased nine percent to provide higher GHe performance, but at reduced LH_2 efficiency.

For space flight applications, the functions of the shaping resistor could be performed by a chopper. This would improve overall efficiency at the expense of added complexity.

Before the electronics could be used in a low temperature environment, either the electronics would have to be redesigned using components (such as f e t semiconductors) compatible with such low temperatures or a heater blanket would have to be provided to raise the temperature to acceptable levels. Postulating an electronics package 3 in (7.6×10^{-2} m) square and 2 in (5.1×10^{-2} m) thick, covered with a blanket having an emissivity of 0.3, mounted on three 1/2 in (1.3×10^{-2} m) dia by 1/2 in (1.3×10^{-2} m) high legs having a thermal conductivity of 1.5 Btu/hr-ft^2-^{0}F-in, and a 260^{0}F (127^{0}C) ΔT, an input of approximately 6.8 w of heating power would be required.

SECTION 6
RECOMMENDATIONS

It is recommended that the following tasks be undertaken to extend the work of this program:

1. Develop electronics capable of operating efficiently and reliabily at spacecraft temperatures below -65°F (-54°C) without resorting to heaters.

2. Perform extended life testing of the mixer bearings in liquid hydrogen.

APPENDIX A

LMSC REPORT

EVALUATION AND DEMONSTRATION BRUSHLESS DC MIXER UNIT

Report No. LMSC/73465 July 15, 1969

NOTES OF EXPLANATION TO LMSC/73465

All oscillograph traces are for 20 V/cm at a sweep rate of 150 ms/cm. Oscillograph traces were taken across the electronics unit switching transistors. These traces were arranged with phases A through D presented successively from the top to the bottom of each page of oscilloscope data. The endurance testing traces were for operation in LH_2 except for the endurance tests in GH_e which are identified. The operating speeds corresponding to these oscillograph traces are presented in the raw test data sheets.

COPY NO.

REPORT NO. LMSC/73465

DATED July 15, 1969

REVISED

LOCKHEED MISSILES & SPACE COMPANY

A GROUP DIVISION OF LOCKHEED AIRCRAFT CORPORATION

SUNNYVALE, CALIFORNIA



TITLE

Evaluation and Demonstration

Brushless DC Mixer Unit

SUBMITTED UNDER

EFFECTIVE UNDER

MODEL _____ REFERENCE _____

PREPARED BY D. R. Stevenson GROUP Cryogenics Systems Test
Santa Cruz Test Base

CHECKED BY _____ APPROVED BY W. H. Sterbentz, Mgr.
Propulsion Vehicle Systems

REVISIONS

DATE	REV. BY	PAGES AFFECTED	REMARKS

FOREWORD

This test report documents the activity performed by Lockheed Missiles and Space Company under AiResearch Contract P0025-49011-9, "Evaluation and Demonstration Test Program, Brushless DC Mixer Unit". This activity is part of NASA LeRe contract NAS 3-11208 for the "Development and Demonstration of a Liquid Hydrogen Brushless DC Mixer Unit".

TABLE OF CONTENTS

	Page
Foreword	i
1.0 Scope	1
2.0 Summary	1
3.0 Description of Test Program	1
3.1 Introduction	1
3.2 Test Facility Description	3
3.3 Testing Discussion	4
4.0 Appendix	9
Test Data	9
Oscilloscope Traces	9

FORM LMSC 8941-A

LIST OF FIGURES

Figure 1 Electronic Breadboard and Mixer

Figure 2 GH_2/LH_2 Test Setup Schematic

Figure 3 GH_2/LH_2 Test Setup Photograph

Figure 4 GHe Test Setup Schematic

Figure 5 GHe Test Setup Photograph

1.0 Scope

This report describes the testing performed by Lockheed Missiles and Space Company on a Brushless DC Motor-Mixer Unit which is designed for use in cryogenic propulsion vehicle tankage. Figure 1 is a photograph of the unit tested which shows electronic breadboard and mixer.

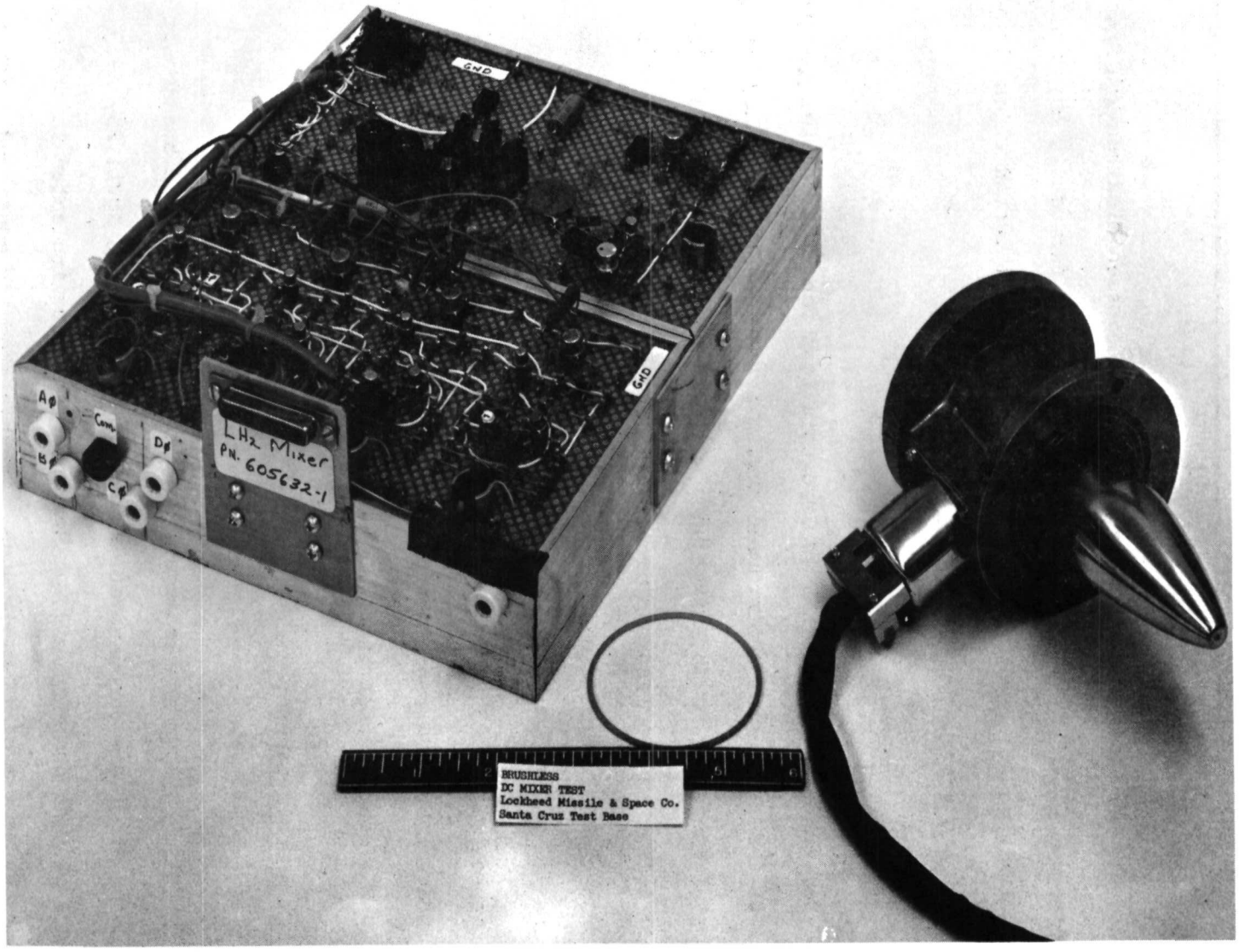
2.0 Summary

The tests were performed at LMSC's Cryogenic test facility located at their Santa Cruz Test Base. The tests performed during months of June and July 1969 demonstrated functional operation of the mixer unit with gaseous hydrogen, liquid hydrogen and gaseous helium in the liquid hydrogen temperature region. Electrical and hydraulic performance data was obtained for mixer operation under these conditions and is presented in the appendices. The unit was operated for a total of 100 hours of which approximately 87 hours were in hydrogen, thus demonstrating endurance of the unit. The unit's operation during liquid and gaseous hydrogen slugging conditions was also demonstrated.

3.0 Description of Test Program

3.1 Introduction

The mixer system consisting of an electronic solid state breadboard and DC motor was first received at Santa Cruz Test Base on April 28, 1969. Testing was started on May 5, 1969. Some problems were indicated in the electrical system of the breadboard-motor. Trouble shooting continued through May 8, 1969. On May 9, 1969, the unit was returned to AiResearch, Torrance, Californiia, for identification of electrical problem and repair. Total run time of unit at this time was 11.2 hours. On June 9, 1969, the repaired unit was returned to Santa Cruz Test Base. Testing of unit was started on June 18 and proceeded to completion on July 10, 1969.



F-16045

Figure 1.

3.2 Test Facility Description

The test program discussed herein was conducted in the Cryogenic Test Facility at LMSC's Santa Cruz Test Base. The capabilities of this facility include storage and transfer equipment for liquid hydrogen, liquid nitrogen and liquid oxygen; gaseous helium, gaseous hydrogen, gaseous nitrogen storage and distribution systems; and varied and high accuracy data acquisition equipment. Specific test equipment and instrumentation equipment used during this program is listed below:

3.2.1 Components test dewar 22 inch diameter by 40 inches deep.

3.2.2 Liquid hydrogen storage and transfer system.

3.2.3 Dymec 2010J digital integrating voltmeter with paper tape printer recorder.

3.2.4 DC power supply, Trygon Electronics SHR 20-3.

3.2.5 Oscilloscope, Techtronix 535 with Polaroid photographic equipment.

3.2.6 Inclined water manometer, 0 to 2 inch range.

3.2.7 Pressure Transducer, 0 to 10 inch H_2O range; CCC-41GP14A.

3.2.8 Pressure Transducer, 0 to 50 psia range; CEC-4-354-0118.

3.2.9 Fluid Temperature Transducer, 0 to 50°R range; Cryo Cal CR-2500L-14-100.

3.2.10 Fluid Temperature Transducer, 0 to 520°R range; Rosemont 150MA10.

3.2.11 Flowmeter; 0 to 25 CFM range; 2 inch diameter Potter special, 66101A.

3.3 Testing Discussion

3.3.1 Calibration in Gaseous Hydrogen

The motor-mixer unit was installed in the upper half of the 2 inch test loop as shown schematically in Figure 2. Figure 3 is a photograph of this setup prior to installation in test dewar. Upon completion of installation in the test dewar, the internal systems were dried by evacuation to 10 microns, holding for a minimum of 15 minutes and then back filling internal systems with dry gaseous nitrogen. The internal systems were then purged with boil-off hydrogen gas at ambient temperature. Liquid hydrogen was then admitted to the test dewar and filled to a level approximately 8 inches below the mixer inlet level. The unit was then started by application of 29 VDC to the breadboard electronics package. Performance data was obtained at flow rates from 8.0 CFM to 3.4 CFM by adjustment of the loop throttling valve. Complete performance data obtained from this test is presented in the appendix.

3.3.2 Calibration in Liquid Hydrogen

This test continued from the gaseous hydrogen calibration described above by filling the test dewar with liquid hydrogen to above the top of the test loop. Performance data was obtained at flow rates from 6.0 CFM to 2.6 CFM by adjustment of the loop throttling valve. With throttling valve full open, maximum flow rate of 6.0 CFM was obtained. Complete performance data from this test is presented in the appendix.

Prepared	NAME	DATE	LOCKHEED MISSILES & SPACE COMPANY A GROUP DIVISION OF LOCKHEED AIRCRAFT CORPORATION	Page	TEMP	PLAN
Checked			TITLE LH_2/GH_2 Testsetup	Model		
Approved				Report No.		

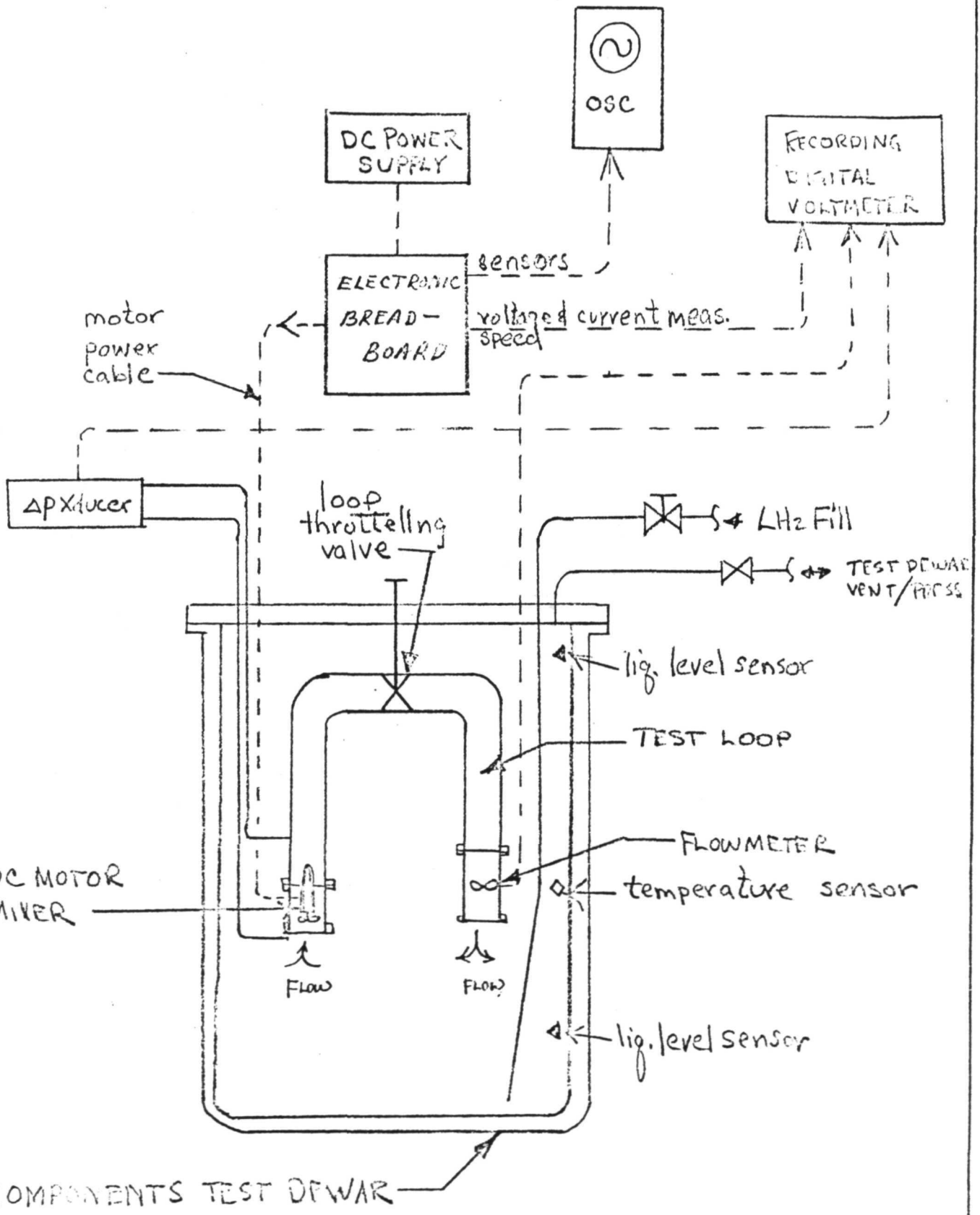
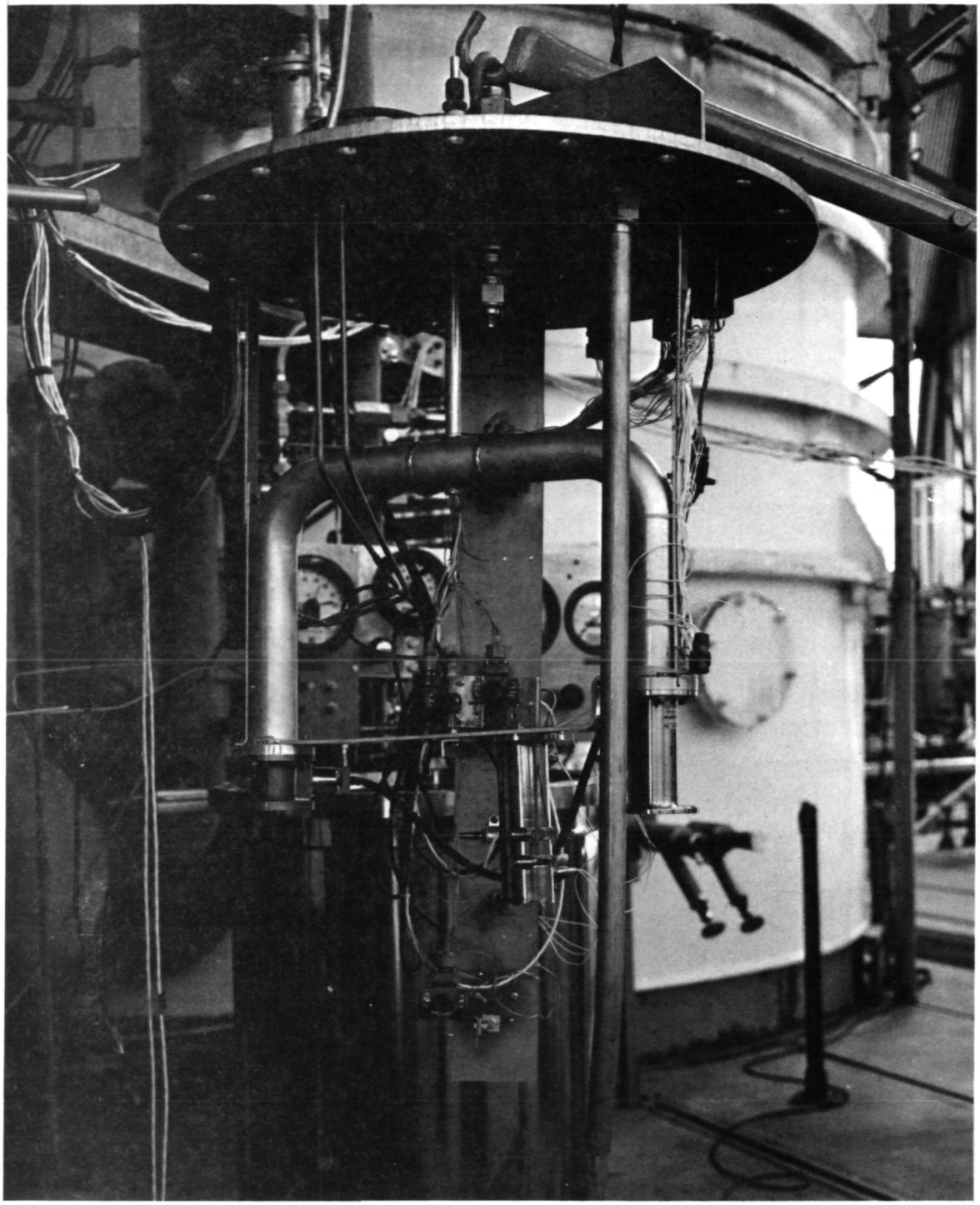


FIG. 2



F-16046

Figure 3.

3.3.3 Hydrogen Slugging Test

This test was performed on June 23, 1969. The test setup was the open loop configuration as described in 3.3.1 above. The test sequence was initiated with the test dewar and system at ambient temperature (approximately 520°R) and containing gaseous hydrogen. Liquid hydrogen was admitted to the test dewar at a slow rate with the test unit off. When the dewar internal temperature reached 100°R, 28 volts DC was applied to the breadboard electronics. When the liquid hydrogen slugging occurred (two phase hydrogen flow) speed oscillated between approximately 3800 and 2400 RPM while motor current oscillated between approximately 0.02 and 0.15 amps. When loop was totally submerged in liquid hydrogen the performance stabilized at a flow rate of 5.4 CFM, speed of 2300 RPM and motor current of 0.09 amps. Complete stabilized performance at end of slugging test is presented in the appendix. No adverse effects to unit's performance was observed as a result of the slugging test. Approximately one hour elapsed during the performance of this test.

3.3.4 Endurance

This test was performed with the unit installed in the test setup as described in above paragraph 3.3.1. The loop was totally submerged in liquid hydrogen for the complete endurance test phase. Data was teken periodically during this testing and is presented in the appendix.

A summary of endurance operating time of unit in various configurations is listed below;

- o 1.0 hour - Gaseous hydrogen calibration
- o 2.0 hours- Liquid hydrogen calibration
- o 85 hours - Liquid hydrogen with cycle timer and slugging (4 min. on and 2 min. off)
- o 12 hours - Gaseous helium

- o 100 hours - Total operating time

3.3.5 Calibration in Gaseous Helium

The lower half of the flow loop was installed in the test setup resulting in a test configuration as shown in the schematic of Figure 4 and photograph of Figure 5. Prior to test, the loop internal system and dewar internal system were evacuated to 10 microns pressure and held for a minimum of 15 minutes in order to accomplish drying of systems. The closed loop was then re-pressurized to approximately 16 psia with helium and maintained at a positive differential above the test dewar pressure throughout this test phase. The test dewar was filled with liquid hydrogen to a level that totally submerged the loop and maintained in this condition throughout test. When helium loop temperature stabilized at 37°R the unit was energized by application of 28 volts to the electronic breadboard. Performance data was obtained at flow rates from 7.0 CFM to 3.4 CFM by adjustment of the loop throttling valve. Complete performance data is presented in the appendix. Upon completion of the helium calibration test the unit was operated in this configuration to obtain the total 100 hours operating time. This series completed the testing activity performed by LMSC on this unit.

Prepared	NAME	DATE	LOCKHEED MISSILES & SPACE COMPANY A GROUP DIVISION OF LOCKHEED AIRCRAFT CORPORATION	Page	TEMP	PLAN
Checked			TITLE	Model		
Approved			GHe Test Setup	Report No.		

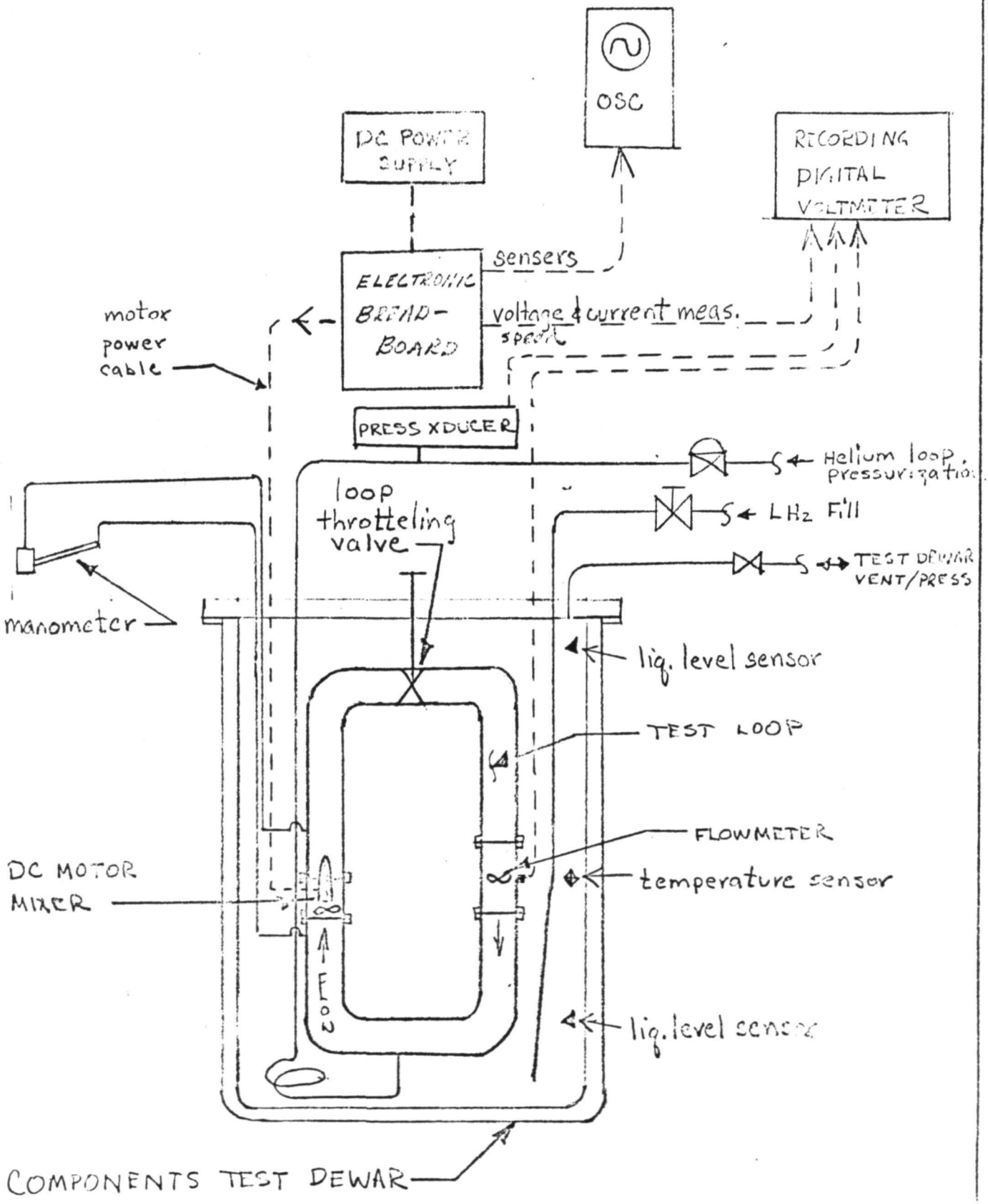
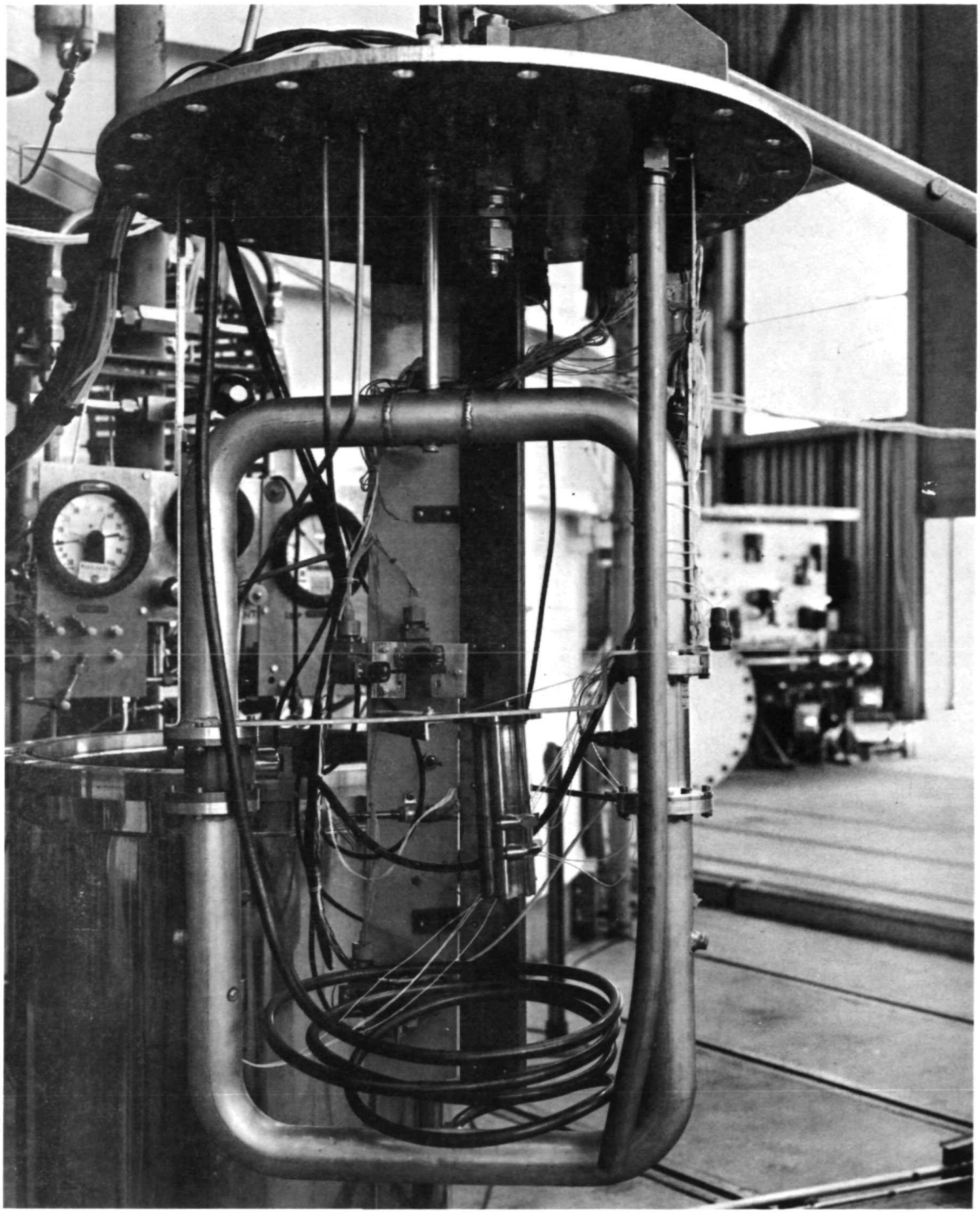


FIG. 4



F-16047

Figure 5.

4.0 Appendix

- Test Data
- Oscilloscope Traces

DC MIXER TEST DATA pg 1 of 3

TEST DIRECTOR: L. Sh...

Test Title	Date	Accum Run Time	Test Fluid	Speed RPM	Flow CFM	Head inch H_2O	Applied Volts	Motor Volts	Applied Amps	Motor Amps	Fluid Temp °R	Inlet Press psia
Calibration	6-18-69	1 hr	GH_2	3990	8.00	0.070	29.4	28.3	0.071	0.015	41	14
↓	↓	↓	↓	3910	6.82	0.085	29.4	28.4	0.071	0.015	42	↓
↓	↓	↓	↓	3920	4.91	0.070	29.4	28.4	0.070	0.014	43	↓
↓	↓	↓	↓	3930	3.41	0.090	29.3	28.5	0.069	0.013	44	↓
↓	↓	↓	↓	3925	6.22	0.020	29.4	28.4	0.071	0.014	45	↓
Calibration	6-18-69	3 hr	LH_2	2590	6.02	1.11	28.6	20.7	0.173	0.116	38	14
↓	↓	↓	↓	2550	5.45	1.67	28.6	20.6	0.178	0.119	38	↓
↓	↓	↓	↓	2580	4.65	2.22	28.7	20.6	0.177	0.121	38	↓
↓	↓	↓	↓	2640	3.55	2.67	28.6	21.1	0.170	0.114	38	↓
↓	↓	↓	↓	2790	2.60	2.03	28.7	21.9	0.156	0.101	38	↓
Endurance	6-19-69	10	LH_2	2250	5.4	1.5	28.1	17.5	0.150	0.094	38	14
↓	6-19-69	15.5	↓	2300	↓	↓	28.1	17.9	0.146	0.091	↓	↓
↓	6-20-69	18.1	↓	2240	↓	↓	28.2	17.5	0.149	0.093	↓	↓
↓	6-20-69	23	↓	2230	↓	↓	28.2	17.4	0.149	0.094	↓	↓
END OF [illegible] Test	6-23-69	25	↓	2280	↓	↓	28.3	17.7	0.148	0.092	↓	↓
Endurance	6-24-69	28.5	↓	2220	↓	↓	28.3	17.7	0.148	0.093	↓	↓
↓	6-24-69	34	↓	2270	↓	↓	28.3	17.6	0.148	0.093	↓	↓

DC MIXER TEST DATA pg 2 of 3

TEST TITLE	DATE	Accum. RUN TIME	TEST FLUID	SPEED RPM	FLOW CFM	head inch H2O	Applied Volts	Motor Volts	Applied Amps	Motor Amps	Fluid TEMP. °R	Inlet press. PSIA
MIL-[illegible]	6-25-69	37	Lliz.	2270	5.4	1.5	28.4	17.6	0.149	0.093	38	14
	6-25-69	44		2270			28.4	17.6	0.149	0.093		
	6-26-69	46		2260			28.2	17.5	0.148	0.092		
	6-26-69	51		2260			28.2	17.5	0.148	0.093		
	6-27-69	56		2260			28.3	17.5	0.148	0.093		
	6-30-9	61		2270			28.3	17.7	0.147	0.092		
	6-30-9	68		2270			28.3	17.7	0.147	0.092		
	7-1-9	72		2250			28.2	17.5	0.148	0.092		
	7-1-9	77		2260			28.2	17.6	0.148	0.092		
	7-2-9	78		2250			28.2	17.6	0.149	0.092		
	7-2-9	84		2250			28.2	17.5	0.148	0.092		
	7-3-9	88		2250			28.2	17.5	0.148	0.092		

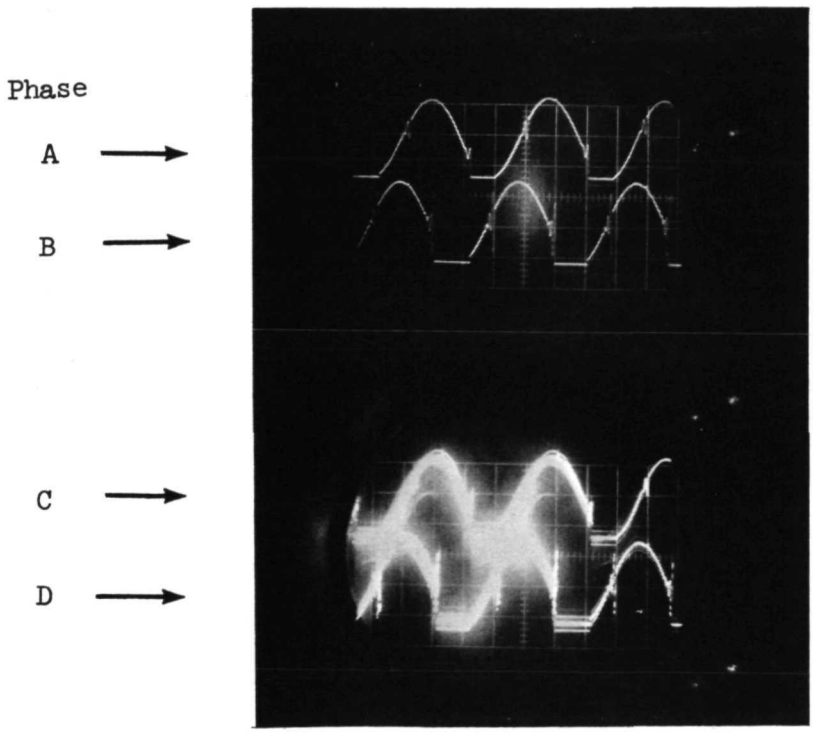
13

DC MIXER TEST DATA pg 3 of 3

TEST TITLE	DATE	ACCUM RUN TIME	TEST FLUID	SPEED RPM	FLOW CFM	head in. H_2O	Applied Volts	Motor Volts	Applied Amps	Motor Amps	FLUID TEMP °F	Inlet press psia.
Calibration	7-9-69	88	GHe	3680	7.01	0.105	28.4	26.1	0.075	0.019	37	16
↓	↓	↓	↓	3680	6.70	0.120	28.4	26.1	0.073	0.019	↓	↓
↓	↓	↓	↓	3700	4.91	0.135	28.4	26.3	0.073	0.017	↓	↓
↓	↓	↓	↓	3720	3.42	0.150	28.4	26.4	0.075	0.017	↓	↓
↓	↓	↓	↓	3680	6.01	0.150	28.4	26.2	0.075	0.019	↓	↓
↓	↓	↓	↓	3680	6.40	0.135	28.4	26.2	0.075	0.019	↓	↓
↓	↓	↓	↓	3700	5.31	0.145	28.4	26.2	0.074	0.018	↓	↓
Endurance	7-9-69	88	GHe	3680	7.00	0.105	28.4	26.1	0.075	0.019	37	16
↓	7-9-69	94	↓	3680	↓	↓	28.4	26.1	0.075	0.019	↓	↓
↓	7-10-69	95	↓	3680	↓	↓	28.4	26.2	0.075	0.019	↓	↓
↓	7-10-69	100	↓	3680	↓	↓	28.4	26.1	0.075	0.019	↓	↓

Date: 6-18-69

Pretest Ambient Temperature Checkout

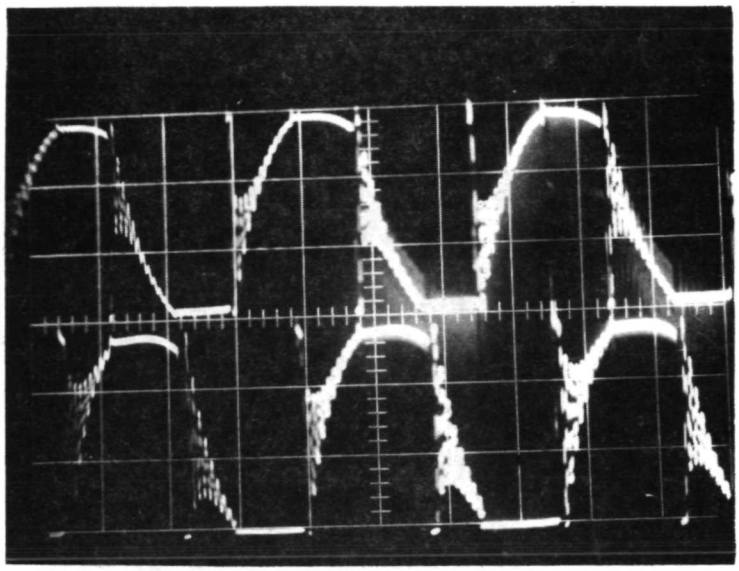


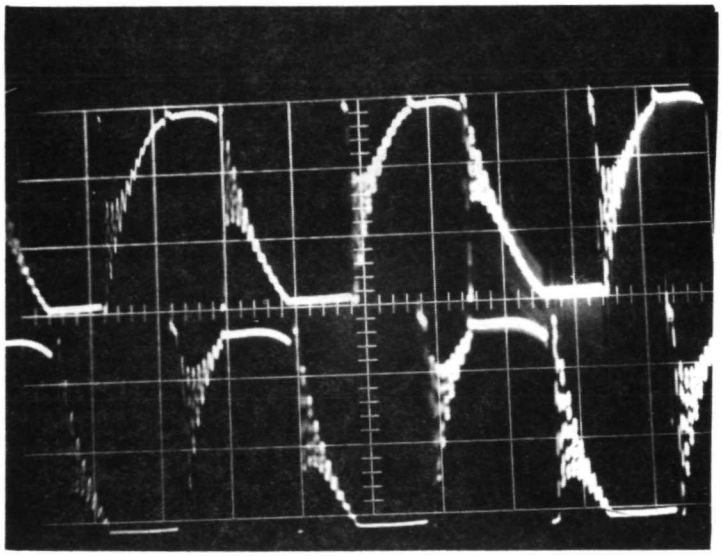
F-16048

Date: 6-18-69 Time of Day: 08:45

Start GH_2 Calib. Run

OSC Range 20 volts/cm

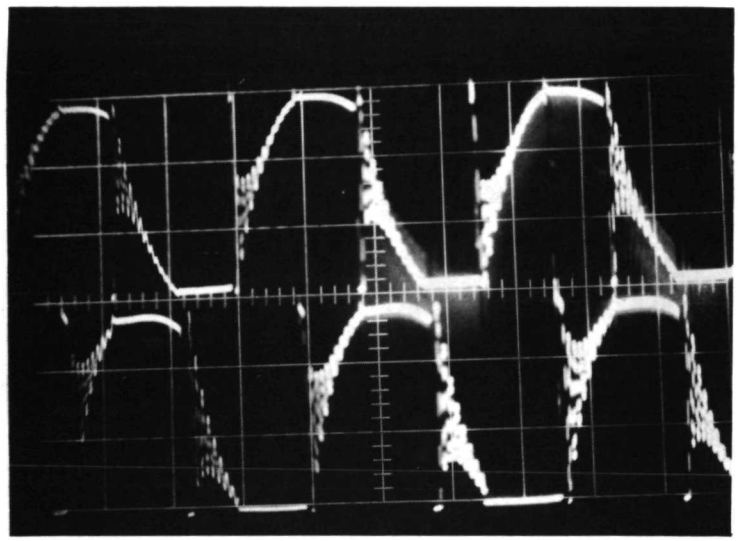


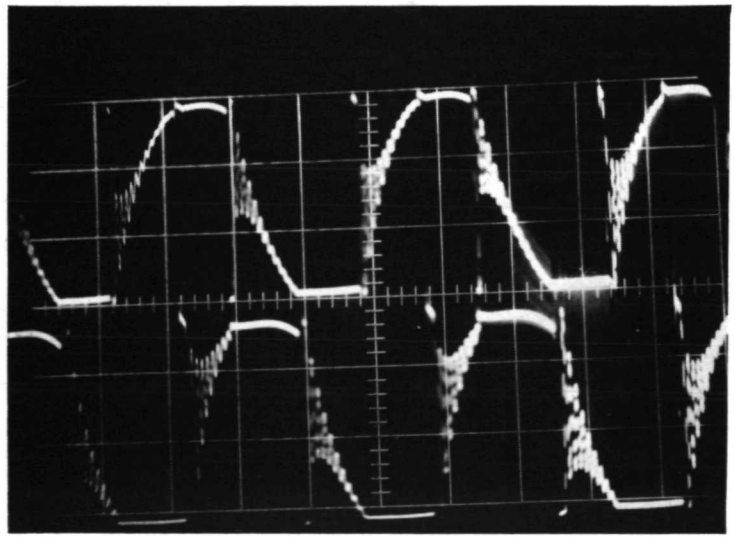


F-16049

Date: 6-18-69 Time of Day: 08:45

Start GH_2 Calibration Run

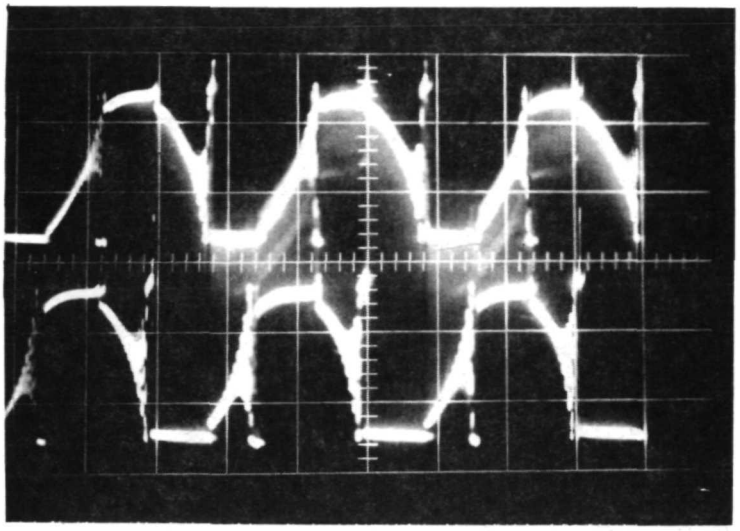


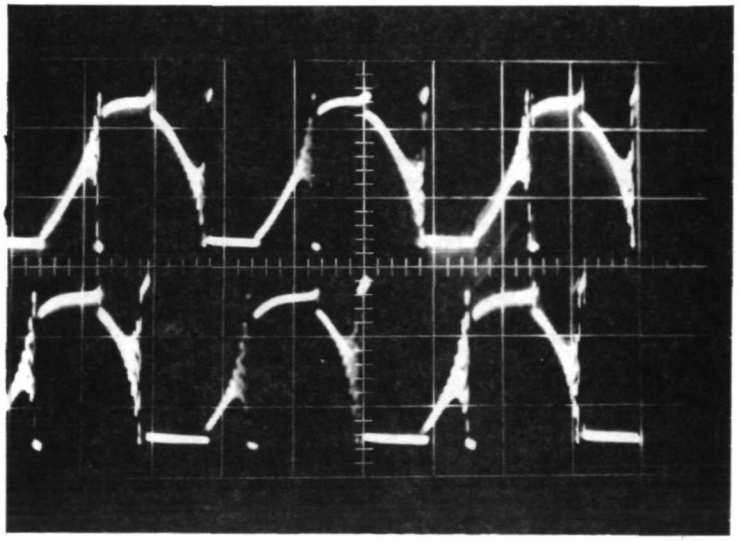


F-16050

Date: 6-18-69 Time of Day: 11:30

Start of LH_2 Calibration Run

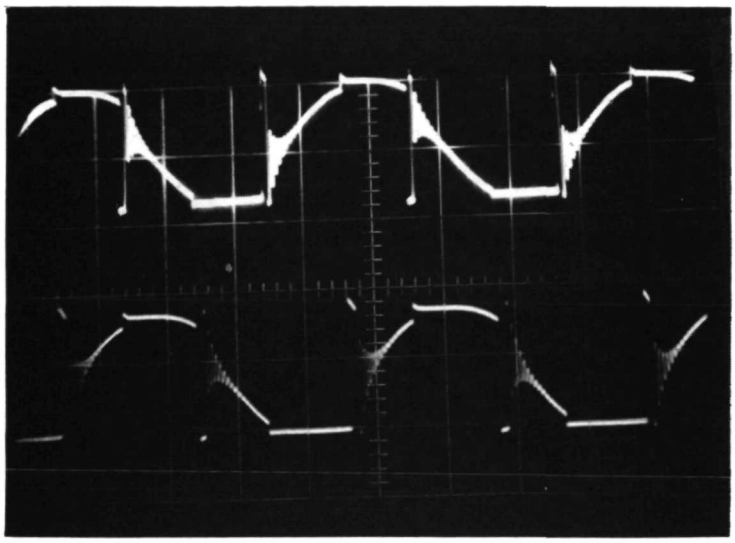


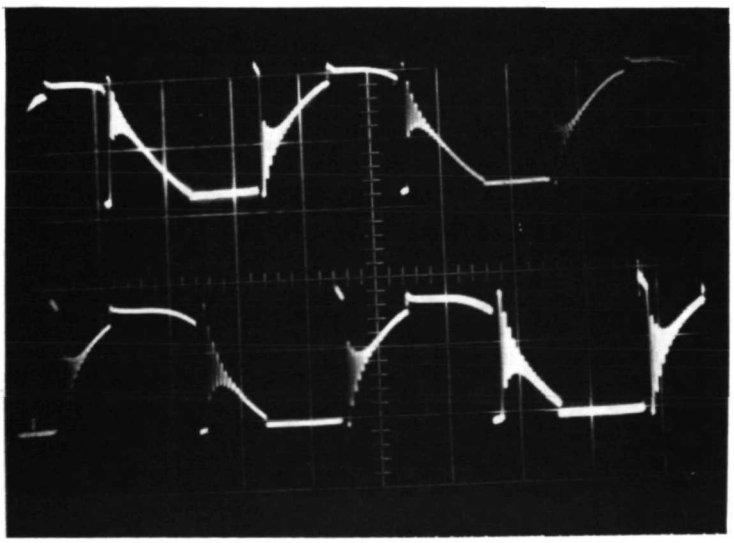


F-16051

Date: 6-19-69 Time of Day: 09:30

Endurance

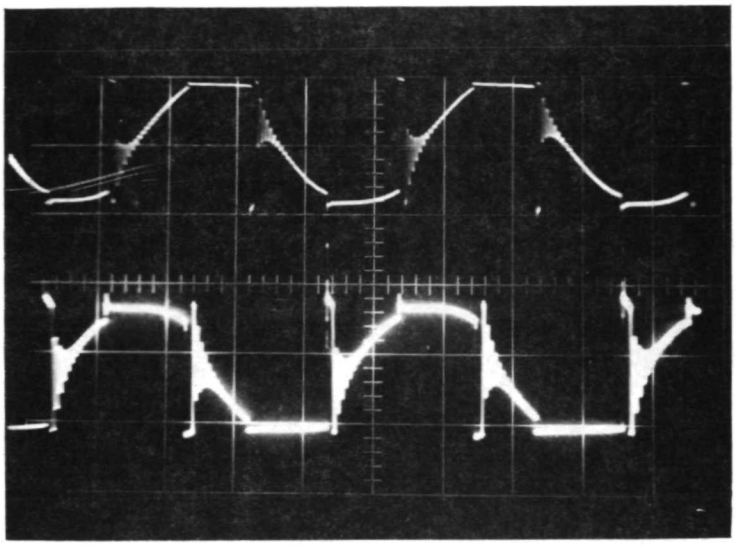


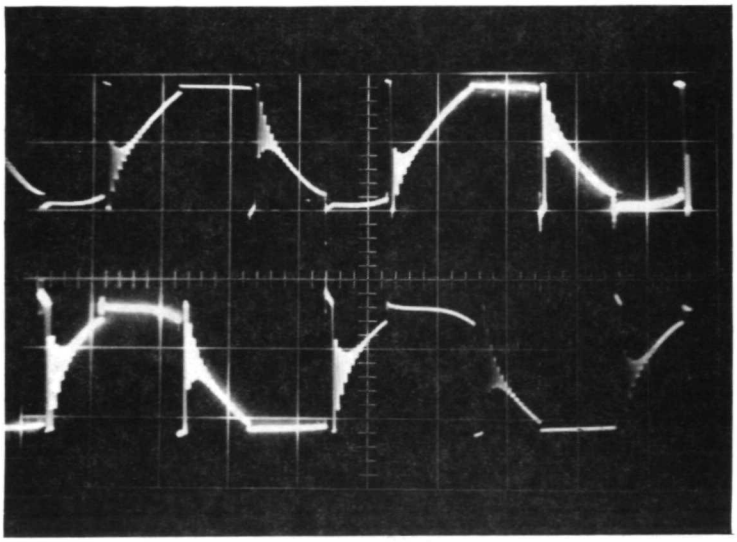


F-16052

Date: 6-19-69 Time of Day: 15:00

Endurance

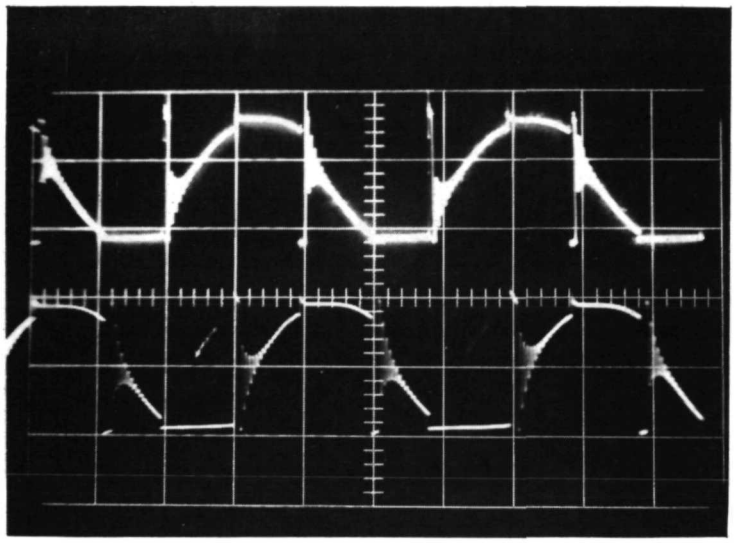


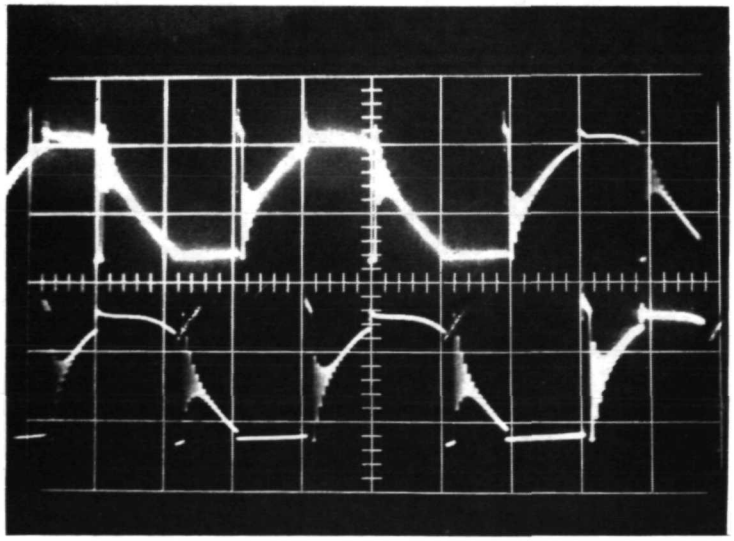


F-16053

Date: 6-20-69 Time of Day: 09:30

Endurance



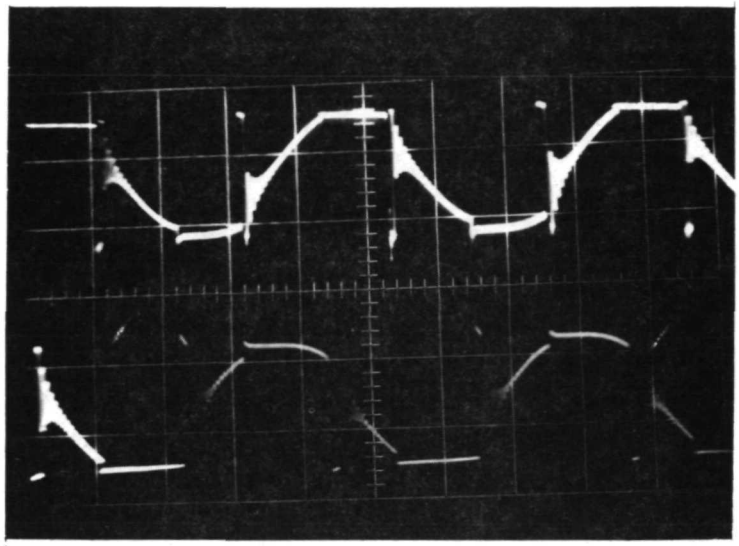


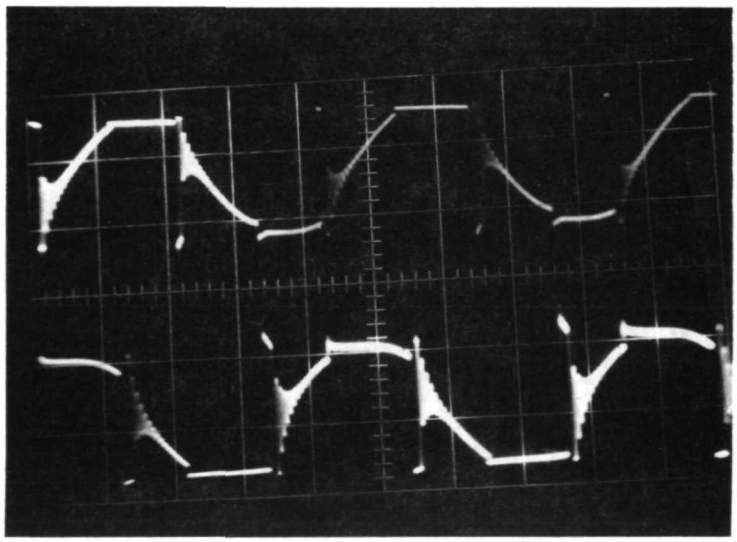
F-16054

Date: 6-20-69

Time of Day: 14:30

Endurance

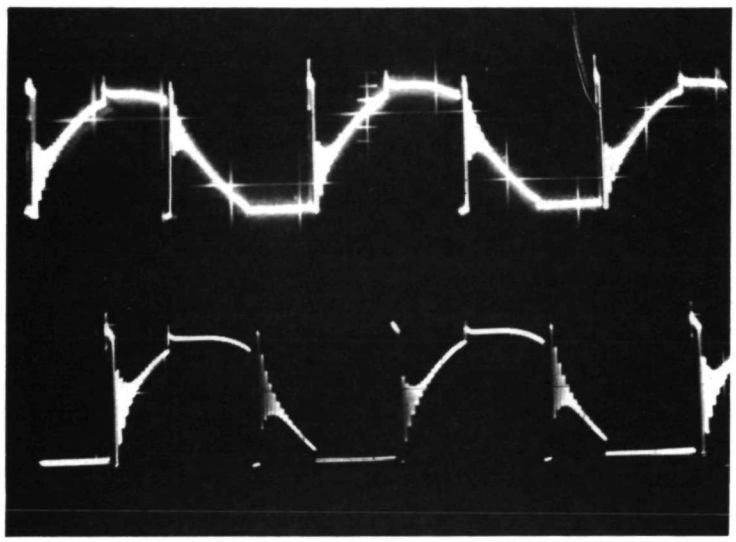


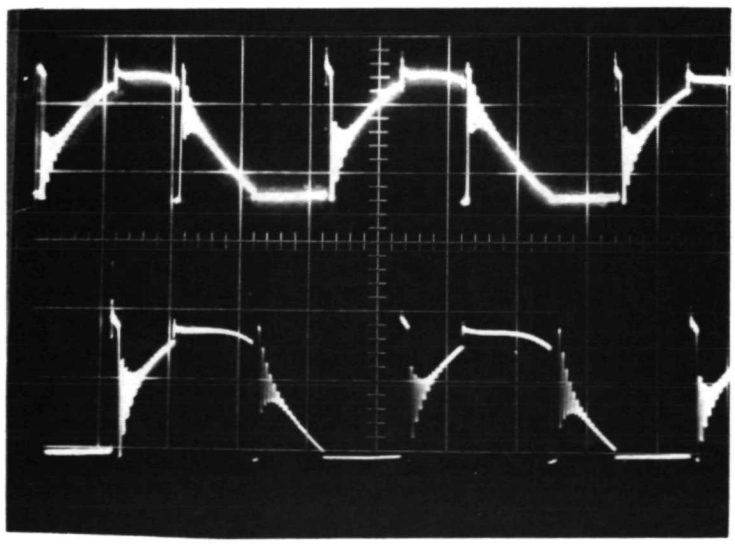


F-16055

Date: 6-23-69 Time of Day: 15:15

Endurance

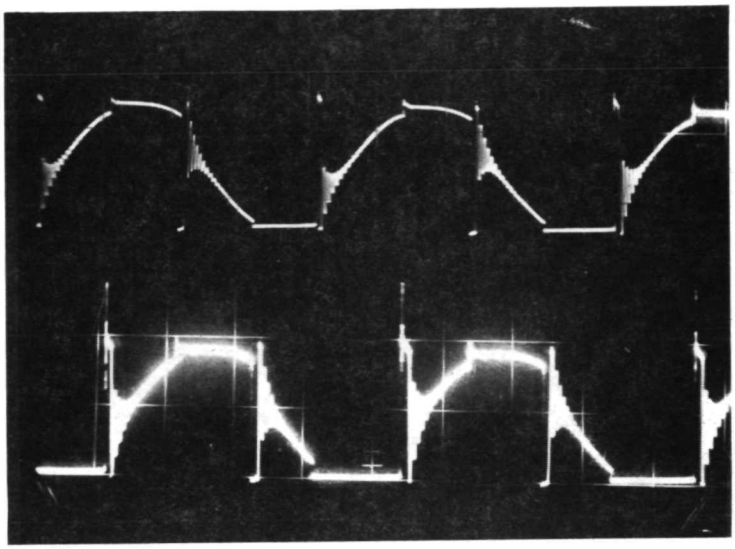


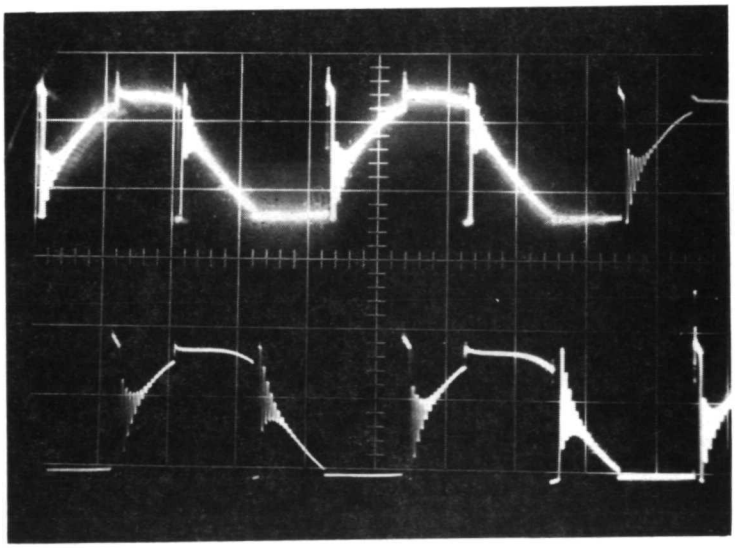


F-16056

Date: 6-23-69 Time of Day: 15:45

Endurance

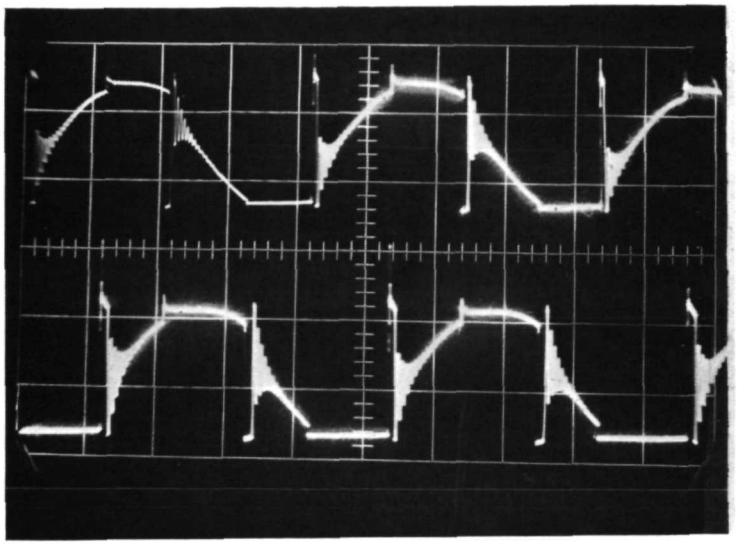


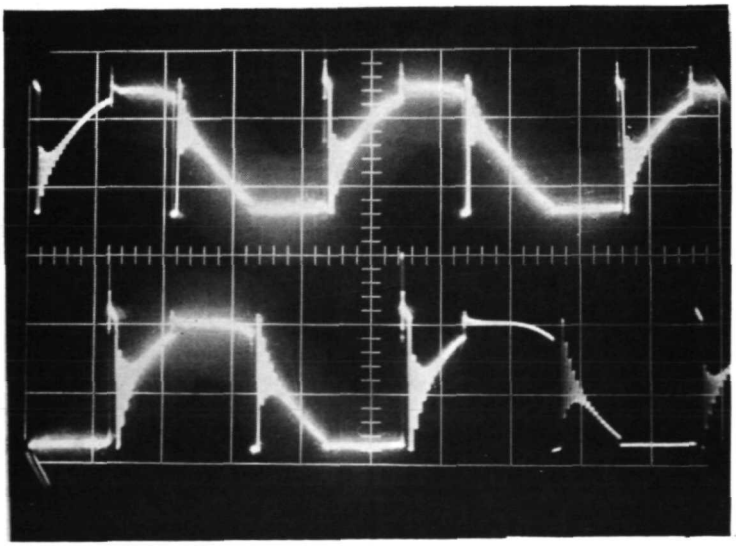


F-16057

Date: 6-24-69 Time of Day: 09:00

Endurance



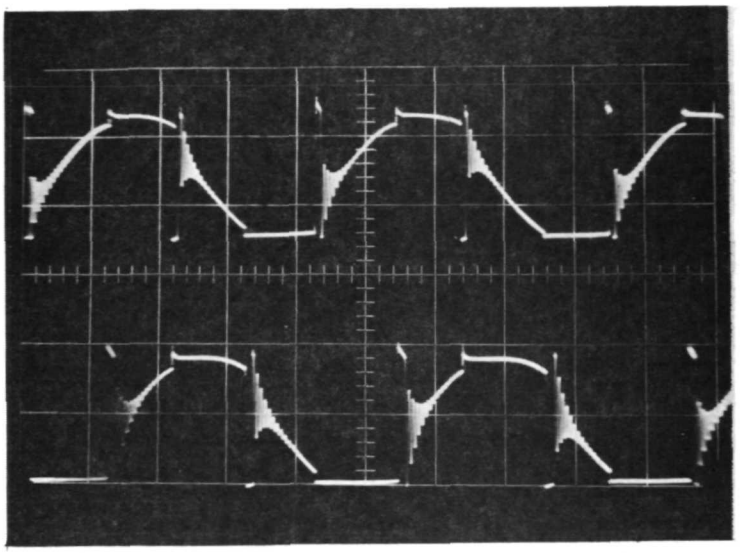


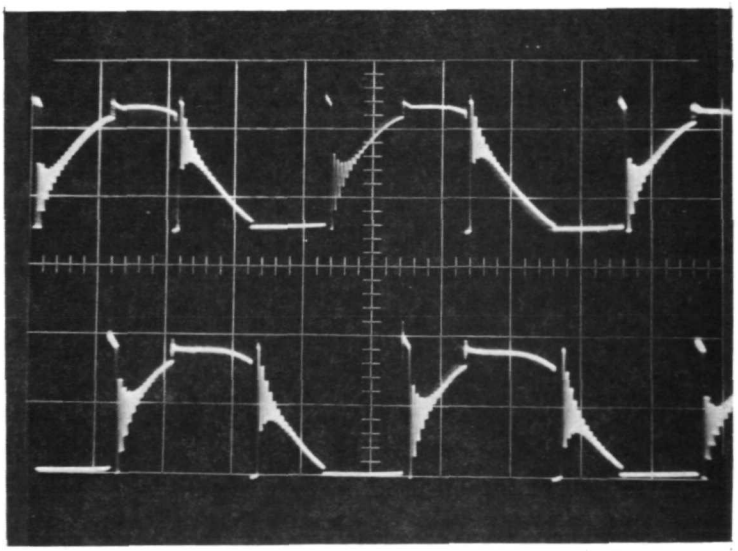
F-16058

Date: 6-24-69

Time of Day: 13:00

Endurance



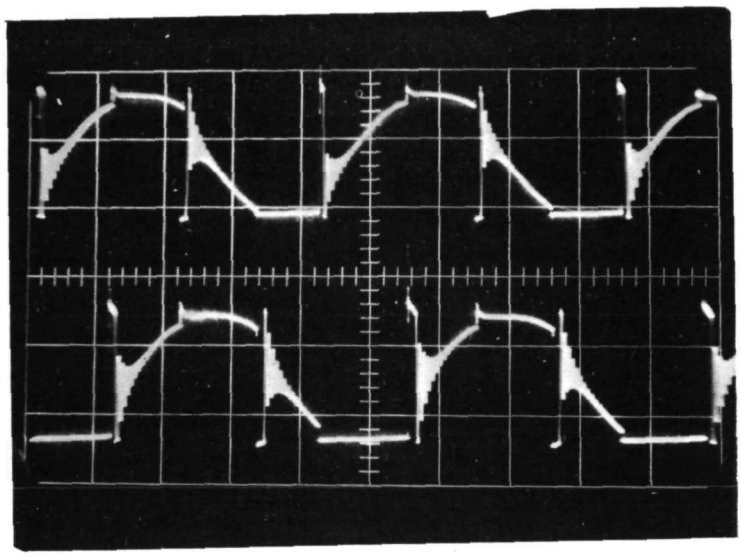


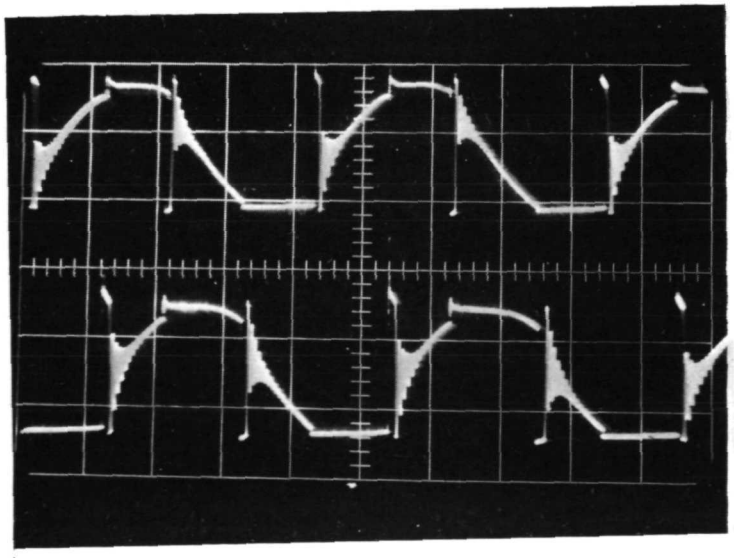
F-16059

Date 6-25-69

Time of Day: 08:30

Endurance



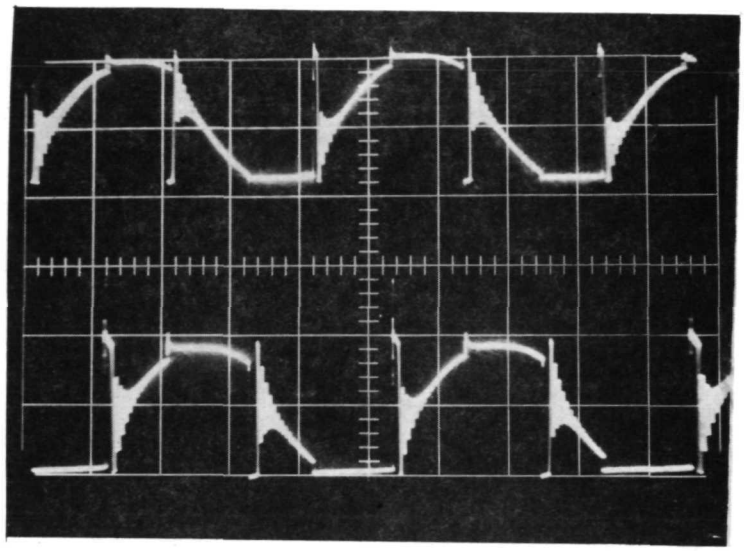


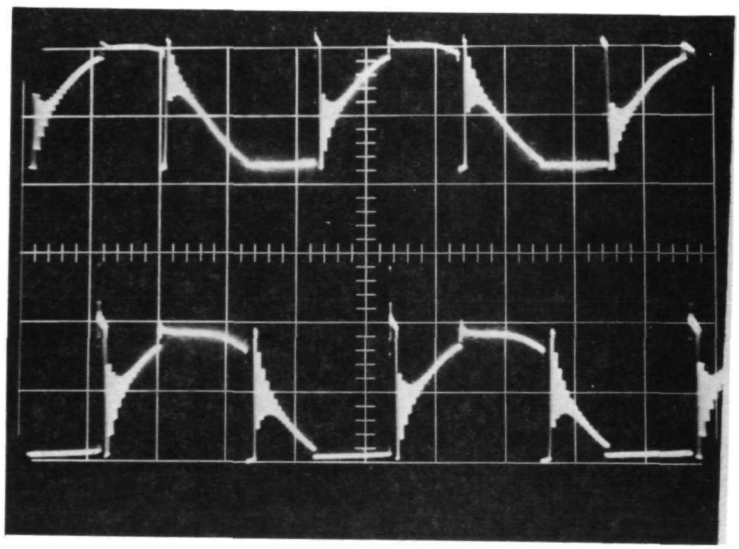
F-16060

Date: 6-25-69

Time of Day: 15:30

Endurance

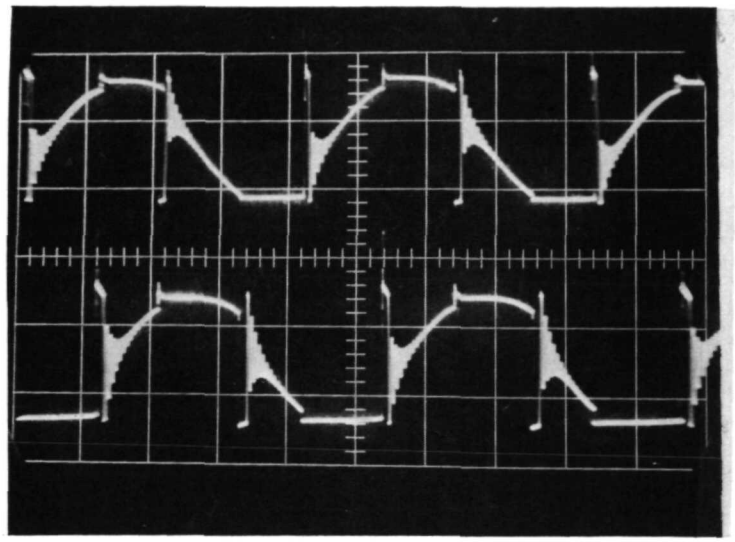


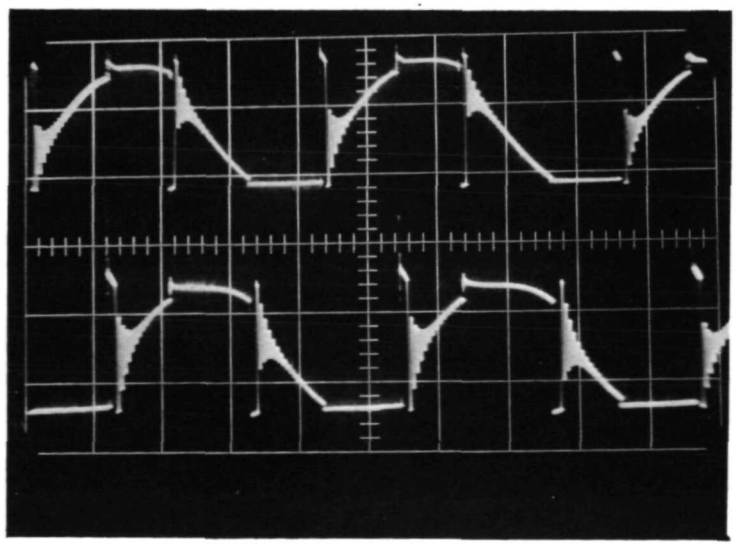


F-16061

Date: 6-26-69 Time of Day: 09:30

Endurance

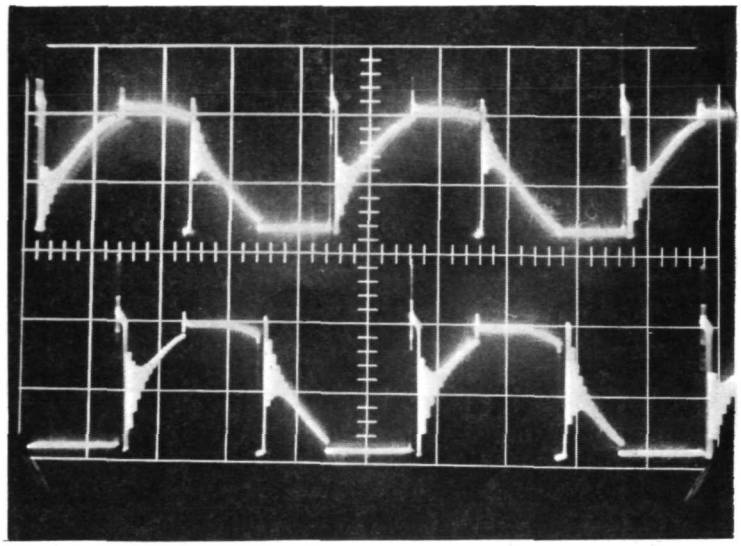


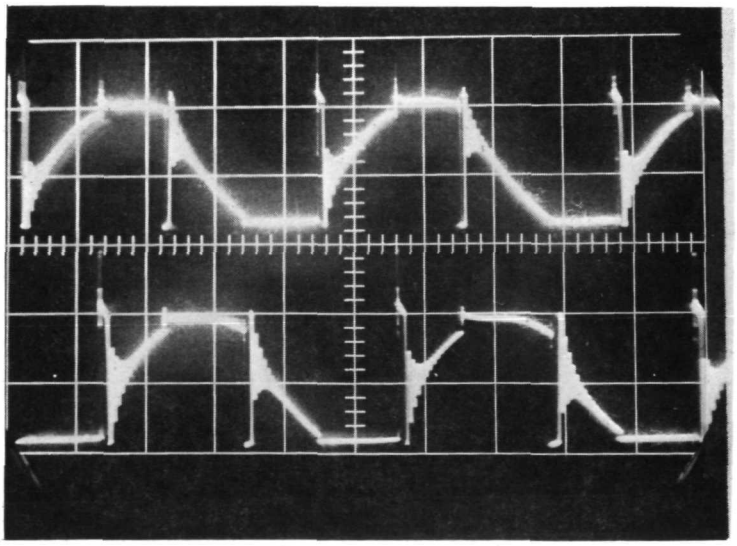


F-16062

Date: 6-26-69 Time of Day: 14:30

Endurance

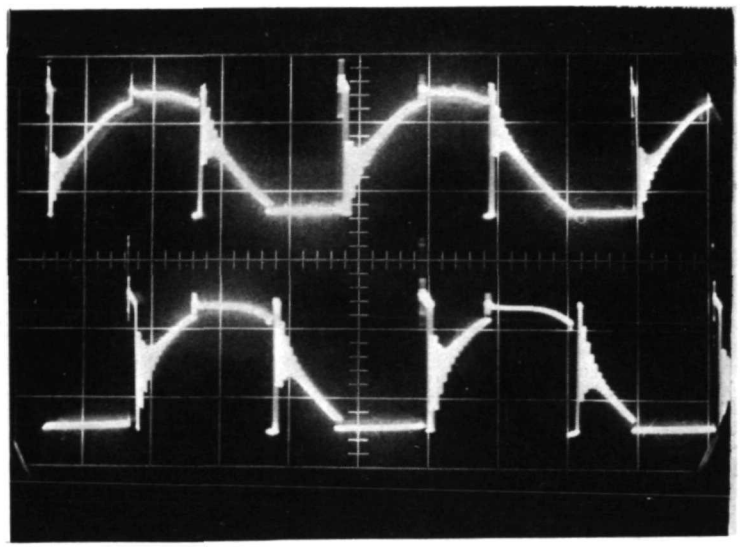


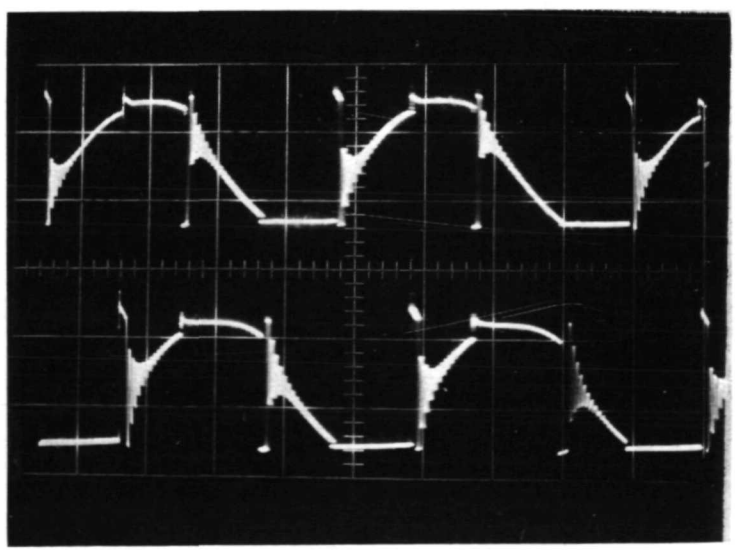


F-16063

Date: 6-27-69 Time of Day: 10:00

Endurance

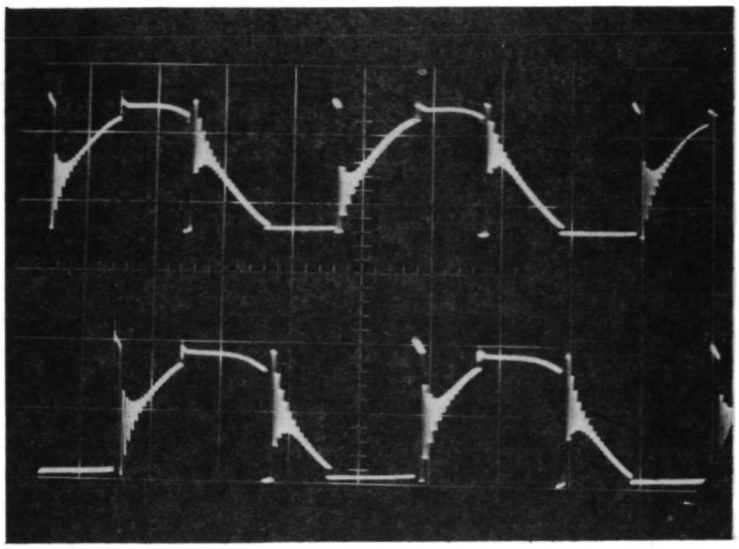


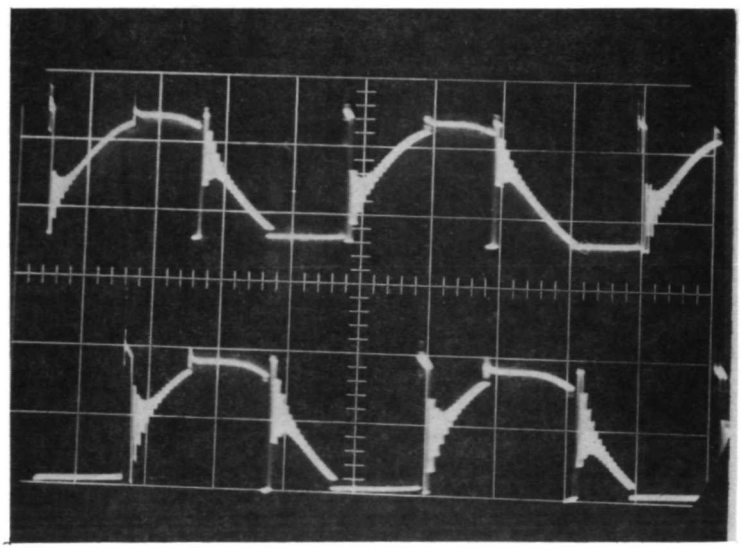


F-16064

Date: 6-27-69 Time of Day: 15:15

Endurance

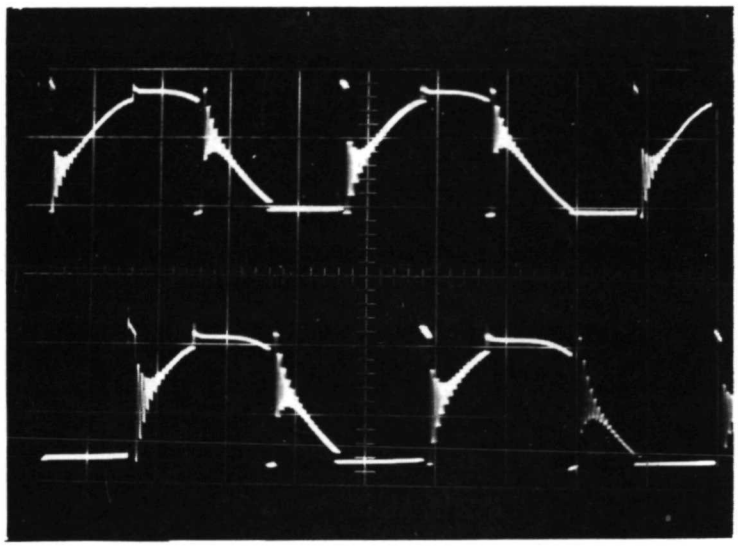


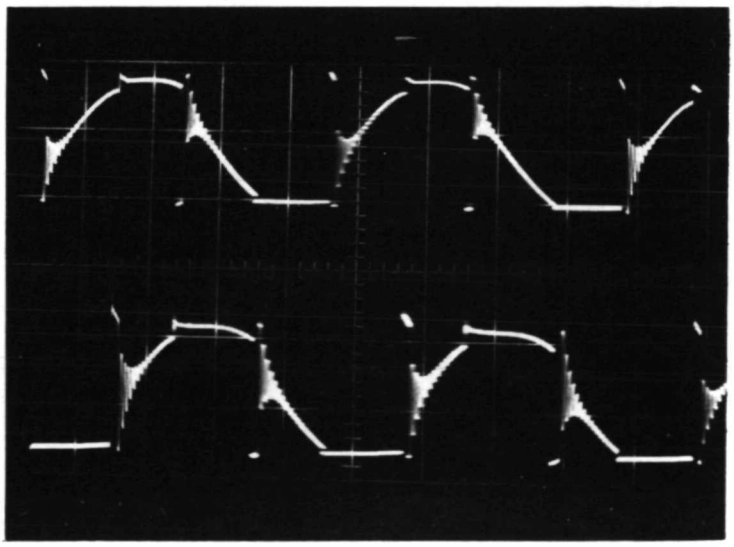


F-16065

Date: 6-30-69 Time of Day: 09:00

Endurance

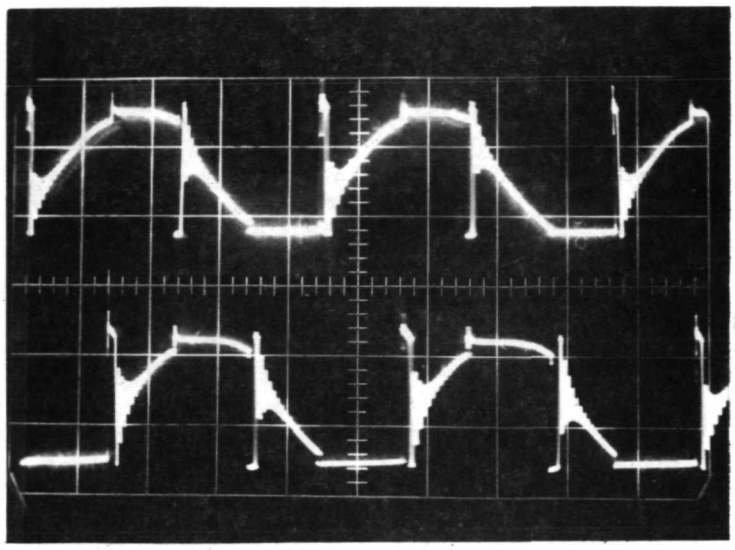


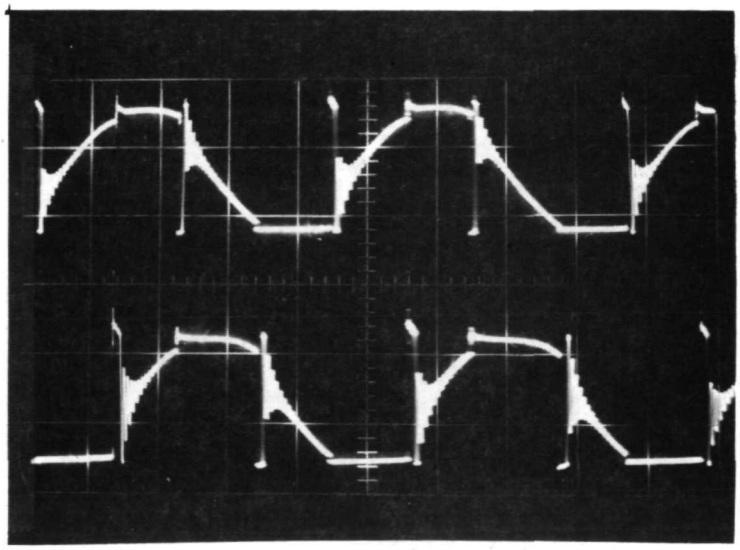


F-16066

Date: 6-30-69 Time of Day: 15:30

Endurance

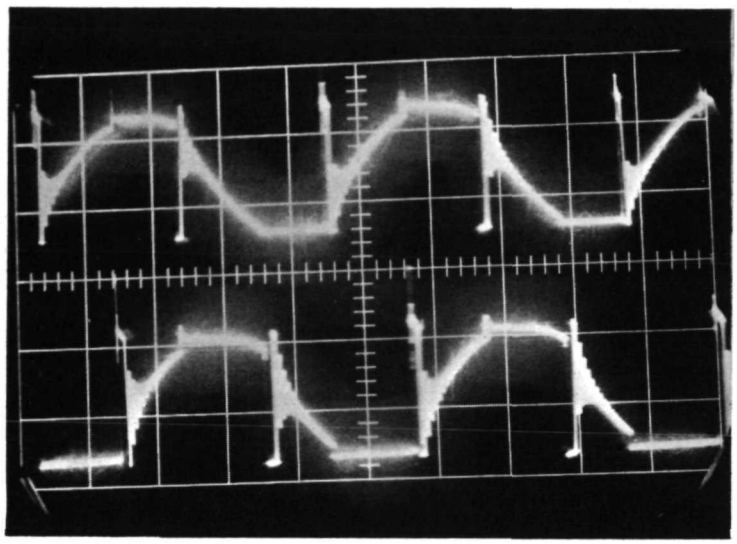


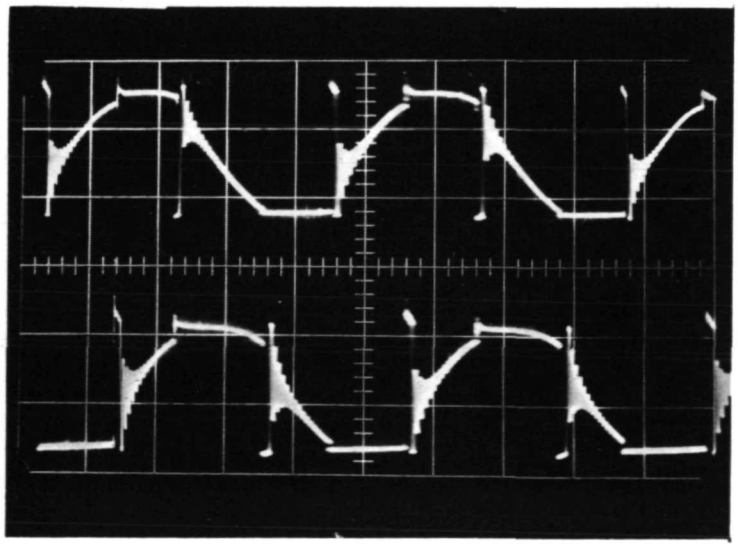


F-16067

Date: 7-1-69 Time of Day: 10:00

Endurance

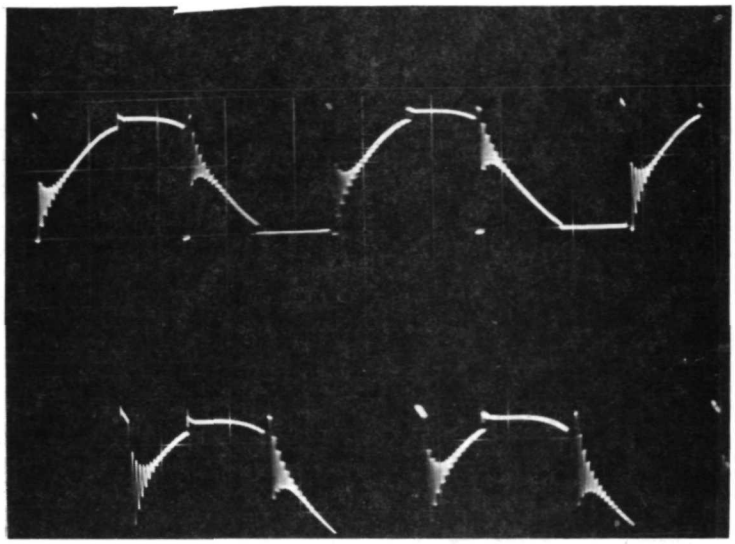


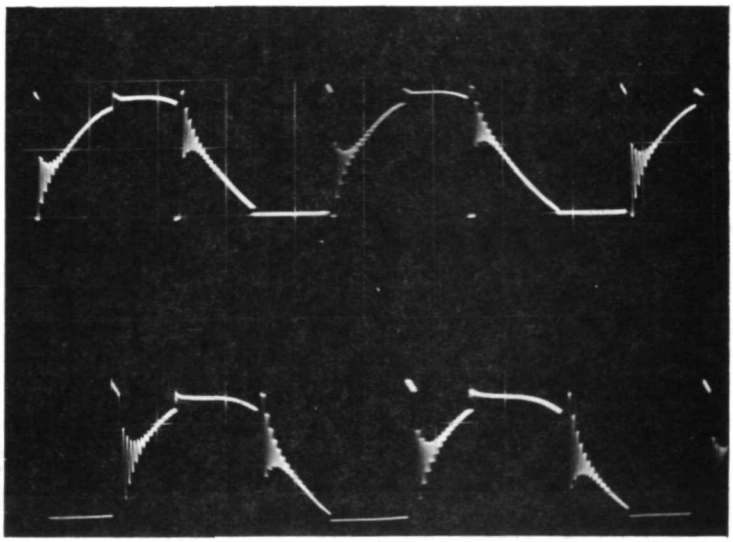


F-16068

Date: 7-2-69 Time of Day: 10:00

Endurance

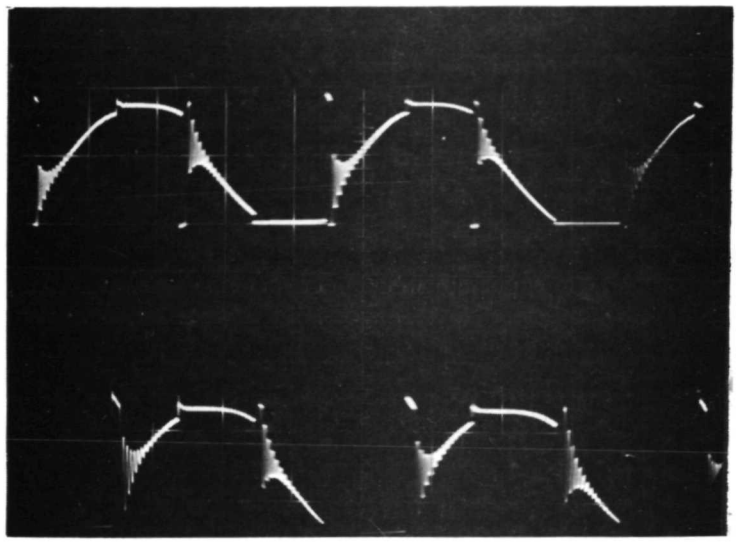


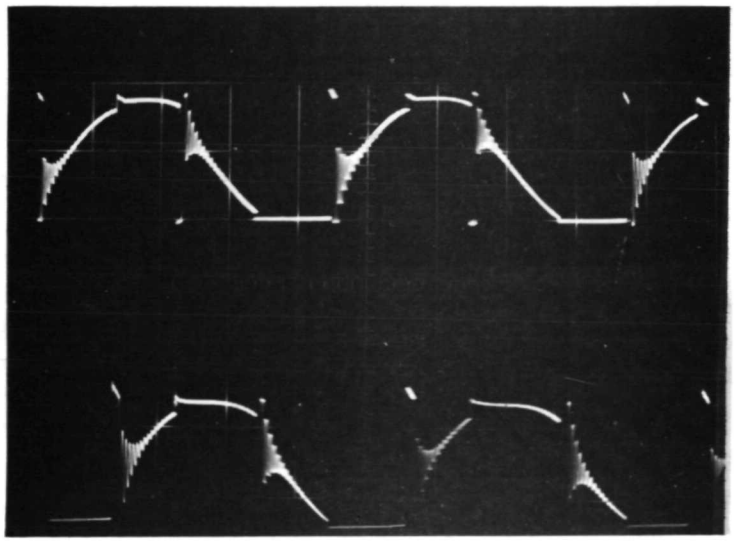


F-16069

Date: 7-2-69 Time of Day: 14:00

Endurance

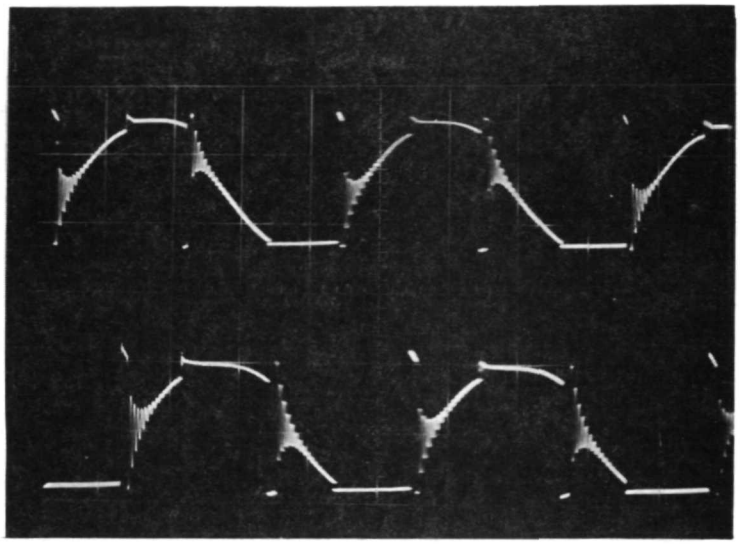


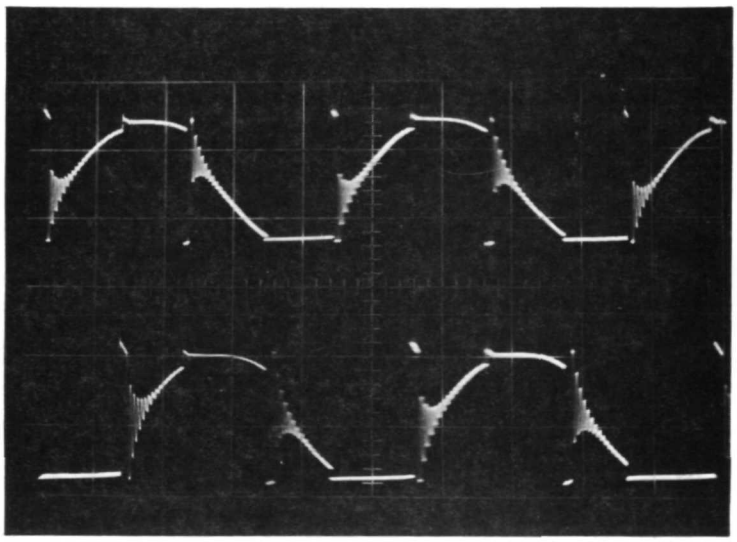


F-16070

Date: 7-3-69 Time of Day: 09:00

Endurance

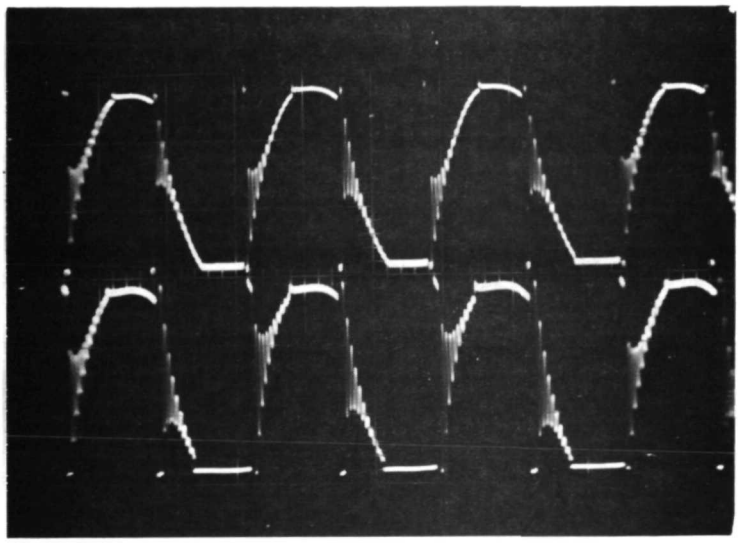


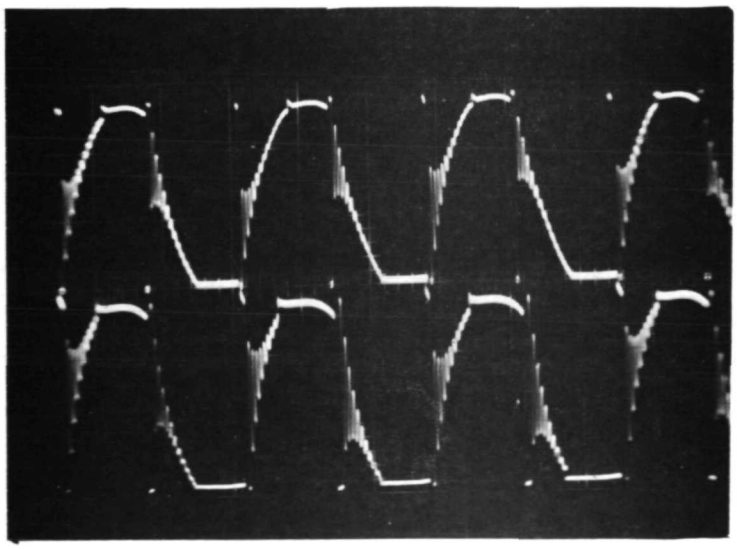


F-16071

Date: 7-9-69 Time of Day: 09:30

Start Helium Calibration



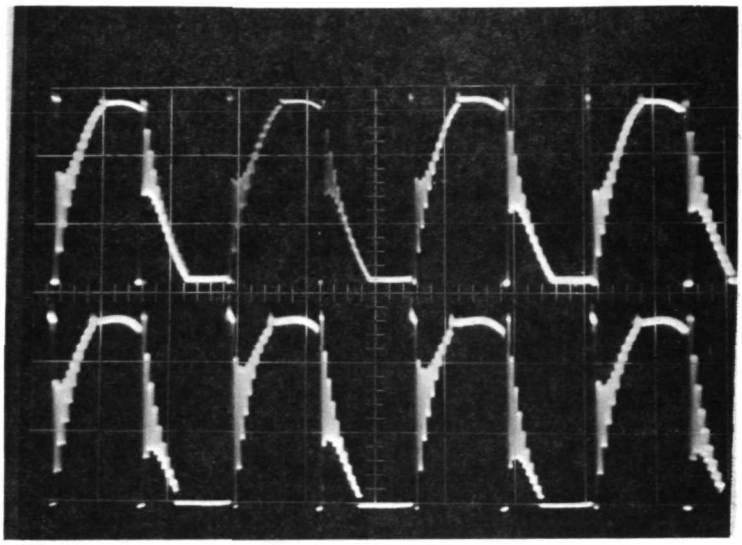


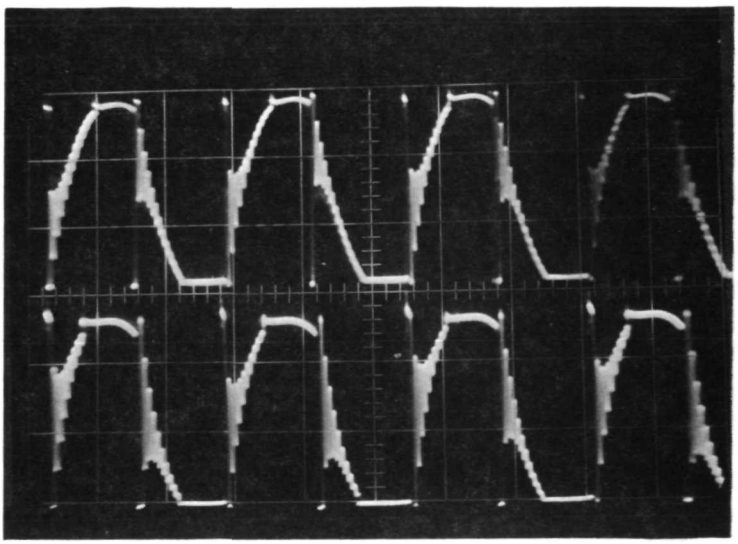
F-16072

Date: 7-9-69

Time of Day: 15:00

Endurance (Helium)

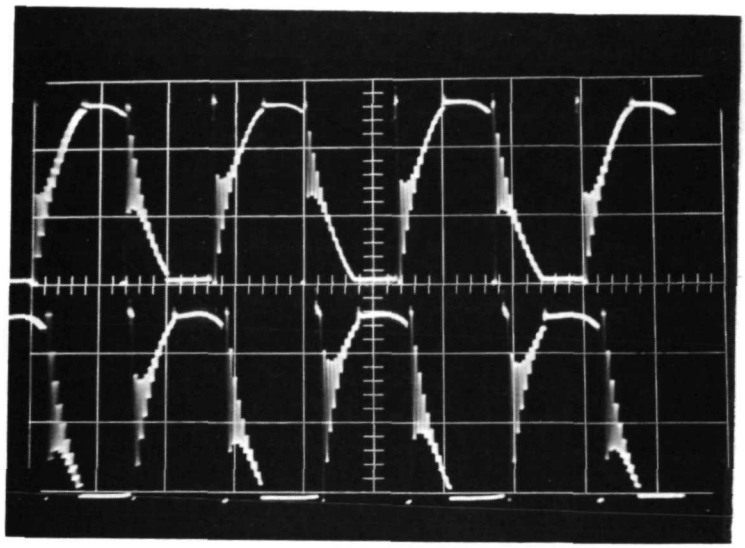


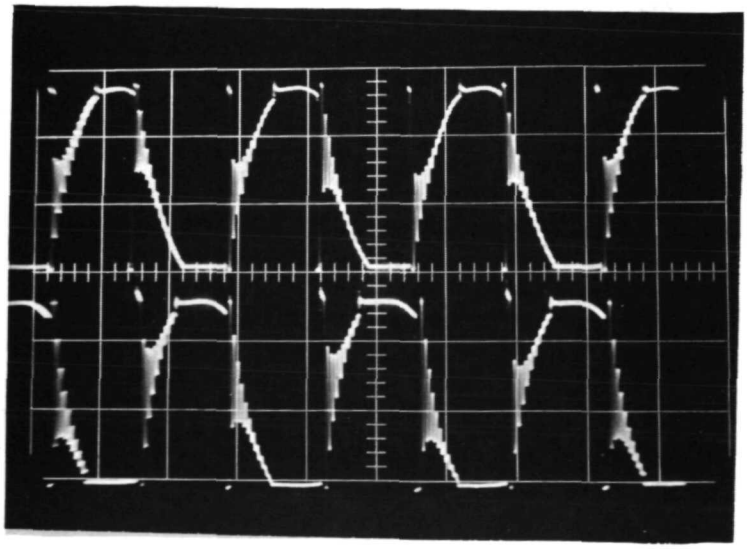


F-16073

Date: 7-10-69 Time of Day: 08:30

Endurance (Helium)

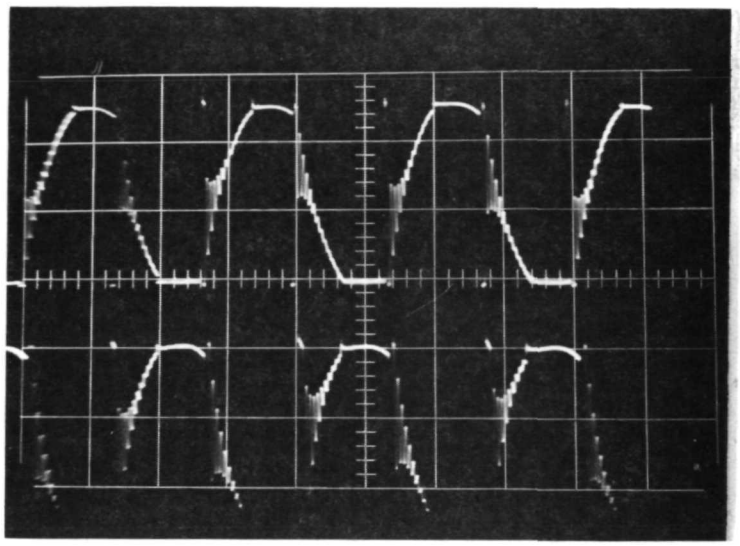


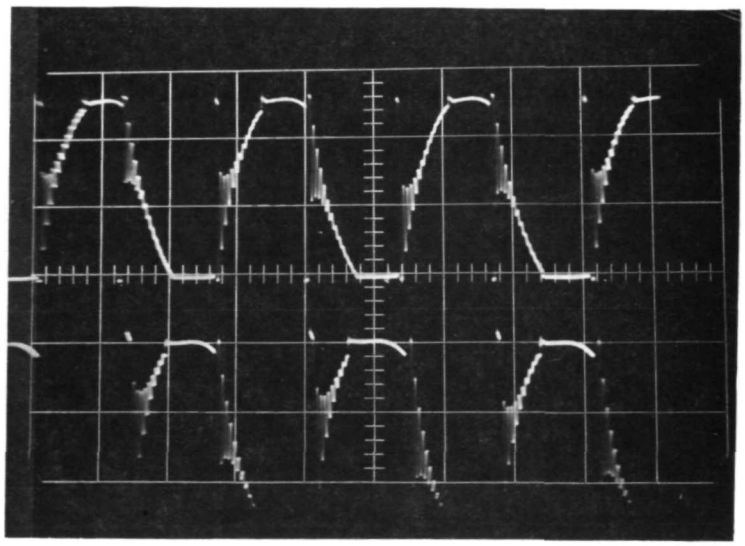


F-16074

Date: 7-10-69 Time of Day: 14:00

Endurance (Helium)





F-16075

APPENDIX B

AIRESEARCH REPORT

EVALUATION AND DEMONSTRATION TEST PROCEDURE CRYOGENIC MIXER PN 605632-1

Report No. 68-4223, Rev 2
(18 pages)

June 12 1972

AIRESEARCH MANUFACTURING DIVISION
Los Angeles, California

EVALUATION AND DEMONSTRATION TEST PROCEDURE AIRESEARCH CRYOGENIC MIXER P/N 605632-1-1

Report No. 68-4223, Rev. 2 June 12, 1972

This document is the property of The Garrett Corporation. It is furnished to inform Buyer of the status of Seller's performance and is not to be duplicated, used, or disclosed for any other purpose without the prior written permission of The Garrett Corporation.

Revised by M. W. Meister (6-12-72)

Orig. Date August 29, 1968

Prepared by R. Rudich R. Morgan

Approved V. A. Vilona
V. A. Vilona

REVISIONS					
Rev. No.	**Date**	**Rev. & New Pages**	**Rev. No.**	**Date**	**Rev. & New Pages**
1	1-10-69	Complete			
2	6-12-72	4-1, 4-2, 4-3, 4-4, 4-5, 4-6, 4-11			

AIRESEARCH MANUFACTURING COMPANY

A DIVISION OF THE GARRETT CORPORATION

LOS ANGELES, CALIFORNIA

DOCUMENT CHANGE NOTICE

DCN NO. - DOC REV 2

DOC NO. 68-4223

PAGE ____ OF ____

DATE 6-5-72

SUPERSEDING DCN NO.

ECP NO.	CONTRACT NO. AND AUTHORITY
None	N/A
EFFECTIVITY	END ITEM NO.
-	605632-1-1

DISPOSITION INSTRUCTION

- [ ] ERRATA SHEET (PARTIAL DOCUMENT). { [ ] FILE OPPOSITE PAGE AFFECTED. [ ] FILE AFTER TITLE PAGE.
- [ ] CHANGED PAGE(S) (PARTIAL DOCUMENT). REPLACE PAGE(S) AFFECTED.
- [ ] SUPPLEMENT OR ADDENDUM. ADD TO EXISTING DOCUMENT.
- [X] COMPLETE DOCUMENT. REPLACE PREVIOUS ISSUE.

- [ ] ADVANCE
- [ ] PROPOSED
- [X] APPROVED

DESCRIPTION OF CHANGE(S)

1. Revised title page to reflect latest revision.
2. Page 4-1, Para. 4.2.1, 2nd para. line 8 word "it" was "this".
3. Page 4-2, Para. 4.2.2, 3rd para. first two sentences were one, subscript for R was S (thus R_E was R_S).
4. Page 4-3, Para. 4.2.3, 3rd para. added last phrase.
5. Page 4-4, last para. line 4 added plural to Zener.
6. Page 4-5, completely revised.
7. Page 4-6, 1st para. subscript R_E was R_S.
8. Page 4-11, upper left area, R_E was R_S.

PREPARED BY / DATE	CHECKED BY / DATE	APPROVED BY / DATE	CONFIG. CONTROL / DATE
N. Meister 6/5/72		[illegible] 6/13/72	

I. INTRODUCTION

This procedure presents a description of the proposed evaluation and demonstration testing of a brushless dc motor driven liquid hydrogen mixer unit, Part No. 605632-1-1. The mixer unit is designed to demonstrate the feasibility of this type equipment for cryogenic tanks used in space flight as set forth in Exhibit A of NASA Contract NAS3-11208.

The tests described in this procedure will be a demonstration that the unit will operate with liquid hydrogen, gaseous hydrogen and gaseous helium at liquid hydrogen temperatures. The tests described will also demonstrate operation with a slugging flow consisting of mixtures of liquid and gaseous hydrogen.

These tests are designed to measure the motor and hydrodynamic efficiencies separately. In order to accomplish this, a procedure is presented which permits an aerodynamic calibration in high density air to be related to liquid hydrogen by the laws of dynamic similarity. Liquid nitrogen and liquid helium tests will also be conducted to predict certain electronic losses at liquid hydrogen temperatures.

2. TEST FACILITIES

2.1 TEST LOCATION

All testing specified herein calling for a temperature of $37^{0}R$ will be performed at Lockheed Missiles and Space Company, Santa Cruz Test Base. All other tests will be performed at the AiResearch Test Laboratory, Los Angeles, California.

2.2 TEST EQUIPMENT

The following test equipment or equivalent may be utilized:

2.2.1 Dewar, Vacuum, Jacketed, 22 x 30 in. with lid and fill, drain, vent and pressurization systems.

2.2.2 Digital integrating voltmeter, 1 microvolt least count, 0-100v.

2.2.3 Pressure transducers, strain gage type, 0-50 psia (readout on 2.2.2).

2.2.4 Temperature sensors (2), platinum resistance bulb, $0-560^{0}R$, manufactured by Winsco or Rosemount (readout on 2.2.2).

2.2.5 Flowmeter, turbine type, calibrated for liquid hydrogen, 1.5 - 15 cfm (readout on 2.2.2).

2.2.6 ΔP transducer, 0-10 in. H_2O, manufactured by Baraton (readout on 2.2.2).

2.2.7 Milliammeter, 0 - 0.1 amp, accuracy 1 percent.

2.2.8 Dynamometer, AiResearch, Model TE 617805, 0-0.1, 0-1, 0-10 oz-in., accuracy 3 percent.

2.2.9 Pressure vessel, 150 psig working pressure, 1.0 cu ft volume (minimum).

2.2.10 Dewar, Vacuum jacketed 8-1/2 x 16 inch with lid.

2.2.11 Pressure gage, 0-200 psig, 1/2 percent accuracy.

2.2.12 Inclined manometer, 2 in. of water.

2.2.13 Flowmeter, 1-10 CFM with booster, orifice type.

2.2.14 Temperature bridge, Leeds & Northrup potentiometer bridge type, iron constantan couples.

2.2.15 Ammeter, dc. 0.5 amps, 1/2 percent accuracy.

2.2.16 Voltmeter, dc 0-30 v, 1/2 percent accuracy.

2.2.17 Digital counter.

2.2.18 Dynamometer, Magtrol model HD106-1, 0-0.5, 0-1, 0-2 oz-in., accuracy 2-1/2 percent.

2.2.19 Variable dc power supply 0-40 v. 0-0.5 amp (min.)

2.2.20 Pressure gage 0-30 psig, 1/2 percent accuracy.

2.2.21 Pressure gage 0-100 psig, 1/2 percent accuracy.

2.2.22 Oscilloscope, Techtronix 547 with 1A1 plug in, or equivalent.

3. TEST CONDITIONS

3.1 TEST SPECIMEN

Only one unit is being fabricated on the subject contract; it will be utilized for all tests specified herein.

3.2 GENERAL

Each test setup shall be photographed. Unless otherwise specified, all tests shall be performed at the following laboratory ambient conditions:

Temperature	0 to 35°C
Atmospheric Pressure	28 to 31 in. Hg abs
Relative Humidity	Not greater than 90 percent relative

3.3 TEST TOLERANCES

Unless otherwise specified, test tolerances shall not vary more than ±3°F for all temperatures above -100°F or ±5°F for all temperatures below -100°F; ±2 percent for all applied voltages.

4.0 PROCEDURE

4.1 Examination of Product

The mixer assembly shall be examined for conformance to the outline drawing with respect to workmanship, finish dimensions and markings. Examine the assembly thoroughly for evidence of damage due to handling and/or shipping. The impeller shall turn freely with no evidence of binding.

4.2 Motor Power Determination

4.2.1 Test Philosophy

The methods presented herein to measure the total power input to the motor, and the efficiency of the electronics module, are explained with the aid of Figure 1.

It can be seen that there are two power input paths to the motor: The main motor power bus and the position sensor excitation lines, both from the electronics. There are two power output paths from the motor back to the electronics: The position sensor feedback lines and the electronic commutator. The balance of the power supplied to the motor remains in the tank in the form of losses and in the form of useful work. The determination of the latter is covered elsewhere in this report. The net power input to the motor is obtained by measuring the gross power input to the motor and subtracting from it that power which is returned to the electronics. With the measurement the total input current to the electronics, sufficient information is also obtained to determine the efficiency of the electronics.

The net input power to the motor, P_{MN}, is given by:

$$P_{MN} = P_{MB} + P_{ME} - P_{EF} - P_{EC}$$

where P_{MB} is the power supplied to the motor by the motor bus

P_{ME} is the power supplied to excite the shaft position sensors

P_{EF} is the power returned to the electronics as the shaft position feedback signal

P_{EC} is that portion of P_{MB} which is dissipated in the electronic commutator in the form of switching losses and forward drops.

If P_{Ei} is the input power to the electronics, then the efficiency of the electronics module is given by

$$\eta_E = P_{MN} \div P_{Ei} \qquad 2$$

The power input to the electronics (P_{Ei}) from the power supply is readily measured. The methods for obtaining the other powers involved are described in the following paragraphs.

4.2.2 Motor Bus Power

The power supplied to the motor via the bus connecting the motor to the electronics is given by:

$$P_{MB} = \frac{1}{T} \int_0^T e_m \, i_m \, dt \qquad 3$$

where e_m is the instantaneous motor input voltage, i_m is the instantaneous motor input current, and T is the periodicity of the power pulses.

Capacitor C_s shown in Figure 1 is sufficiently large to hold the motor voltage constant at a given operating point. Mathematically:

$$e_m = V_M = \text{constant} \qquad 4$$

and thus:

$$P_{MB} = \frac{V_M}{T} \int_0^T i_m dt = V_M \, I_M \qquad 5$$

where I_M is the average motor current.

V_M will be directly measured in the test set-up by means of a DC digital voltmeter. The average motor current is obtained indirectly. It may be noted from Figure 1 that all of current I_M, and only I_M, is supplied via the shaping resistor, R_E. Since the potentials at both the terminations of this resistor are DC, the current is given by

$$I_M = \frac{V_A - V_M}{R_E} \qquad 6$$

and thus finally

$$P_{MB} = \frac{V_M (V_A - V_M)}{R_E} \qquad 7$$

where V_A is the DC voltage supplied to the electronics module (also measured with a digital voltmeter). R_E is a fixed wire-wound resistor, thus its value is accurately known and stable.

It is well to note that if C_S were absent, then both e_m and i_m would be complex wave forms containing significant fourier components to very high frequencies, making the integration and multiplication called for by equation 5 difficult to achieve accurately without a rather special wattmeter transducer.

4.2.3 Shaft Position Sensor Excitation Losses

The excitation power of the motor shaft position sensors is virtually all dissipated in the tank. The 100K Hz excitation voltage is sinusoidal, $E_{pk} \sin \omega t$; the excitation current is also essentially sinusoidal and lagging, $I_{pk} \sin (\omega t - \theta)$. Thus the real power is given by

$$P_{ME} = \frac{1}{2} I_{pk} E_{pk} \cos\theta \, . \qquad 8$$

This power is readily measurable to an accuracy of ± 15% with the shunt and oscilloscope set-up shown in Figure 1. These losses are temperature sensitive but independent of motor load.

For simplicity, the measurement of these losses will be performed in the electronics laboratory rather than in the cryogenics laboratories. Since LH_2 cannot be used in the electronics laboratory, measurements will be made in LH_e and LN_2. The losses under these conditions will then be linearly extrapolated to obtain the losses at LH_2 temperatures. It should be noted that because the excitation losses are small compared to the total in-tank power, relatively large errors in their measurement have little effect on the accuracy of the total in-tank power determination. It has been found that copper and iron losses are essentially linear in this temperature range, thus the linear extrapolation is valid.

4.2.4 Position Feedback Signal Power

The portion of the position sensor excitation power extracted from the tank in the form of a feedback signal actuating the commutator amplifiers is typically in the order of two milliwatts, and thus is considered to be negligible. Consequently

$$P_{EF} \cong 0 \, . \qquad 9$$

4.2.5 Commutation Losses

Not all the power entering the tank via the motor power bus is dissipated inside the tank. Some of it is dissipated in the commutator which is located in the electronics package. These losses consist of two components: Forward conduction losses of the transistors and switching losses of the transistors and of their protective zeners. The measurement of both of these losses present sufficient difficulties that again they will be measured in the electronics laboratory rather than the cryogenics laboratory.

4.2.5.1 Commutator Series Drop

The commutator forward conduction drop consists of the product of the motor current and of the transistor collector to emitter saturation voltage. This saturation voltage is difficult to measure under dynamic conditions because the large, normal, collector to emitter signal excursions make small deviations from zero hard to resolve.

The transistor saturation and wiring losses will be statically determined as a function of current for each of the four commutators, and the power absorbed will be graphed as a function of the average motor current. This data can then be used with the information obtained during cryogenic testing to calculate the in-tank power losses. For a given operating point these losses are independent of motor temperature, thus calibration at lab ambient is adequate.

4.2.5.2 Switching Losses

The switching losses of the commutator present a rather complex picture particularly in the presence of the stray capacitance associated with the long cable.

In the absence of stray capacitance, (including the transistor's junction capacitance), the turn-on pulse would be dissipationless since the initial transistor voltage would be instantly transferred to the motor winding inductance, after which current would build up in the standard L/R circuit manner. In practice, however, the stray capacitance results in a somewhat triangular power pulse which is a complex function of the circuit parameters, of current rise time, (i.e., of motor speed) of amplifier gain, and of sensor dynamics. This power pulse is measurable by numerical integration of a simultaneous display of transistor collector current and collector to emitter voltage.

The turn-off transient consists primarily of the discharge of the energy stored in the motor inductance just prior to commutation. Some of this energy is lost in the winding resistance, some in the switching transistor, and some in the protective Zeners. This energy is again measurable by numerical integration of a simultaneous oscilloscope display of collector to emitter voltage and the combined transistor/zener current. This power is a function of circuit parameters, motor load, motor speed, and motor temperature.

The above measurements and the associated data reduction are time consuming. Furthermore, the measurements require high frequency current shunts, as well as access to portions of circuitry not normally available under field conditions. It is for these reasons that these losses will be calibrated in the electronics laboratory.

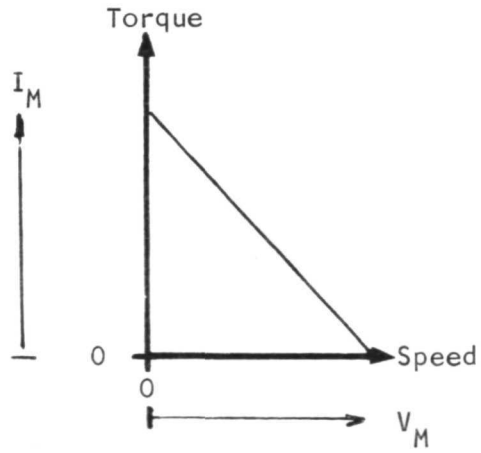
The motor will be operated in LN_2 and in LH_2 with the breadboard electronics. The torque-speed curve shall be sampled at several points by means of an eddy-current brake, and the switching losses determined from oscilloscope photographs taken at each point. This data will be plotted for the two temperatures as function of motor current, extrapolated to LH_2 temperatures, and then combined with the excitation and conduction losses to yield a calibration curve for $(P_{ME} - P_{EF} - P_{EC})$ vs current.

Finally, the determination of net motor input power is reduced to:

$$P_{MN} = V_M I_M - f_{(I_M)} \qquad 10$$

- $f_{(I_M)}$ — Calibrated in the Electronics Laboratory
- I_M — Calculated from measurements in the Cryogenics Laboratory (Equation 6)
- V_M — Measured in the Cryogenics Laboratory

The switching losses are a function of switching frequency and thus a function of motor speed. For this reason the $f_{(I_M)}$ portion of equation 10 holds only for a particular torque speed (or current-speed) characteristic as shown below.



Over the temperature range under consideration ($4^{\circ}K$ to $77^{\circ}K$) the flux of the rotor magnet has been found to remain constant and thus the torque-speed characteristic is determined by the total circuit resistance only. In order to compensate for stator resistance changes, the tests at LH_2 and LN_2 must be run with external resistance (R_E) chosen to obtain the torque-speed characteristic specified for LH_2 temperatures, thus maintaining a constant relationship between speed and motor current.

4.3 Cryogenic Testing

4.3.1 Cool Down and Slugging

The mixer shall be installed in the test ducting with the electronics package mounted to a convenient surface outside the dewar as shown in Figure 2. The setup and fan shall be purged for 15 minutes minimum by evacuating the dewar to 10 microns pressure. The setup (dewar) shall then be filled with boiloff-hydrogen gas to a pressure of 17 to 20 psia. Liquid hydrogen shall then be introduced into the dewar. When the dewar temperature reaches $100^{\circ}R$ apply 28 ± 0.5 vdc to the electronics package. A record of test time shall be maintained and recorded on the applicable data sheet. Motor current shall be observed during filling. The current may vary but if the current remains at or above 0.32 amps for more than 1 minute it is an indication that the mixer has stopped. Shut power OFF to motor immediately and notify proper AiResearch representative. If motor current remains below 0.32 amps, filling shall continue until the proper liquid level is reached.

4.3.2 Calibration in Liquid Hydrogen

Immediately upon completion of the operations called out in Paragraph 4.3.1, the dewar pressure shall be adjusted to 17 ± 0.5 psia and the temperature allowed to stabilize at 37 ± $2^{\circ}R$. The back pressure valve shall be opened fully and the first data point recorded. The valve shall be partially closed and data points recorded at flows of approximately 8, 6.5, and 3.5 cfm. A data point recording shall include the following:

Mixer Inlet Pressure

Mixer Inlet Temperature

Mixer Pressure Rise

Flow Rate

Applied Voltage

Input Current

Motor Speed

Motor Voltage

Operating Time

4.3.3 Calibration in Gaseous Hydrogen

Continuing from 4.3.2, if possible, liquid shall be drained from the dewar until the mixer inlet duct is above the level of the liquid hydrogen and is positioned to pick up hydrogen vapor at a pressure of 17 ±0.5 psia and a temperature of 37 ± 2°R. The mixer shall be operated and data points recorded as called out in Paragraph 4.3.2.

4.3.4 Calibration in Gaseous Helium

The mixer shall be mounted in a closed loop with a helium connection and the loop reinstalled in the dewar as shown in Figure 3. The loop vent valve shall be opened and the system evacuated as discussed in Paragraph 4.3.1. Prior to filling with hydrogen, the loop vent valve shall be closed and the loop pressurized to 17 to 20 psia and filling with hydrogen started. During filling and operation, the pressure inside the loop shall be maintained greater than dewar pressure with makeup helium to prevent hydrogen from leaking into the loop through any minor system leaks that might be produced by thermal contraction. After the helium temperature is stabilized at 37 ± 2°R and its pressure is stabilized at 17 ± 0.5 psia data points shall be recorded as specified in Paragraph 4.3.2. Voltage, pressure and temperature shall also be recorded.

4.3.5 Endurance

The mixer shall be reinstalled in the dewar as described in Paragraph 4.1.2 and a cycle timer installed on the input power line. The timer shall be set to cycle 4 min ± 15 sec ON and 2 min ± 15 sec OFF. The inlet duct shall be immersed in liquid hydrogen at all times. The test shall be continued until the total duration of this test plus the operating times of Paragraphs 4.3.1, 4.3.2, 4.3.3, and 4.3.4 equal 100 hr. The sum of times of this test and Paragraph 4.3.2 shall not be less than 75 hr. The loop back pressure shall be such that after coming up to speed the mixer does not flow less than 5 cfm. The data point recordings called out in Paragraph 4.3.2 shall be recorded every four hours.

4.4 Aerodynamic Calibration

4.4.1

In order to determine motor efficiency at very low temperatures, it is necessary to know the motor shaft power. To know motor shaft power, it is necessary to measure motor torque at these very low temperatures or to apply a known load to the motor shaft. Measurement of motor torque at liquid hydrogen temperatures is very difficult, so the mixer aerodynamic components will be calibrated in air to provide a known load in the operational fluids (LH_2, GH_2 and GH_e), and as shown in Figure 4.

For such a calibration to be valid, geometric and dynamic similarity must be maintained. For geometric similarity to be maintained, the mechanical configuration must be the same for the unit operating in the operating fluid and in the calibrating fluid. Both the operating and calibrating fluids must also strike the aerodynamic components at the same angle for geometric similarity to be maintained. To maintain dynamic similarity, both the calibrating fluid and operating fluid Reynolds Numbers (N_R) must be the same.

$$N_R = \frac{VC\rho}{\mu} \text{ (dimensionless)}$$

V Fluid Velocity

C Characteristic Dimension (blade chord length)

ρ Fluid Density

μ Viscosity

In order to insure geometric similarity, the rotational speed and flow rate may be held constant in both the calibrating and operating fluids. Since the same aerodynamic components are used for both calibration and operation, geometric similarity is assured if the angle at which the blading meets the fluid (air angle) is the same in both the calibrating and operating fluids. The rotational speed and through flow velocity determine the air angle, and if the rotational speed and volumetric flow rates are the same for both the calibrating and operating fluids, geometric similarity is assured.

Reynolds Number is fundamental to the establishment of dynamic similarity. It establishes the relationship between the viscous and inertial forces and insures that dimensionless coefficients are comparable when a machine is operated in two different fluids. By inspection of the formula for Reynolds Number, it may be seen that all the terms which effect incompressible flow between two geometrically similar devices are included. By way of contrast Specific Speed (N_S) is often considered an influencing rotating machinery performance.

$$N_S = \frac{rpm\sqrt{CFM}}{\Delta P/\sigma}$$

ΔP Pressure change

σ ratio of fluid densities

Specific Speed does influence performance and may be applied without knowing the dimensions of the machine in question. It tacitly assumes that any viscous changes are unimportant. It is, a good rule of thumb but ignores two items which may exercise a powerful influence on performance, blade chord

length and fluid viscosity. A careful examination will show that for a constant geometry, all terms effecting performance included in N_S are included in N_R, but N_R also includes dimensional and viscosity dimensions which N_S does not have.

The "C" term in the N_R equation is a constant; V will be the same whenever the rotational speed and volumetric flow rates are the same for both fluids. The viscosity term is independent of pressure in the range of pressures under consideration; it is a function only of the properties of the fluid and the fluid temperature. Then for N_R to be the same for both the calibrating and operating fluids the following relationship holds:

$$\rho_{cal} = \rho_{operating} \frac{\mu\ cal}{\mu\ operating}$$

The pressures called out in the following paragraphs were found using this relationship. In order to make sure that the air angles and velocities are the same, each operating point must have a calibration point. This has been accomplished in the paragraphs that follow.

It has been found that the brushless motor will operate satisfactorily at room temperature, so it will be used for the aerodynamics calibration.

4.4.2 In order to maintain dynamic similarity the air pressure at the mixer inlet shall be maintained at 161 ±2 psia (146.3 ±2 psig). The fan speed and back pressure shall be adjusted to within 1 percent of each of the values of speed and volume flow obtained for the liquid hydrogen calibration of Paragraph 4.1.3. The following parameters shall be recorded:

Mixer Inlet Pressure

Mixer Inlet Temperature

Mixer Pressure Rise

Flowrate

Motor Voltage

Motor Current

Motor Speed

4.4.3 The test specified in Paragraph 4.1.7.1 shall be repeated except that the mixer inlet pressure shall be 32 ±0.5 psia (17.3 ±0.5 psig) and the operating points from the helium test of Paragraph 4.1.5 shall be used.

4.4.4 The test specified in Paragraph 4.1.7.1 shall be repeated except that the mixer inlet pressure shall be 75 ±1.0 psia (60.3 ±1.0 psig) and the speeds and volume flows shall be within 1 percent of those obtained during the gaseous hydrogen calibration, Paragraph 4.1.4.

4.4.5 Motor Calibration

The impeller shall be removed from the motor. The motor shall be connected to a dynamometer. The dynamometer shall be set to maintain each of the motor voltages, currents and speeds from Paragraphs 4.1.7.1, 4.1.7.2, and 4.1.7.3. The following data shall be recorded:

Voltage

Motor Current

Motor Speed

Dynamometer Reading (Load)

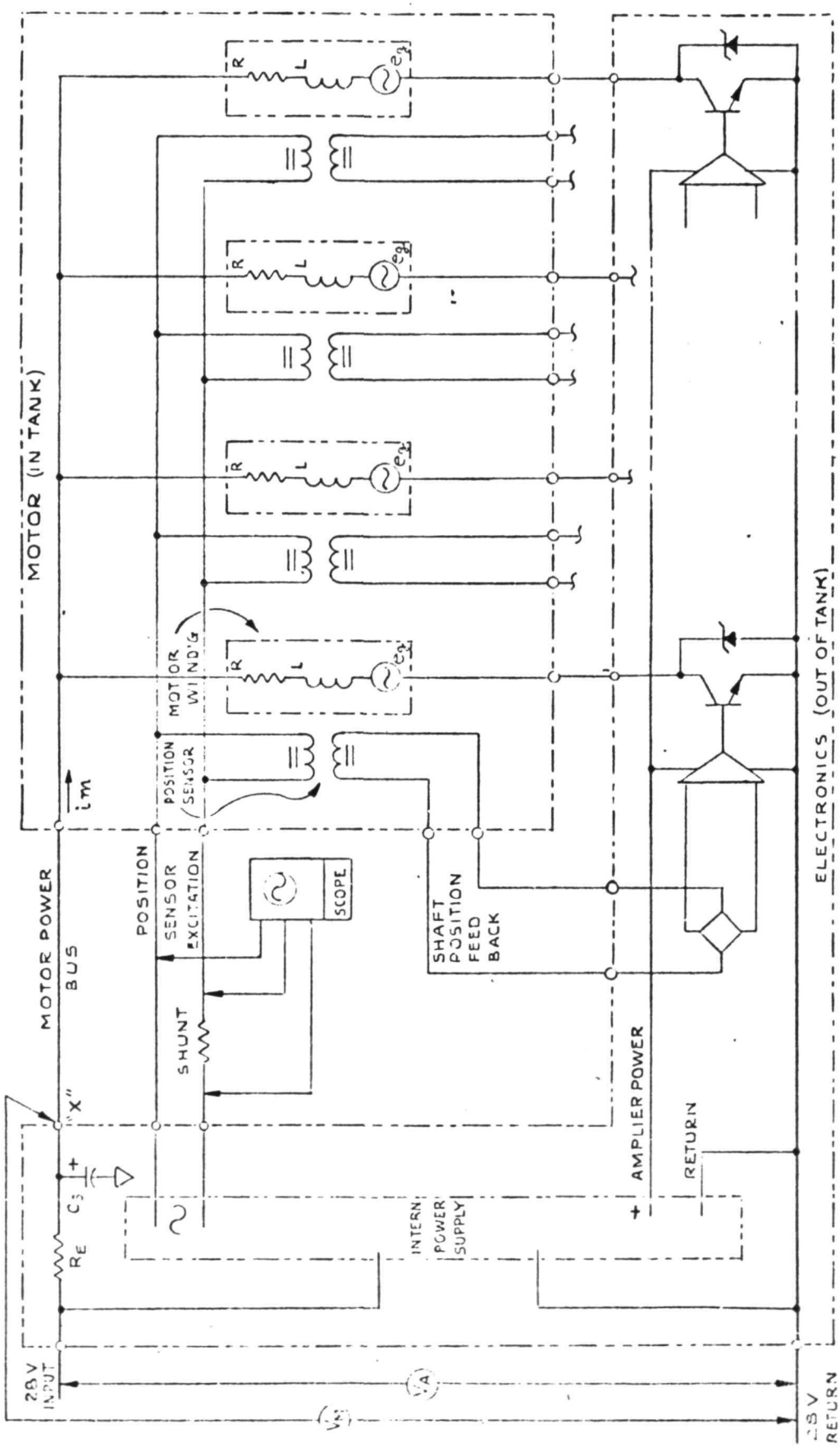


Figure 1. Motor/Electronics Power Test Schematic

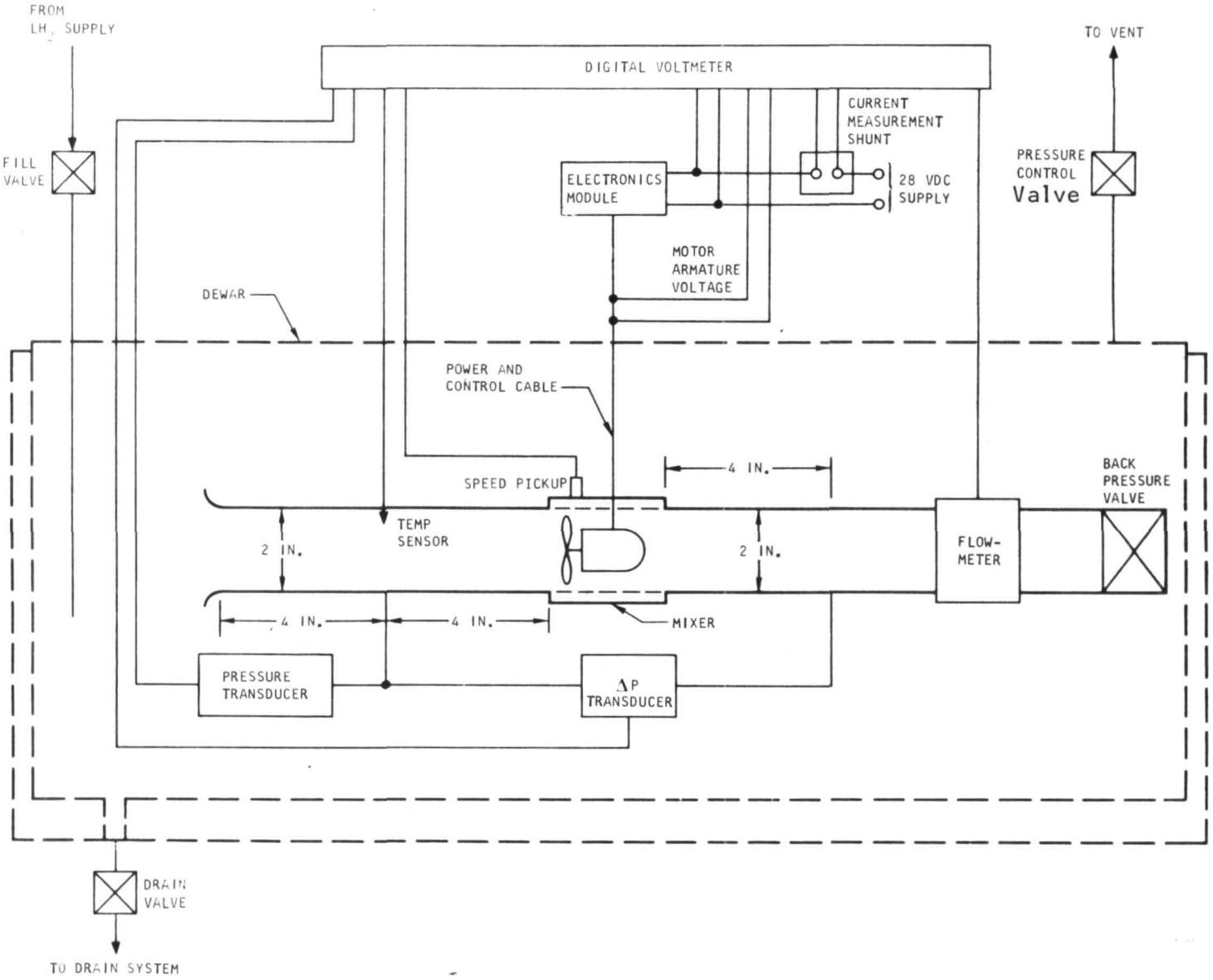


Figure 2. Hydrogen Test Setup

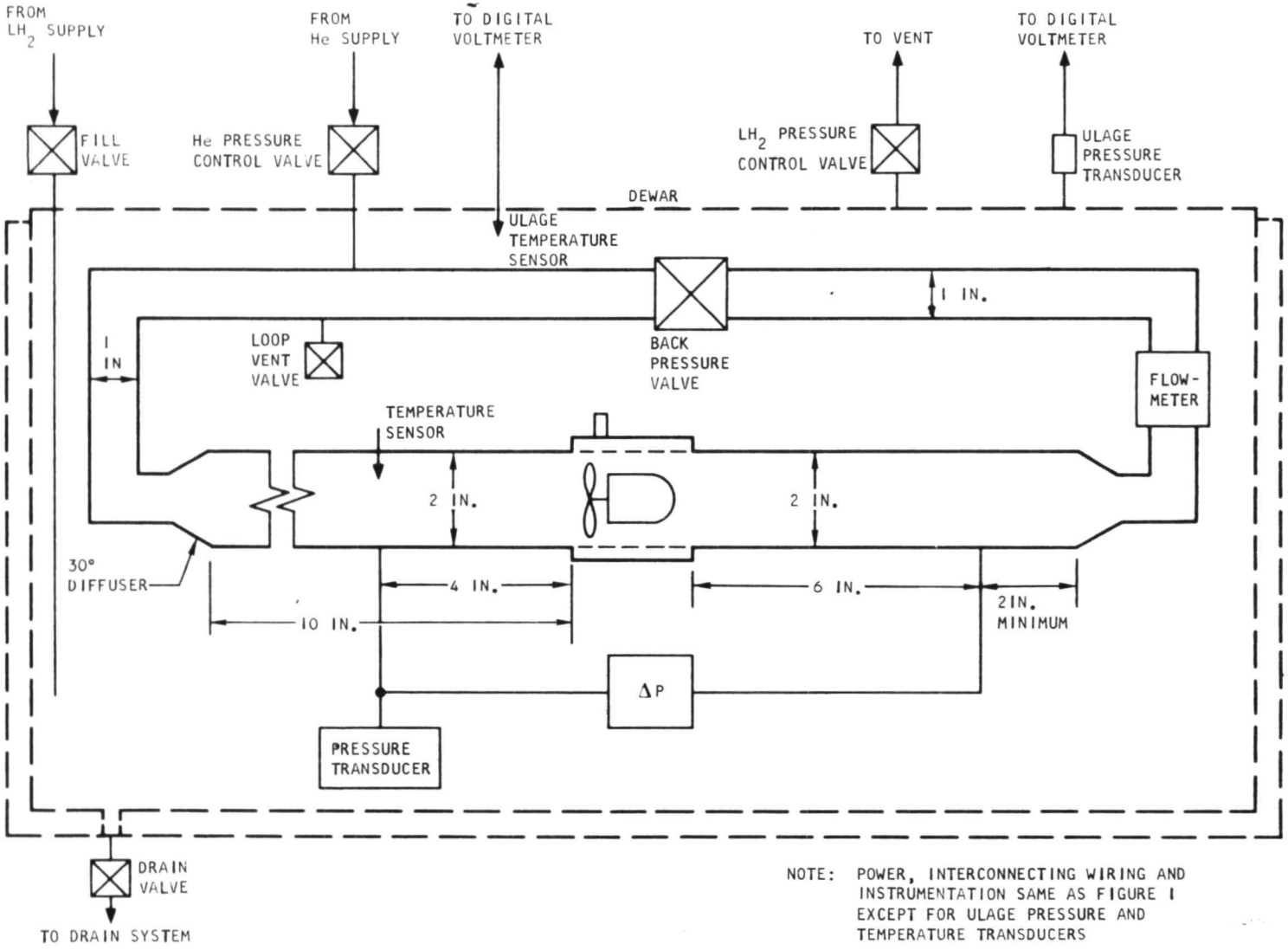


Figure 3. Helium Test Setup

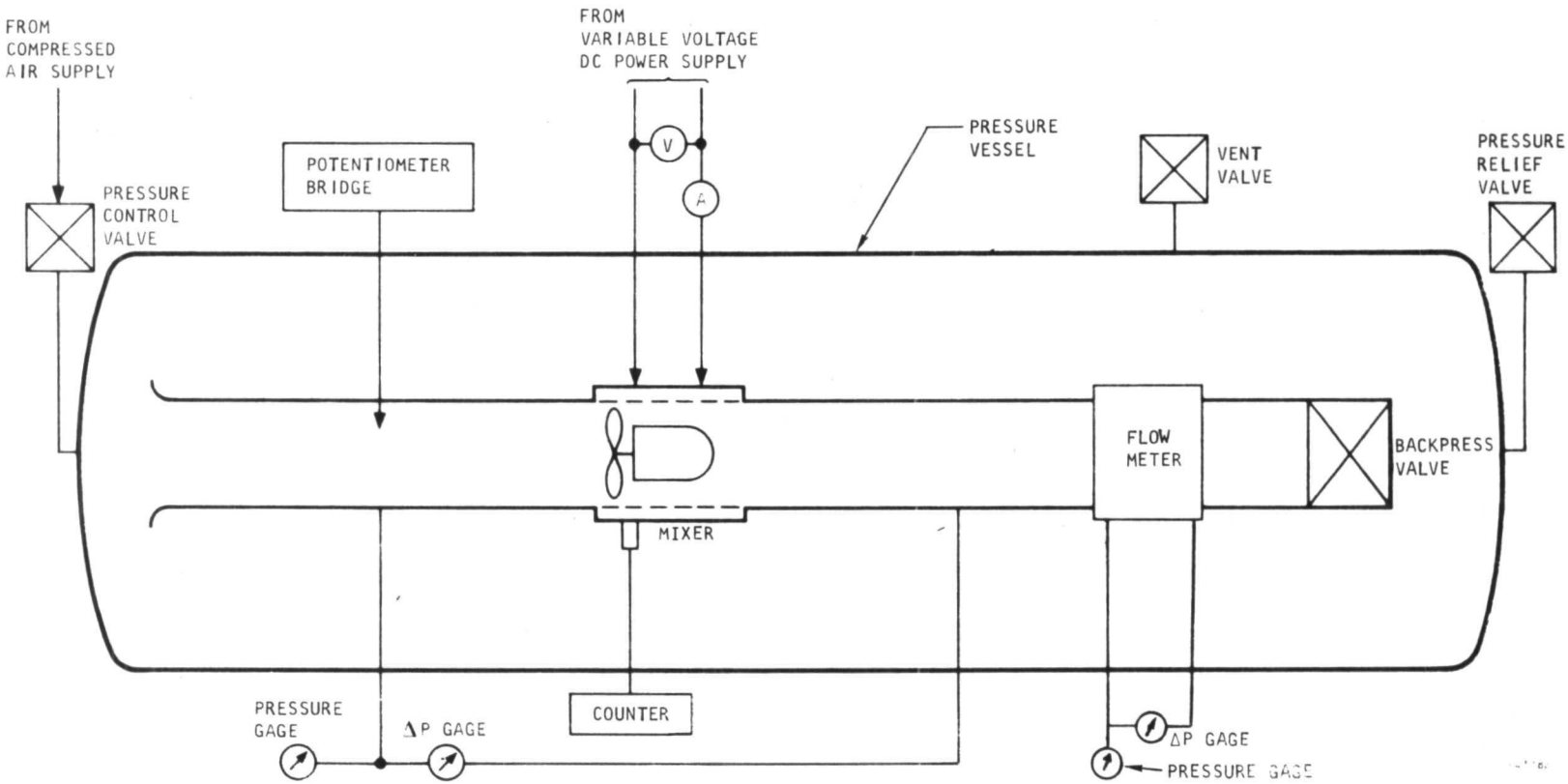


Figure 4. Aerodynamic Calibration Test Setup

APPENDIX C

COMPONENT FAILURE ANALYSIS REPORT

ARINC Research Corp.
Report No. 571A, B

September 1968

technical notes

FAILURE ANALYSIS REPORT NO. 571A, B

N-CHANNEL FIELD EFFECT TRANSISTOR TYPE FF600

September 1968

Prepared for

GARRETT AIRESEARCH MANUFACTURING CO.
Torrance, California

Prepared by

H. Rosenberg
L. Larsen
M. Baker

WESTERN DIVISION
ARINC RESEARCH CORPORATION
P.O. BOX 1375/SANTA ANA, CALIF.

ARINC RESEARCH CORPORATION

COMPONENT FAILURE ANALYSIS REPORT

No. 571A

Date 9-19-68

Customer AiResearch | Failure Report No. ____

Part Ident. No. 3 | Part Type P/N FF600 (Fotofet)

Part Mfr. Crystalonics | Date Code None available.

Description of Failure Conditions

Device indicated an open circuit after 26 temperature cycles.

1. Electrical Measurement Analysis –

Parameter	Condition	Spec.	Actual Reading
BV_{DSO}		15V	Open
BV_{DGO}		15V	23V (see Plate 1)
BV_{GSO}		-10V	Open
I_{GSS}	V_{GS} = -10V, V_{DS} = 0	0.5 nA min - 3 nA max	Open
I_{DSS}	V_{DS} = 10V, V_{GS} = 0	8 mA min (25 mA Typ)	Open

2. Curve Tracer Analysis – Values were obtained for gate to drain characteristics (Photo 1), but no measurements could be obtained for gate to source, indicating an open connection with the source (Photo 2).

3. Hermetic Seal Testing – This device was tested to 1 X 10^{-8} atm cc/sec by means of tracergas, and did not exhibit any hermetic leakage.

4. Visual Examination –

   a. External – All aspects of external construction were suitable. The package weld and the glass lens seal were satisfactory. No defects were noted in the lens or in the region it was bonded to the metal cap.

   b. Internal – Examination of the internal assembly showed that the source bond was separated from the die at the region of the contact metal (Photo 3a). The region where the bond had separated displayed signs of purple plague (Photo 3b). This plague is indicative of improper bonding conditions used

in the assembly operations. In addition to the above, contamination, pinholes, and oxide defects were present on the die surface. These were not related to the existing failure, but are indicative of poor manufacturing techniques (Photo 3a).

6. Microprobe Analysis – Microprobing of the die assembly indicated all parameters to be within specification. This verified that no other failure modes were present.

7. Mode and Cause of Failure – The failure mode of this device is an electrical open condition. The failure mechanism is a defective lead bond at the source region of the device. This defective bond was created by improper manufacturing conditions during device assembly.

8. Recommendations – The existence of purple plague and other surface and oxide defects relate to inadequacies in the processing operations used by the manufacturer of this device. Since these findings can be related to having a deleterious effect on reliability, it is recommended that 1) the device manufacturer be shown the photographs of this unit, 2) corrective action be verified by the manufacturer through properly established documentation and quality control procedures, and 3) a screening test be established to eliminate open bond failures of the type described in this report.

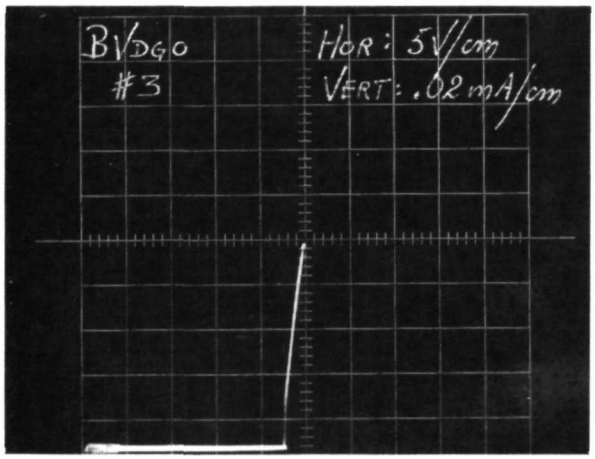


Photo 1. Curve Tracer
Measurement of BV_{DGO}

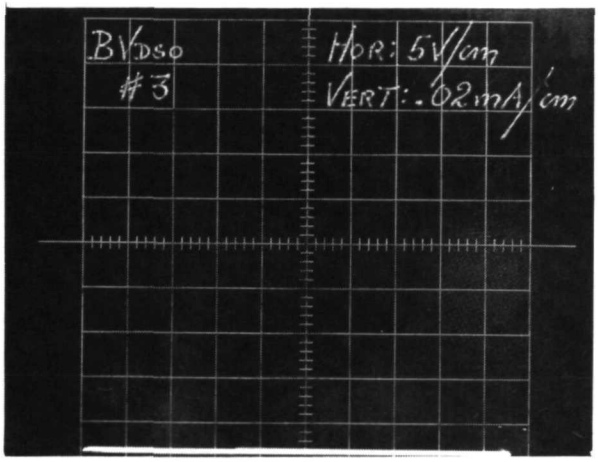


Photo 2. Curve Tracer
Measurement of BV_{DSO}
(open condition)

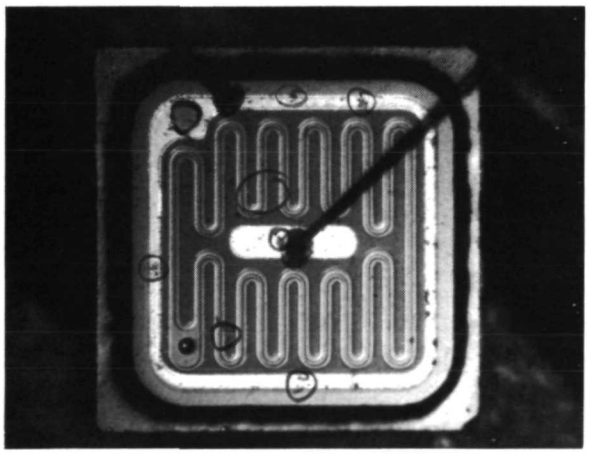


Photo 3a. View of Crystal Assembly (Note oxide pinholes, defects and contamination)
62.5X magnification

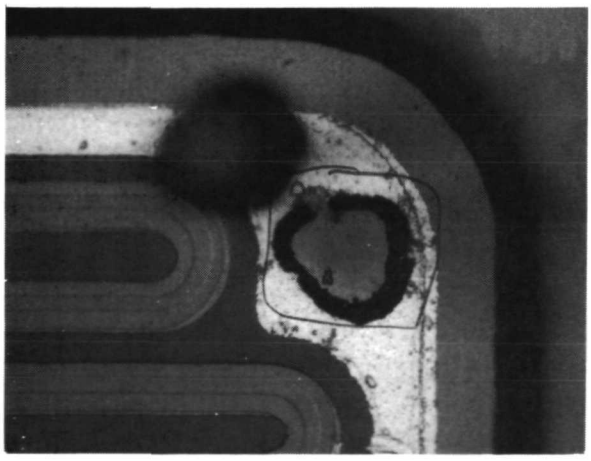


Photo 3b. View of Defective Bond
Note discoloration (purple plague)
250X magnification

F-16026

ARINC RESEARCH CORPORATION

COMPONENT FAILURE ANALYSIS REPORT

No. 571B

Date 9-19-68

Customer AiResearch

Failure Report No. _____

Part Ident. No. 5

Part Type P/N FF600 (Fotofet)

Part Mfr. Crystalonics

Date Code None available.

Description of Failure Conditions

Device No. 5 could not be biased off (drain current near zero) after 160 temperature cycles.

1. Electrical Measurement Analysis –

Parameter	Condition	Spec.	Actual Reading
BV_{DSO}		15V	>80V
BV_{DGO}		15V	68V (Plate 2)
BV_{GSO}		-10V	-6V (Plate 3)
I_{GSS}	V_{GS} = -10V, V_{DS} = 0	0.5 nA min - 3 nA max	(Breaks down at 6V)
I_{DSS}	V_{DS} = 10V, V_{GS} = 0	8 mA min - 25 mA Typ.	50 mA

2. Curve Tracer Analysis – The gate to source voltage was determined to be 6 volts instead of the required 10 volts minimum (Photo 1). This low breakdown condition resulted in conduction and inability to bias off under the circuit specified at a 10 volt supply. The gate to drain voltage was within specification limits (Photo 2).

3. Hermetic Seal Testing – This device was tested to 1 X 10^{-8} atm cc/sec by means of tracergas and did not exhibit any hermetic leakage.

4. Visual Examination –

   a. External – All aspects of external construction were satisfactory. The package weld and the lens seal were satisfactory. No defects were noted in the lens or in the region it was bonded to the metal cap.

b. Internal – Examination of the internal assembly displayed several suspect defects on the crystal. One defect, noted at the drain-source junction (Photo 3) appeared as a hole in the oxide, extending into the silicon. This hole was shown to be a microplasm center that resulted in the premature breakdown voltage described above. Microplasms result from contamination introduced during processing operations such as high temperature diffusion. In addition to the microplasm, pinholes, resist residue, lint particles, etc. were present on the surface of the crystal (Photo 4). Although these were not related to the failure described above, they are indicative of poor manufacturing conditions, and have been shown to be related to device reliability.

5. Chemical Analysis – Several attempts were made to clean up the defect condition by sequential etching of the protecting oxide layer. No significant change in electrical characteristics was noted, verifying the condition to be existent in some form not related directly to surface effects.

6. Mode and Cause of Failure – The failure mode of this device is an inferior breakdown voltage for the gate to source characteristics. The failure mechanism is a microplasm, or region of high current density that was caused by defective manufacturing techniques.

7. Recommendations – Since this is the second failure related to manufacturing techniques, it is recommended that the statement for 571A be followed, and additionally an effort be made towards obtaining a more reliable source for this component.

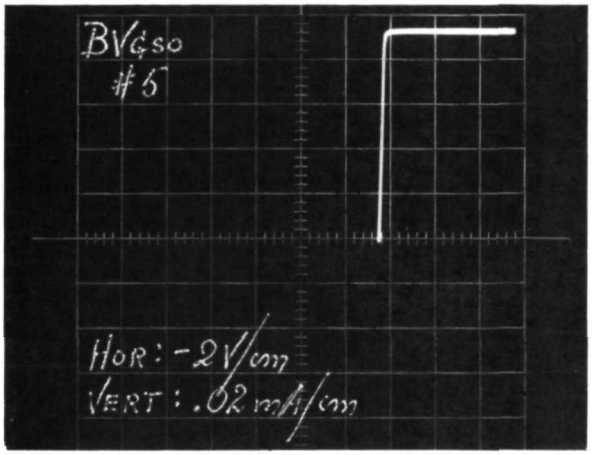


Photo 1. Curve Tracer Results of BV_{GSO}
(Should be 10 volts min.)

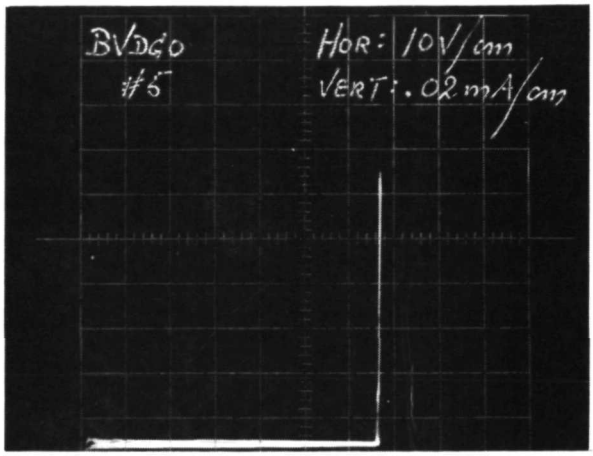


Photo 2. Curve Tracer Results of BV_{DGO}
(Satisfactory voltage level)

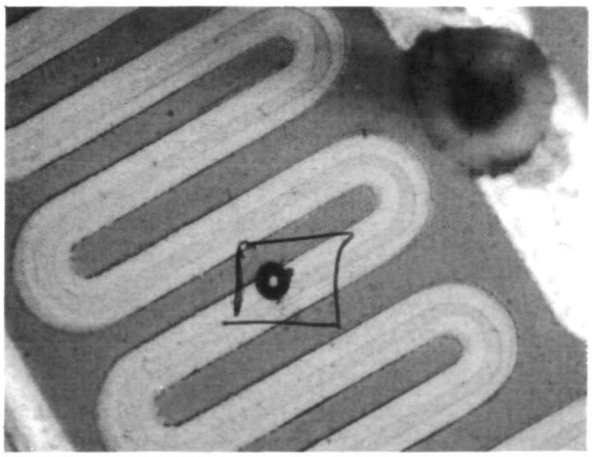


Photo 3. View of Defect at Drain-Source Junction
250X magnification

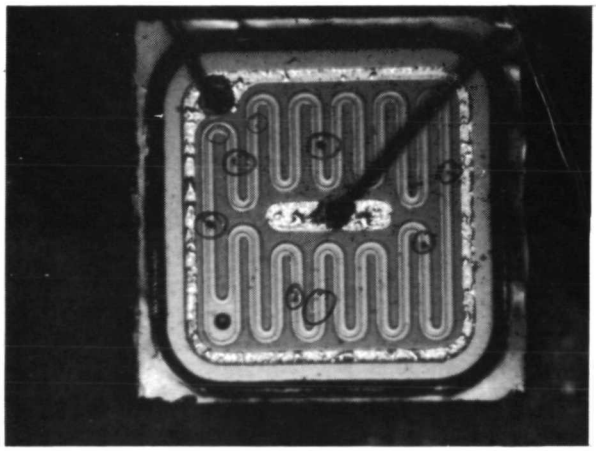


Photo 4. View of Crystal Assembly (Defects and contamination are circled in red)

F-16025

APPENDIX D

BEARING REPORT

OPERATING DATA

BEARING REPORT BR 690731-7-590

UNIT: LIQUID H_2 MIXER

P/N:

S/N:

BEARING: MPB SR3 SHIELDED AND DUROID SEPARATOR

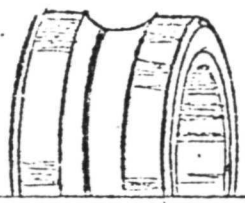
DIST.: R. MORGAN

R.O.:

NO. I OUTBOARD BEARING (REAR)

INNER RING

NORMAL VERY LIGHT PRELOAD BALL TRACK



SEPARATOR

BALL CONTACT POINTS LIGHTLY POLISHED



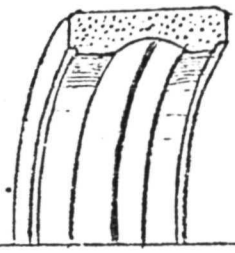
BALLS

EXCELLENT



OUTER RING

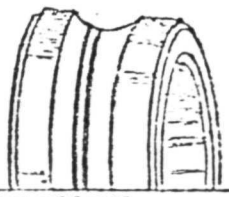
NORMAL VERY LIGHT PRELOAD BALL TRACK



NO. II OUTBOARD BEARING (FRONT)

INNER RING

TWO NORMAL VERY LIGHT PRELOAD BALL TRACKS.



SEPARATOR

BALL CONTACT POINTS LIGHTLY POLISHED.



BALLS

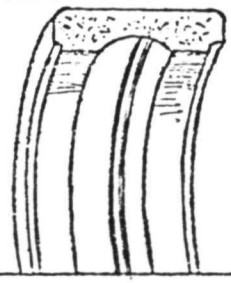
SLIGHT SURFACE DISCOLORATION.



OTHERWISE EXCELLENT.

OUTER RING

TWO NORMAL VERY LIGHT PRELOAD BALL TRACKS.



CONCLUSIONS: BOTH BEARINGS ARE IN EXCELLENT CONDITION AND OPERATED UNDER LIGHT PRELOAD AND ADEQUATE INTERNAL CLEARANCE.

AS TO BE EXPECTED IN DRY BEARINGS, THE RACEWAY LOADED ZONE MATERIAL HAS BECOME SLIGHTLY DULLED AND DISCOLORED. SEPARATOR POCKET WEAR IS NEGLIGIBLE.

THE BEARINGS HAVE POTENTIAL FOR LONG OPERATIONAL LIFE.

CONDITION	I	II
BALANCE	O.K.	O.K.
LOADS	O.K.	O.K.
ALIGNMENT	O.K.	O.K.
LUBRICATION	O.K.	O.K.

7-31-69
DATE

R. Blisk
BEARING COORDINATOR

APPENDIX E

DISTRIBUTION LIST FOR FINAL REPORT

CR-120963 NAS3-11208

APPENDIX E

DISTRIBUTION LIST FOR FINAL REPORT CR-120963

NAS3-11208

			Copies
1.	National Aeronautics & Space Administration Lewis Research Center 21000 Brookpark Road Cleveland, Ohio 44135		
	Attn: Contracting Officer	MS 500-313	1
	Technical Report Control Office	MS 5-5	1
	Technology Utilization Office	MS 3-16	1
	AFSC Liaison Office	MS 501-3	2
	Library		2
	Office of Reliability & Quality Assurance	MS 500-111	1
	G. T. Smith	MS 49-3	3
	C. Gresslin	MS 23-1	2
	W. Mc Cann		1
	J. W. Gregory, Chief	MS 500-203	1
	J. R. Barber		
2.	Director, Physics & Astronomy Programs, SG Office of Space Science NASA, Headquarters Washington, D.C. 20546		1
3.	Director, Planetary Programs, SL Office of Space Science NASA Headquarters Washington, D. C. 20546		1
4.	Director, Manned Space Technology Office, RS Office of Aeronautics & Space Technology NASA Headquarters Washington, D.C. 20546		1
5.	Director Space Property and Power, RP Office of Aeronautics & Space Technology NASA Headquarters Washington, D.C. 20546		2
6.	Director, Launch Vehicles & Propulsion, SV Office of Space Science NASA Headquarters Washington, D.C. 20546		1
7.	Director, Materials & Structures Division, RW Office of Aeronautics & Space Technology NASA Headquarters Washington, D.C. 20546		1

		Copies
8.	Director, Advanced Programs, MT Office of Manned Space Flight NASA Headquarters Washington, D.C. 20546	1
9.	National Technical Information Services Springfield, Virginia 22151	16
10.	National Aeronautics & Space Administration Ames Research Center Moffett Field, California 94035 Attn: Library	1
11.	National Aeronautics & Space Administration Flight Research Center P.O. Box 273 Edwards, California 93523 Attn: Library	1
12.	Director, Technology Utilization Division Office of Technology Utilization NASA Headquarters Washington, D.C. 20546	1
13.	Office of the Director of Defense Research & Engineering Washington, D.C. 20301 Attn: Office of Asst. Dir. (Chem Technology)	1
14.	Office of Aeronautics & Space Technology, R NASA Headquarters Washington, D.C. 20546	1
15.	NASA Scientific & Technical Information Facility P.O. Box 33 College Park, Maryland 20740 Attn: NASA Representative	2
16.	Nation Aeronautics & Space Administration Goddard Space Flight Center Greenbelt, Maryland 20771 Attn: Library	1
17.	National Aeronautics & Space Administration John F. Kennedy Space Center Cocoa Beach, Florida 32931 Attn: Library	1

		Copies
18.	National Aeronautics & Space Administration Langley Research Center Langley Station Hampton, Virginia 23365 Attn: Library	1
19.	National Aeronautics & Space Administration Manned Spacecraft Center Houston, Texas 77001	
	Attn: Library	1
	W. Chandler	1
	W. Dusenberry	1
	C. Yodzis	1
20.	National Aeronautics & Space Administration George C. Marshall Space Flight Center Huntsville, Alabama 35912	
	Attn: Library	1
	J. M. Stuckey	1
	I. G. Yates	1
	E. H. Hyde	1
21.	Jet Propulsion Laboratory 4800 Oak Grove Drive Pasadena, California 91103	
	Attn: Library	1
	L. Stimson	1
	J. Kelly	1
	R. Breshears	1
22.	Defense Documentation Center Cameron Station Building 5 5010 Duke Street Alexandria, Virginia 22314 Attn: TISIA	18
23.	RTD (RTNP) Bolling Air Force Base Washington, D.C. 20332	1
24.	Arnold Engineering Development Center Air Force Systems Command Tullahoma, Tennessee 37389 Attn: Library	1
25.	Advanced Research Projects Agency Washington, D.C. 20525 Attn: Library	1

		Copies
26.	Aeronautical Systems Division Air Force Systems Command Wright-Patterson Air Force Base Dayton, Ohio	1
	Attn: Library	1
	AFML (MAAE)	1
	AFML (MAAM)	1
27.	Air Force Rocket Propulsion Laboratory (RPM) Edwards, California 93523 Attn: Library	1
28.	Air Force FTC (FTAT-2) Edwards Air Force Base, California 93523 Attn: Library	1
29.	Air Force Office of Scientific Research Washington, D.C. 20333 Attn: Library	1
30.	Space & Missile Systems Organization Air Force Unit Post Office Los Angeles, California 90045 Attn: Technical Data Center	1
31.	Office of Research Analyses (OAR) Holloman Air Force Base New Mexico, 88330 Attn: Library	1
32.	U. S. Air Force Washington, D.C. Attn: Library	1
33.	Commanding Officer U. S. Army Research Office (Durham) Box CM, Duke Station Durham, North Carolina 27706 Attn: Library	
34.	Bureau of Naval Weapons Department of the Navy Washington, D.C. Attn: Library	1
35.	Director (Code 6180) U. S. Naval Research Laboratory Washington, D.C. 20390	1

		Copies
36.	Picatinny Arsenal Dover, New Jersey 07801 Attn: Library	1
37.	Air Force Aero Propulsion Laboratory Research & Technology Division Air Force Systems Command United States Air Force Wright-Patterson AFB, Ohio 45433 Attn: APRP (Library)	1
38.	Electronics Division Aerojet-General Corporation P.O. Box 296 Azusa, California 91703 Attn: Library	1
39.	Space Division Aerojet-General Corporation 9200 East Flair Drive El Monte, California 91734 Attn: Library	1
40.	Aerojet Ordance & Manufacturing Aerojet-General Corporation 11711 South Woodruff Avenue Fullerton, California 90241 Attn: Library	1
41.	Aerojet Liquid Rocket Company P.O. Box 15847 Sacramento, California 95813 Attn: Technical Library 2484-201A	1
42.	Aeronutronic Division of Philco Ford Corp. Ford Road Newport Beach, California 92663 Attn: Technical Information Department	1
43.	Aerospace Corporation 2400 E. El Segundo Blvd. Los Angeles, California 90045 Attn: Library-Documents	1
44.	Arthur D. Little, Inc. 20 Acorn Park Cambridge, Massachusetts 02140 Attn: Library R. B. Hinckley	 1 1

		Copies
45.	Astropower Laboratory McDonnell-Douglas Aircraft Company 2121 Paularino Newport Beach, California 92163 Attn: Library	1
46.	ARO, Incorporated Arnold Engineering Development Center Arnold AF Station, Tennessee 37389 Attn: Library	1
47.	Susquehanna Corporation Atlantic Research Division Shirley Highway & Edsall Road Alexandria, Virginia 22314 Attn: Library	1
48.	Beech Aircraft Corporation Boulder Facility Box 631 Boulder, Colorado Attn: Library	1
49.	Bell Aerosystems, Inc. Box 1 Buffalo, New York 14240 Attn: Library	1
50.	Instruments & Life Support Division Bendix Corporation P.O. Box 4508 Davenport, Iowa 52808 Attn: Library	1
51.	Boeing Company Space Division P.O. Box 868 Seattle, Washington 98124 Attn: Library D. H. Zimmerman	1
52.	Boeing Comapny 1625 K Street, N.W. Washington, D.C. 20006	1
53.	Chemical Propulsion Information Agency Applied Physics Laboratory 8621 Georgia Avenue Silver Spring, Maryland 20910	1

		Copies
54.	Chrysler Corporation Missile Division P.O. Box 2628 Detroit, Michigan Attn: Library	1
55.	Chrysler Corporation Space Division P.O. Box 29200 New Orleans, Louisianna 70129 Attn: Librarian	1
56.	Curtiss-Wright Corporation Wright Aeronautical Division Woodridge, New Jersey Attn: Library	1
57.	University of Denver Denver Research Institute P.O. Box 10127 Denver, Colorado 80210 Attn: Security Office	1
58.	Fairchild Stratos Corporation Aircraft Missiles Division Hagerstown, Maryland Attn: Library	1
59.	Research Center Fairchild Hiller Corporation Germantown, Maryland Attn: Library	1
60.	Republic Aviation Fairchild Hiller Corporation Farmington, Long Island New York	1
61.	General Dynamics/Convair P.O. Box 1128 San Diego, California 92112 Attn: Library R. Tatro	 1 1
62.	Missiles and Space Systems Center General Electric Company Valley Forge Space Technology Center P.O. Box 8555 Philadelphia, Pa. 19101 Attn: Library	1

		Copies
63.	General Electric Company Flight Propulsion Lab. Department Cincinnati, Ohio Attn: Library	1
64.	Grumman Aircraft Engineering Corporation Bethpage, Long Island, New York Attn: Library	1
65.	Honeywell Inc. Aerospace Division 2600 Ridgeway Road Minneapolis, Minnesota Attn: Library	1
66.	IIT Research Institute Technology Center Chicago, Illinois 60616 Attn: Library	1
67.	Ling-Temco-Vought Corporation P.O. Box 5907 Dallas, Texas 75222 Attn: Library	1
68.	Linde-Div. of Union Carbide P.O. Box 44 Tonawanda, N. Y. 11450 Attn: G. Nies	1
69.	Lockheed Missiles and Space Co. P.O. Box 504 Sunnyvale, Calif. 94088 Attn: Library R. T. Parmley	1
70.	Marquardt Corporation 16555 Saticoy Street Box 2013 - South Annex Van Nuys, California 91409	1
71.	Denver Division Martin-Marietta Corporation P.O. Box 179 Denver, Colorado 80201 Attn: Library G. C. Skartvedt	1

		Copies
72.	Western Division McDonnell Douglas Astronautics 5301 Bolsa Avenue Huntington Beach, California 92647 Attn: Library P. Klevatt	1
73.	McDonnell Douglas Aircraft Corporation P.O. Box 516 Lambert Field, Missouri 63166 Attn: Library L. F. Kohrs	1 1
74.	Rocketdyne Division North American Rockwell Inc. 6633 Canoga Avenue Canoga Park, California 91304 Attn: Library, Department 596-306	1
75.	Space & Information Systems Division North American Rockwell 12214 Lakewood Blvd. Downey, California Attn: Library E. Hawkinson AC10	1 1
76.	Northrop Space Laboratories 3401 West Broadway Hawthorne, California Attn: Library	1
77.	Purdue University Lafayette, Indiana 47907 Attn: Library (Technical)	1
78.	Goodyear Aerospace Corporation 1210 Massilon Road Akron, Ohio 44306 Attn: C. Shriver	1
79.	Hamilton Standard Corporation Windsor Locks, Connecticut 06096 Attn: Library	1
80.	Stanford Research Institute 333 Ravenswood Avenue Menlo Park, California 94025 Attn: Library	1

		Copies
81.	TRW Systems Inc. 1 Space Park Redondo Beach, California 90278 Attn: Tech. Lib. Doc. Acquisitions	1
82.	United Aircraft Corporation Pratt & Whitney Division Florida Research & Development Center P.O. Box 2691 West Palm Beach, Florida 33402 Attn: Library	1
83.	United Aircraft Corporation United Technology Center P.O. Box 358 Sunnyvale, California 94038 Attn: Library	1
84.	Vickers Incorporated Box 302 Troy, Michigan	1
85.	Airesearch Mfg. Div. Garrett Corporation 9851 Sepulveda Blvd. Los Angeles, California 90009 Attn: Library	1
86.	Airesearch Mfg. Div. Garrett Corporation 402 South 36th Street Phoenix, Arizona 85034 Attn: Library	1
87.	Commanding Officer U.S. Naval Underwater Ordnance Station Newport, Rhode Island 02844 Attn: Library	1
88.	National Science Foundation Engineering Division 1800 G Street N.W. Washington, D.C. 20540 Attn: Library	1
89.	G. T. Schjeldahl Company Northfield, Minnesota Attn: Library	1

		Copies
90.	General Dynamics P.O. Box 748 Fort Worth, Texas 76101	1
91.	Cryonetics Corporation Northwest Industrial Park Burlington, Massachusetts	1
92.	Institute of Aerospace Studies University of Toronto Toronto 5, Ontario Attn: Library	1
93.	FMC Corporation Chemical Research & Development Center P.O. Box 8 Princeton, New Jersey 08540	1
94.	Westinghouse Research Laboratories Buelah Road, Churchill Boro Pittsburg, Pennsylvania 15235	1
95.	Cornell University Department of Materials Science & Engineering Ithaca, New York 14850 Attn: Library	1
96.	Marco Research & Development Co. Whittaker Corporation 131 N. Ludlow Street Dayton, Ohio 45402	1
97.	General Electric Company Apollo Support Department P.O. Box 2500 Daytona Beach, Florida 32015 Attn: C. Ray	1
98.	E. I. DuPont, DeNemours & Company Eastern Laboratory Gibbstown, New Jersey 08027 Attn: Library	1
99.	Esso Research & Engineering Company Special Projects Unit P.O. Box 8 Linden, New Jersey 07036 Attn: Library	1

Copies

100. Minnesota Mining & Manufacturing Company 1
900 Bush Avenue
St. Paul, Minnesota 55106
Attn: Library